CFD AND PIV INVESTIGATION OF UV REACTOR HYDRODYNAMICS

by

Angelo Sozzi

Chemiker FH, Zuercher Hochschule Winterthur, 2000

A THESIS SUBMITTED IN PARTIAL FULFILLMENT OF
THE REQUIREMENTS FOR THE DEGREE OF

MASTER OF APPLIED SCIENCE

in

The Faculty of Graduate Studies

(Chemical and Biological Engineering)

THE UNIVERSITY OF BRITISH COLUMBIA

May 2005

Abstract

The performance of ultraviolet (UV) reactors used for water treatment is greatly influenced by the reactor hydrodynamics, due to the non-homogeneity of the UV-radiation field. Yet, a present lack of rigorous quantitative understanding of the flow behavior in such reactor geometries is shown to limit the versatile and efficient optimization of UV reactors. In this research, the key characteristics of turbulent flow in annular UV-reactors and its influence on reactor performance were studied using particle image velocimetry (PIV) measurements and computational fluid dynamics (CFD) simulations.

Two conceptual reactor configurations, with inlets either concentric (L-shape) or normal (U-shape) to the reactor axis, were investigated experimentally. The time averaged velocity data revealed a strong dependency of the hydrodynamic profile to the inlet position. The frontal inlet of the L-shape reactor resulted in an expanding jet flow with high velocities close to the radiation source (UV-lamp) and areas of recirculation close to the inlet. The perpendicular inlet of the U-shape reactor brought about higher velocities along the outer reactor walls far from the central lamp.

Numerical simulations, using a commercial CFD software package, Fluent, were performed for the L- and U-shape reactor configurations. The influences of mesh structure and the Standard κ-ϵ, Realizable κ-ϵ, and Reynolds stress (RSM) turbulence models were evaluated. The results from the Realizable κ-ϵ and RSM models were in good agreement with the experimental findings. However, the Realizable κ-ϵ model provided the closest match under the given computational restraints.

UV disinfection models were developed by integrating UV-fluence rate and inactivation kinetics with the reactor hydrodynamics. Both, a particle tracking (Lagrangian) random walk model and a volumetric reaction rate based (Eulerian) model were implemented. The performance results of the two approaches were in good agreement with each other and with the experimental data from an industrial prototype reactor. The simulation results provided detailed information on the velocity profiles, reaction rates, and areas of possible short circuiting within the UV-reactor. It is expected that the application of the verified integrated CFD models will help to improve the design and optimization of UV-reactors.

Table of Contents

List of Figures

List of Tables

List of Symbols

C	Concentration of microorganisms, [mol/L]
C_μ	Empirical coefficient, mixing length model, [-]
D	Dose, [mJ/cm^2]
D_1	Diameter of the inlet tube, [cm]
D_2	Diameter of the reactor body,[cm]
D_3	Diameter of the quartz sleeve, [cm]
E	Fluence rate, [mW/cm^2]
k	Inactivation rate constant, [cm^2/mJ]
L_1	Lengt of inlet tube, [cm]
L_2	Lengt of reactor body, [cm]
L_3	Lengt of lamp arc, [cm]
l_m	Mixing length, [m]
l_i	Distance from lamp point to current point (MPSS), [cm]
N	Organism concentration, [PFU/mL]
N_0	Initial organism concentration, [PFU/mL]
n	Number of points for MPSS model, [-]
P	Germicidal lamp output (254 nm) per cm, [W/cm]
Q	Flow rate, [m^3/s]

r	Radial distance from lamp, [cm]
r_L	Radius of lamp sleeve, [cm]
t	Time, [s]
U	Axial velocity, [m/s]
V	Radial velocity, [m/s]
z	Axial distance on lamp, [cm]

Greek letters

ϵ	Turbulent energy dissipation rate, [-]
κ	Turbulent kinetic energy, [-]
μ_t	Turbulent viscosity,
μ	Fluid viscosity, [kg/m s]
σ_w	Absorption coefficient of fluid, [cm^{-1}]

Abbreviations

AdOx	Advanced Oxidation
CFD	Computational fluid dynamics
GPM	US gallons per minute
LDV	Laser Doppler velocimetry
MPSS	Multiple point source summation
PDEs	Partial differential equations
PIV	Particle image velocimetry
RANS	Reynolds averaged Navier-Stokes
RSM	Reynolds stress model
UV	Ultra Violet (at 254 nm)

Acknowledgments

I would like to thank my supervisor Dr. Fariborz Taghipour, for offering me the opportunity to enter an interesting new field, without his patience, guidance and support this thesis would not exist.

Particular thanks goes to Siamak Elyasi for the animated discussions where many of the ideas and solutions were developed and Ramn Toor, whose cheerful disposition, comments and camaraderie made the office a better place to work.

I would also like to acknowledge the assistance of the staff of the Chemical and Biological Engineering Department at UBC. Thanks to the shop will follow at a more leisurely speed.

Furthermore, I would like to thank: Bojun Zhang, a summer student who's ability to generate structured meshes for almost any geometry saved me many hours, and Anita Fischer, for her help in the often tedious process of data extraction.

Thanks also go to NSERC for their important financial contribution.

And finally, I owe it all to my wife, Fan. She gave herself to this effort even more than I. After leaving China and settling in Switzerland, she was not only willing to continent hop again, but also learnt English in record time and found a great job to support our household. Without her devoted help and encouragement, this work would likely have never been completed.

Chapter 1

Introduction, background and objectives

Drinking water is one of the most widely used, yet under-appreciated natural resources in the modern world. The supply and distribution of safe, potable water has been nominated as one of the top 5 engineering achievements of the 20^{th} century, contributing to the quality of life by virtually eliminating waterborne diseases (35). However, the contamination of water resources by civilization (e.g. hormones, pesticides, fuel products), chlorine resistant microorganisms (e.g. *Cryptosporidium*), and mounting evidence that the use of chlorine for disinfection can result in potentially carcinogenic disinfection byproducts (DBPs) (2) have increased the demand for alternative treatment methods. In particular, UV-based technologies have seen rapid development and are being applied to both water disinfection and reduction of low concentration contaminants. The use of UV-radiation for disinfection relies on the inactivation of microorganisms through direct mutation of the DNA, while the UV application for advanced oxidation processes (AOPs) involves exciting oxidants such as hydrogen peroxide (H_2O_2) or ozone (O_3) to form highly reactive hydroxyl-radicals ($^{\bullet}OH$) to oxidize (toxic) contaminants. It has been shown that the majority of contaminants present in water can be either destroyed completely or reduced to more (bio-)degradable forms through oxidation (12).

The boost in UV-treatment development was initiated by a series of legislative events. The United States Environmental Protection Agency (US-EPA) adapted the Safe Drinking Water Act in 1996 to include maximum allowable concentration

levels of DBPs in potable water (30). The same year the US-EPA also revised the guidelines for known chemical, physical and microbiological parameters and extended the list of monitored toxic contaminants. Canada followed suit with their own legislative changes while many European countries had already put similar regulations into effect (28). In 1998, standards for water systems utilizing surface water supplies were tightened, affecting over 140 million Americans. In the year 2000 the US-EPA proposed tougher requirements for groundwater. The regulations apply to more than 150,000 water systems in the US alone. In order to comply with the updated Safe Drinking Water Act, an estimated $150 billion will be have to be invested to ensure the continued provision of safe drinking water, with a predicted $40 billion to be invested in new technologies (31).

This market stimulated the development of new or underdeveloped technologies to meet the demand in water quality. In addition to traditional treatment methods such as filtration, chlorination, and ozonation (22), the array of new methods being developed include the use of UV radiation for primary disinfection and UV advanced oxidation for the removal of toxic, recalcitrant contaminants. Other methods under discussion are the addition of chloramines (less aggressive and odorless) for the persistent disinfection in distribution systems, activated carbon for the adsorption and/or biodegradation of organic contaminants, and the use of membranes for the removal of heavy metals and organic contaminants (12). While both UV disinfection and UV Advanced Oxidation Processes have been known for over 20 years (9), the applications remained mainly of academic interest, due to the high effectiveness and low costs of chlorination. But UV-based technologies fit the new requirements for non DBP generating disinfection processes (UV-disinfection) and show promise for the removal of low concentration recalcitrant contaminants (UV-Advanced Oxidation).

An early cost comparison from the year 1992 (18) showed a cost envelope for UV-treatment processes of 1-10 US$ per thousand gallons, for the removal of organic contaminants in the range of 0.1-1000 ppm. Later studies confirmed these figures (11) placing UV-processes in the cost range of sustainable treatment alternatives. Since expenses can vary widely depending on the type of contaminant to be treated, Bolton et al. (3, 4) proposed a figure of merit for economic comparisons, relating the total expenses incurred, to the electrical energy used per order

of magnitude in oxidative reduction (EE/O) for each 1 m^3 of treated fluid. Reports comparing treatment processes on this basis (23, 24) indicate that the high energy consumption of UV-lamps account for a large portion of the running costs. Further, it has been demonstrated that reactor hydrodynamics and lamp position are crucial to optimize the yield of UV radiation and ensure quality (5). With UV power consumption as a main cost factor, over specification of the lamp power output is not a viable option; yet guaranteed constant water quality is crucial for health reasons and cannot be compromised. An in-depth understanding of UV-reactors based on validated models is therefore needed to ensure efficient reactor designs.

Since the radiation field, defined as the fluence rate (E) and given by the spatial location and operating conditions of the lamp(s), is non-uniformly distributed and reaction rates in UV-reactors are a function of both the local fluence rate and concentration of contaminant(s), reactor performance is dependent on both residence time and the hydrodynamic flow through the reactor geometry. Thus, a general model that can be used to improve the UV-reactor design has to take the actual flow field information inside the reactor into account. Computational Fluid Dynamics (CFD) makes the development of such models possible by mathematically solving the momentum and mass conservation equations that govern the flow inside a defined domain. Finally, reactor performance can be computed by integrating hydrodynamics with radiation distribution and UV reaction kinetics submodels.

1.1 Literature review

1.1.1 Safe drinking water

Improper waste disposal, slack quality control, aging or missing distribution systems, and other factors can lead to the contamination of drinking water supplies. Headlines about the loss of human life connected to *E.Coli* and *Cryptosporidium paryum* oocysts are reminders that clean water is very much a current issue. Less tragic, but in many ways even more thought provoking, are reports of endocrine disrupters such as estrogen (birth control hormone) found in water streams (32).

Endocrine disrupters have been linked to gender changes occurring in fish and invertebrates and are under investigation. Indeed, over the last decade most countries have introduced intensified legislative measures to monitor and remove contaminants that present health risks and are known, or likely to occur, in public drinking water supplies.

The widely publicized incidences of illness and even deaths occurring in the US and Canada due to bacterial and parasite infections (*Cryptosporidium* in Milwaukee,Wi, USA (1993) and *E.Coli* in Walkerton, Ontario, Canada (2000)) were traced back to the contamination of drinking water. These high profile cases (29) heightened the awareness in the public and scientific community to chlorine resistant microorganisms and have since led to changes and additions to the Safe Drinking Water Act (USA) (30), with many other countries taking similar steps.

The new guidelines were introduced, in large part, to govern the development and implementation of (new) drinking water treatment processes that achieve a favorable balance between the risk of possible contamination, cost of ownership, and possible negative treatment impacts such as the formation of disinfection byproducts (DBPs).

1.1.2 Methods of water treatment and new approaches

The use of UV-radiation for disinfection purposes is undisputed (13), but the newer challenge of removing trace contaminants has yet to be dealt with. The fact that biological treatment and conventional chemical oxidation have low removal rates for many environmental contaminants (e.g. MTBE (36)), led to the development of alternative methods in order to cost-effectively meet the new environmental standards.

One such group of technologies is referred to as Advanced Oxidation Processes (AOPs). They involve the generation of a powerful but non-selective transient oxidation species, primarily the hydroxyl radical ($^{\bullet}OH$) which has one of the highest thermodynamic oxidation potentials (Table 1.1). Hydroxyl radicals can be generated in several ways, with photochemical processes showing great potential. The production of $^{\bullet}OH$ radicals, through irradiation of hydrogen peroxide (H_2O_2) with UV, is of special interest, since these reactors are very similar to those used for

UV-disinfection, but with much higher fluence rates.

Table 1.1: Oxidation potential of several oxidants in water

Oxidant	Oxidation Potential (eV)
$^{\bullet}OH$	2.80
O_3	2.42
H_2O_2	1.77
Cl	1.36
O_2	1.23

1.1.3 UV-reactors

While UV-radiation in disinfection reactors directly affects the target microorganisms, advanced oxidation reactors need to bring UV-radiation in conjunction with a strong oxidant (e.g. H_2O_2) to generate the fast reacting intermediate oxidizing agent ($^{\bullet}OH$). There are many ways to design UV-reactors (7, 15), but a recurring design concept for simpler reactors consist of submerged UV-lamp(s) in a tubular body. Annular reactor designs, where a UV lamp is installed concentric and parallel to the reactor body, are currently used for many small to medium-sized single lamp products (6, 25). One of the challenges in modeling reactors with spatially dependt reaction rates is the impact of the fluid flow field on the reactor performance. For instance microorganisms with similar residence times can absorb different amounts of UV-dose, depending on their path through the reactor. UV-reactor modeling approaches have made use of simplified hydrodynamics for the cases of fully developed laminar flows (10), fully mixed conditions (8) and tanks in series (19, 27). Application of these models, while valuable under the stated restrictions, are questionable in the case of the more prevalent turbulent flows found in many industrial continuous flow reactors. The influence of hydrodynamics on the performance of UV-reactors has been widely acknowledged (21) underlining the importance of detailed flow field information for the design and optimization of UV-reactors. Analyzing the interactions of photo-reactors therefore involves at least three (sub) models, linked by material and energy balances:

1. A hydrodynamic model

2. A radiation emission/distribution model

3. A kinetic model (disinfection or advanced oxidation)

each of which will be treated separately in what follows.

Due to the increasing power of computers, Computational Fluid Dynamics (CFD) has become an efficient tool to simulate fluid flow behavior in complex geometries. CFD is based on the numerical solution of partial differential equations (PDEs), expressing the local balances of mass, momentum and energy, potentially coupled to the transport equations of the reacting species. However, such PDEs could include phenomenological terms that should be adjusted to provide the correct results. For example, turbulent stresses are computationally expensive to calculate and several models have been developed, describing time-averaged (simplified) results. The choice of an adequate approximation lies with the model operator. Since the accuracy of CFD simulations is dependent on choices made during the model setup, experimental validation by measuring flow characteristics would be preferable.

1.1.4 Particle image velocimetry (PIV)

Particle Image Velocimetry (PIV) is currently one of the most advanced experimental methods to visualize and measure flow characteristics. The general principle of PIV is to illuminate tracer particles in the flow field of interest with a two dimensional sheet of laser light and acquire two images of the flow field with a known time separation. The velocity field is determined from the distance traveled by the tracer particles between the two images, divided by the known time interval.

1.1.4.1 A short history

The year 2004 marked the 20th anniversary of particle image velocimetry. PIV has enjoyed a long and adventurous journey from the early roots beginning in 1977 when Laser Speckle Velocimetry (LSV) was demonstrated to measure flow fields. In 1984, R.J Adrian (1) pointed out that the illumination of particles in a fluid flow by a light sheet would almost never create a speckle pattern. The image would rather show the tracks of individual particles, hence making particle image velocimetry possible. The initial groundwork to modern PIV was then laid down by Adrian (17), who described the expectation value of an auto-correlation function

for double-exposure continuous PIV images. Later the theory was generalized to include exposures over multiple recordings (16).

To visualize and study the structure of turbulent flow, the particles must be able to follow the flow, including small-scale local turbulence. This implies the use of very small particles, a few tens of microns in diameter for liquids, which in turn necessitates the use of high intensity illumination to compensate for the small light scattering cross-section. Coupled with the short time exposures needed to prevent blurring, the only viable solution was the use of high intensity pulsed lasers.

There still remained the problem of processing the obtained data. Initial methods relied on the determination of two-dimensional correlations by analog optical means. With the advent of computers, enough computing power was available to perform the two-dimensional Fourier transform needed for the auto-correlation methods.

One of the most important changes in PIV was the move from photographic to digital image recording. Westerweel's (33) proof of concept, showing that digital PIV was as accurate as film PIV, did much to reduce initial concerns on the much lower resolution of digital images. The fast evolution of digital cameras has surpassed 1000x1000 pixel resolution and is currently approaching levels equivalent to that of 35 mm films.

The second important change was the introduction of interline transfer cameras, as these cameras can record two images only microseconds apart. Thus many problems associated with double-exposed (single) pictures could be addressed. The need for image shifting was eliminated, since the direction of the flow was determined automatically by the order of the images. Auto-correlation, known to be superior to cross-correlation, was finally feasible with digital images and fast computers. Separate images allowed the resolution of movements smaller than a full particle diameter, increasing the dynamic range, defined as

$$\text{dynamic range} = \frac{\text{maximum measurable velocity}}{\text{minimum measurable velocity}} \tag{1.1}$$

by an order of magnitude, enough to resolve even turbulent flows. Presently, the single camera, planar light sheet, cross-correlation PIV with a double-pulsed Neodymium-doped Yttrium Aluminum Garnet (Nd:YAG) laser and 2kx2k cross

correlation camera is standardly used and sold commercially. These systems have enough spatial resolution and dynamic range to resolve turbulent flow fields. But the dynamic range of currently no more than 200:1 is still small enough to make PIV experimental investigations exercises in optimization. PIV results have been used to validate CFD simulations in the airplane and car industries for some time now (34). Studies of turbulent flows in rectangular (14) and tubular channels (26), have been published for dimensions and flow conditions similar to those used in this study.

1.1.5 CFD

Computational fluid dynamics, CFD, solves the following conservation equations:

$$\frac{\partial u_i}{\partial x_i} = 0 \tag{1.2}$$

and momentum conservation:

$$\frac{\partial u_i}{\partial t} + u_j \frac{\partial u_i}{\partial x_j} = -\frac{1}{\rho}\frac{\partial p}{\partial x_i} + \mu \frac{\partial^2 u_i}{\partial x_j \partial x_j} \tag{1.3}$$

that govern the flow. These equations are based on the assumption of Newtonian fluids with constant medium properties . The computational domain is discretized (or meshed) into a number of small cells (finite volumes). In the meshed computational domain, the PDEs are approximated as a set of algebraic equations that can be solved numerically. Meshing of the domain is crucial, can be very time consuming, and needs a good initial understanding of the investigated volume. For the finite volume method employed by many commercial CFD software packages, such as Fluent, this consists of:

- Formal integration of the governing equations of fluid flow over all the (finite) control volumes of the solution domain.
- Discretisation involving the substitution of a variety of finite-difference type approximations for the terms in the integrated equation representing flow processes such as convection, diffusion and sources. This converts the integral equations into a system of algebraic equations.

- Solution of the algebraic equations by an iterative method.

1.1.6 Turbulence modeling

The direct numerical solution (DNS) of the governing Navier-Stokes equations is not possible for most applications involving turbulent flows, because of the wide range of time and length scales involved (Figure 1.1). To describe the mean flow

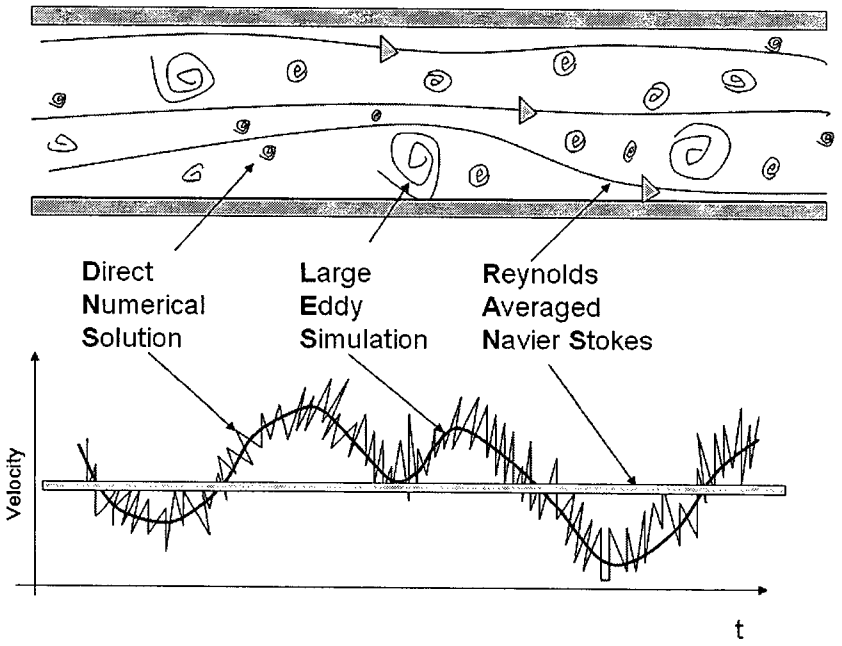

Figure 1.1: Schematic representation of scales in turbulent flow and their relationship to modeling approaches

field, it is possible to time-average the governing equations through Reynolds decomposition, resulting in the Reynolds Averaged Navier-Stokes (RANS) equations :

$$\frac{\partial \bar{u}_i}{\partial x_i} = 0 \tag{1.4}$$

$$\frac{\partial \bar{u}_i}{\partial t} + \bar{u}_j \frac{\partial \bar{u}_i}{\partial x_j} = -\frac{1}{\rho}\frac{\partial \bar{p}}{\partial x_i} + \mu \frac{\partial^2 \bar{u}_i}{\partial x_j \partial x_j} - \frac{\partial}{\partial x_j}\overline{u_i' u_j'} \tag{1.5}$$

These equations have the same general form as the instantaneous Navier-Stokes equations except for the new term $-\rho\overline{u_i' u_j'}$, called the Reynolds stress tensor. This

term is usually negative and represents the effect of smaller scale motions on the mean flow. It acts as an additional stress and dominates the transport processes by several orders of magnitude over molecular transport. To close the RANS equations, individual Reynolds stress components can be solved throughout the flow field. This is computationally expensive because the Reynolds stresses are tensor quantities. Reynolds stress is a higher-order moment that has to be modeled in terms of the knowns. This is referred to as the closure approximation, the challenge of which lies in the representation of the unknown terms in a way that mimics the real physics of the small turbulent length scales as close as possible.

1.1.6.1 Eddy viscosity concept

Boussinesq (1885) hypothesized a relationship between the Reynolds stressed and mean velocity gradients of the flow by assuming isotropy of the stresses, i.e.,

$$-\overline{u_i' u_j'} = \mu_t \left(\frac{\partial \bar{u}_i}{\partial x_i} + \frac{\partial \bar{u}_j}{\partial x_i} \right) - \frac{2}{3} \kappa \delta_{ij} \tag{1.6}$$

where μ_t is the turbulent or eddy viscosity similar to the molecular viscosity, except that it is a flow property and depends on the local state of turbulence. κ is the turbulent kinetic energy per unit mass and the term The idea behind this hypothesis is that momentum transfer in turbulent flows is dominated by the mixing caused by large eddies. Turbulent eddies are visualized as molecules, colliding and exchanging momentum and thus, can be derived analogous to the molecular transport of momentum as described by the kinetic theory of gases. This is quite bold, since the mean free path between molecules is large compared to turbulent eddies that can be assumed to be on the same order as the flow scales. Despite these differences, models based on the Boussinesq hypothesis perform well in many cases.

Prandtl (1925) proposed a mixing-length model for μ_t analogous to the kinetic theory of gases where the turbulent viscosity can be related to the characteristic velocity of turbulence V and a length scale of turbulence called the mixing length l_m, i.e.,

$$\mu_t \propto V l_m \tag{1.7}$$

Prandtl proposed this in the context of a turbulent shear layer with only one mean gradient $\partial\bar{u}_1/\partial x_2$. He suggested that the turbulent fluctuations can be expressed as:

$$V = l_m \left| \frac{\partial \bar{u}_1}{\partial x_2} \right| \tag{1.8}$$

allowing the turbulent viscosity to be expressed as:

$$\mu_t = l_m^2 \left| \frac{\partial \bar{u}_1}{\partial x_2} \right| \tag{1.9}$$

l_m is usually specified, from experimental knowledge, as constant across the shear layer for most of the thin shear layers, and takes a different value in the boundary layers to account for the different layers. This is not a very suitable closure method since difficulties arise in determining the missing length for complicated flows. Mixing length models typically fail in predicting flow separations, because large eddies persist in the mean flow and cannot be modeled from local properties alone. This is a so-called zero equation model because no additional equations are needed for closure.

As an improvement to the above closure problem, transport equations are generally solved to specify the turbulent velocity and length scales involved. Depending on the number of additional equations solved, they are called one or two equation models. κ-ϵ models are two-equation models since they require the solution of both the turbulent velocity and the length scale.

1.1.6.2 Standard κ-ϵ model

This family of models is widely used in turbulence simulations because of its general applicability. It is a two equation model, in which transport equations are solved for turbulent kinetic energy κ, and instead of modeling the length scale itself they use the turbulent energy dissipation rate ϵ where:

$$\epsilon = \kappa^a l_m^b \tag{1.10}$$

This approach is preferred by engineers since it does not require a secondary source and the simple gradient diffusion hypothesis is fairly accurate. In this model the

turbulent viscosity is related to κ and ϵ by the following equation:

$$\mu_t = \rho C_\mu \frac{\kappa^2}{\epsilon} \tag{1.11}$$

where C_μ is an empirical coefficient. To close the equation, the local values of κ and ϵ are obtained by solving their transport equations. These can be derived from the Navier-Stokes equations of which a detailed description can be found in "Lectures in Mathematical Modeling of Turbulence" (20). In essence the turbulent diffusivity of κ and ϵ are related to the turbulent viscosity with additional empirical constants, which are known as turbulent Prandtl numbers for κ and ϵ. The final model contains 4 empirical parameters that have been determined experimentally by Launder and Spalding (20).

The standard κ-ϵ model has some limitations and drawbacks since this is a semi-empirical model. The equation for ϵ is based on physical reasoning while the model equation for κ is derived mathematically. One of the problems encountered is the fact that the equation does not ensure that turbulent normal stresses are positive, which is contradictory to real physics.

1.1.6.3 Realizable κ-ϵ model

The realizable κ-ϵ model is an improvement over the standard model with certain mathematical constraints on the Reynolds stresses, consistent with the physics of turbulent flows. It has a new formulation for ϵ that is derived from the exact equation for the transport of the mean-square vorticity fluctuation. It outperforms the standard κ-ϵ model for flows involving rotation, boundary layers under strong adverse pressure gradients, and recirculation. Even so, it pays to keep the underlying assumptions of all κ-ϵ models in mind:

- Turbulence is assumed to be nearly isotropic
- The spectral distributions of turbulent quantities are assumed to be similar
- It is true only at high Reynolds numbers

These assumptions may not be valid for the flows encountered in practical environments. Also, all κ-ϵ based models tend to over-predict turbulence generation

in regions of high acceleration and deceleration where the isotropic assumption no longer holds.

1.1.6.4 Reynolds stress model (RSM)

The one and two-equation models presented assume that the principal axes of both the Reynolds stress tensor and the mean strain-rate tensor are coincident everywhere in the flow. This Boussinesq approximation weakens in flows with sudden changes in the mean strain rate, flows with strong curved surfaces, flows with separation, and flows with three-dimensional features. A Reynolds stress model, in theory, will circumvent the deficiencies of the Boussinesq approximation. The individual Reynolds stresses are calculated directly using differential transport equations and solution of the ϵ equations provides the remaining turbulent scale to obtain closure of the Reynolds-averaged momentum equation. This second-order moment closure method offers an advantage over scalar eddy viscosity approaches in that the transport equations possess several exact terms and, therefore, a closer connection to the exact equations. Reynolds stress transport modeling also formally accounts for the effects of streamline curvature, and rapid changes in strain rate more rigorously than one- and two-equation models. While possessing more exact terms, the computational cost of the calculation is substantially greater, as the approach requires solutions of seven additional transport equations. Also, the model is not fully mechanistic and contains empirical constants (e.g., in the pressure and dissipation terms). A tendency to require denser mesh, higher computational costs, and the fact that, in many cases, it does not perform better than the two equation models have to be weighed against the stated advantages.

1.1.6.5 Choosing a turbulence model

No turbulence model is universally applicable to all conditions. Therefore, it is important to chose an appropriate turbulence model for each application at hand, be sure to understand the underlying assumptions, and if possible perform a model validation.

Generally, any of the two equation κ-ϵ models are recommended as a starting baseline model. Once unsteady vortex shedding is involved, the Realizable-κ-

ϵ version of the κ-ϵ model should be used. For more complex flows including curved flows and rotating flows, the computationally more expensive Reynolds Stress Model (RSM) might be considered. Due to the numeric stability of the standard κ-ϵ model, it is often used as the starting point for subsequent changes in turbulence model choice. It should also be noted that, for many industrial solutions, the grid resolution might have a higher impact than the turbulence model used.

1.1.6.6 Summary

CFD calculations are influenced by parameters such as mesh size and structure, mathematical discretisation method used, and the choice of turbulence models. Accordingly, calculations should be verified experimentally before integrating further components into the model.

1.2 Research objectives

The objectives of this thesis are to study the fluid flow of water in annular UV reactors, both experimentally and through CFD simulations, with the aim of identifying key parameters to achieve verified CFD flow field calculations. A two-dimensional flow visualization technique, Particle Image Velocimetry (PIV), is used to obtain the main hydrodynamic characteristics of the given flow configurations. A UV reactor performance model is then established by integrating hydrodynamics with radiation and reaction rate submodels. The objectives are achieved through the following steps:

1. Identify typical annular reactor designs and establish plexiglas prototypes for flow visualization.

2. Develop an experimentally substantiated understanding of the flow field inside the UV-prototype reactors by means of particle image velocimetry (PIV).

3. Establish the computational hydrodynamics of UV-reactors through CFD models and study the influence of model assumptions. Assess the validity of the flow prediction through comparison with PIV results.

4. Adapt and integrate UV-radiation models for mesh-based CFD calculations.

5. Develop a general, particle based (Lagrangian) model, coupling UV-radiation and reaction kinetics to reactor hydrodynamics to simulate overall UV disinfection performance.

6. Develop a model based on volumetric reaction rates (Eulerian), that is capable of handling more than single step reactions (applicable for advanced oxidation).

7. Evaluate and compare integrated UV reactor performance models.

What follows are the three research chapters composing the main body of this thesis. Objectives 1 and 2 are the focus of Chapter 2 with the title "Experimental investigation of flow fields in annular UV-reactors using PIV". Chapter 3 with the title "CFD study of annular UV-reactor hydrodynamics" concentrates on Objective 3. Finally Objectives 4 to 7 are addressed in Chapter 4, entitled "Integrated UV reactor model development". Chapter 5 summarizes conclusions and recommendations.

Bibliography

[1] ADRIAN, R. J. *Probability density of turbulence from multiple field Particle Image Velocimetry.* Fifth Symposium on Turbulent Shear Flows., Ithaca, NY, USA, 1985, pp. 11–7. Compilation and indexing terms, Copyright 2004 Elsevier Engineering Information, Inc.

[2] ARBUCKLE, T. E., HRUDEY, S. E., KRASNER, S. W., NUCKOLS, J. R., RICHARDSON, S. D., SINGER, P., MENDOLA, P., DODDS, L., WEISEL, C., ASHLEY, D. L., FROESE, K. L., PEGRAM, R. A., SCHULTZ, I. R., REIF, J., BACHAND, A. M., BENOIT, F. M., LYNBERG, M., POOLE, C., AND WALLER, K. Assessing exposure in epidemiologic studies to disinfection by-products in drinking water: report from an international workshop. *Environ Health Perspect 110 Suppl 1* (Feb 2002), 53–60.

[3] BOLTON, J. R., BIRCHER, K. G., TUMAS, W., AND TOLMAN, C. A. Figures-of-merit for the technical development and application of advanced oxidation technologies for both electric- and solar-driven systems. *Pure and Applied Chemistry 73* (2001), 627–637.

[4] BOLTON, J. R., AND BIRCHNER, K. G. Figures of merit for the technical development and application of advanced oxidation processes. *Journal of Advanced Oxidation Technologies 1* (1996), 13–17.

[5] BOLTON, J. R., WRIGHT, H., AND ROKJER, D. Using a mathematical fluence rate model to estimate the sensor readings in a multi-lamp ultraviolet reactor. *Journal of Environmental Engineering and Science 4* (January 2005), 27–31. Supplement 1.

[6] BRAUN, A., JAKOB, L., AND OLIVEROS, E. Advanced oxidation processes - concepts of reactor design. *Journal of Water Supply: Research and Technology-AQUA 42*, 3 (1993), 166–173.

[7] CASSANO, A. E., MARTIN, C. A., BRANDI, R. J., AND ALFANO, O. M. Photoreactor analysis and design: Fundamentals and applications. *Industrial & Engineering Chemistry Research 34* (1995), 2155–201.

[8] CHANG, P. B. L., AND YOUNG, T. M. Kinetics of methyl tert-butyl ether degradation and by-product formation during uv/hydrogen peroxide water treatment. In *Proceedings of the Air & Waste Management Association's Annual Conference & Exhibition, 93rd, Salt Lake City, UT, United States, June 18-22, 2000* (2000), pp. 7036–7055.

[9] CLARKE, N., AND KNOWLES, G. High-purity water using hydrogen peroxide and uv radiation. *Effluent & Water Treatment Journal 22* (1982), 335–8, 340–1.

[10] ELKANZI, E. M., AND KHENG, G. B. H2o2/uv degradation kinetics of isoprene in aqueous solution. *Journal of Hazardous Materials 73* (2000), 55–62.

[11] ESPLUGAS, S. Economic aspects of integrated (chemical + biological) processes for water treatment. *Journal of Advanced Oxidation Technologies 2* (1997), 197–202.

[12] GOGATE, P. R., AND PANDIT, A. B. A review of imperative technologies for wastewater treatment. ii: Hybrid methods. *Advances in Environmental Research 8* (2004), 553–597.

[13] HANZON, B., AND VIGILIA, R. Uv disinfection. *Wastewater Technology Showcase 2*, 3 (1999), 24–28.

[14] ISLAM, M. S., HAGA, K., KAMINAGA, M., HINO, R., AND MONDE, M. Experimental analysis of turbulent flow structure in a fully developed rib roughened rectangular channel with piv. *Experiments in Fluids 33* (2002), 296–306.

[15] KARPEL VEL LEITNER, N., LE BRAS, E., FOUCAULT, E., AND BOUSGARBIES, J.-L. A new photochemical reactor design for the treatment of absorbing solutions. *Water Science and Technology 35* (1997), 215–222.

[16] KEANE, A., AND ADRIAN, R. Particle-imaging techniques for experimental fluid mechanics. *Annual Review of Fluid Mechanics* (1991).

[17] KEANE, R., AND ADRIAN, R. Optimization of particle image velocimeters part i double pulsed systems. *Measurement and Technology 1*, 11 (November 1990), 1202–1215.

[18] KIDMAN, R., AND TSUJI, K. Preliminary costs comparison of advanced oxidation processes. Tech. rep., Los Alamos National Laboratory, 1992.

[19] LABAS, M. D., ZALAZAR, C. S., BRANDI, R. J., MARTIN, C. A., AND CASSANO, A. E. Scaling up of a photoreactor for formic acid degradation employing hydrogen peroxide and uv radiation. *Helvetica Chimica Acta 85* (2002), 82–95.

[20] LAUNDER, B. E., AND SPALDING, D. B. *Lectures in mathematical modeling of turbulence.* Academic Press, London, 1972.

[21] LAWRYSHYN, Y. A., AND CAIRNS, B. Uv disinfection of water: the need for uv reactor validation. *Water Science & Technology: Water Supply 3* (2003), 293–300.

[22] LETTERMAN, R. *Water quality and treatment - A Handbook of community water supplies (5th Edition).* McGraw-Hill, 1999.

[23] MUELLER, J. P., AND JEKEL, M. Comparision of advanced oxidation processes in flow-through pilot plants (parti). *Water Science and Technology 44*, 5 (2001), 303–309.

[24] MUELLER, J. P., AND JEKEL, M. Comparision of advanced oxidation processes in flow-through pilot plants (partii). *Water Science and Technology 44*, 5 (2001), 311–315.

[25] OPPENLAENDER, T. *Photochemical purification of water and air.* Wiley-VCH, 2003.

[26] PRUVOST, J., LEGRAND, J., LEGENTILHOMME, P., AND DOUBLIEZ, L. Particle image velocimetry investigation of the flow-field of a 3d turbulent annular swirling decaying flow induced by means of a tangential inlet. *Experiments in Fluids 29* (2000), 291–301.

[27] PUMA, G. L., AND YUE, P. L. Modeling and design of thin-film slurry photocatalytic reactors for water purification. *Chemical Engineering Science 58* (2003), 2269–2281.

[28] RADCLIFF, R. International drinking water regulations:the developed world sets the standards. *On Tap Magazine Spring* (2003).

[29] RITTER, L., SOLOMON, K., SIBLEY, P., HALL, K., KEEN, P., MATTU, G., AND LINTON, B. Sources, pathways, and relative risks of contaminants in surface water and groundwater: a perspective prepared for the walkerton inquiry. *Journal of Toxicology and Environmental Health, Part A 65* (2002), 1–142.

[30] USEPA. *Clean water act.* US-EPA, 1996. http://www.epa.gov/safewater/sdwa/index.html.

[31] USEPA. 1999 drinking water infrastructure needs survey. modeling the cost of infrastructure. Tech. rep., US-EPA, February 2001.

[32] Vos, J. G., Dybing, E., Greim, H. A., Ladefoged, O., Lambre, C., Tarazona, J. V., Brandt, I., and Vethaak, A. D. Health effects of endocrine-disrupting chemicals on wildlife, with special reference to the european situation. *Critical Reviews in Toxicology 30* (2000), 71–133.

[33] Westerweel, J. *Digital particle image velocimetry: Theory and application.* PhD thesis, Universityof Delft, 1993.

[34] Wu, H. L., Peng, X. F., and Chen, T. K. Influence of sleeve tube on the flow and heat transfer behavior at a t-junction. *International Journal of Heat and Mass Transfer 46* (2003), 2637–2644.

[35] Wulf, W. A. Great achievements and grand challenges. *The Bridge 30*, 3&4 (2000), 6–11.

[36] Yeh, C. K., and Novak, J. Anaerobic biodegradation of gasoline oxygenates in soils. *Water Environment Research 66*, 5 (1994).

Chapter 2

Experimental investigation of the flow field in annular UV reactors using PIV

In this chapter, the experimental investigation of flow in different annular UV reactors will be discussed. Starting with the underlying ideas of the experiment, Particle Image Velocimetry (PIV) is introduced. Considering that PIV is a new entrant in the field of fluid flow measurements, some topics concerning this method are covered in more detail.

2.1 Introduction

Annular UV-reactors have become more popular over the last few years, mainly due to the successful introduction of UV-photoreactors for water disinfection and advanced oxidation processes (AOPs) for the removal of organic contaminants. These reactors use UV radiation to either directly affect hazardous organisms for water disinfection or to excite a strong oxidant such as H_2O_2 or O_3 to generate highly reactive hydroxyl radicals in situ, which in turn oxidize (toxic) organic substances. The design of photoreactors is largely determined by the radiation distribution field and thus, the placement of UV-lamp(s) as radiation sources. The annular reactor, a cylinder with a concentric lamp parallel to the reactor body,

strikes a good balance between the lamp placement and reactor geometry for small to medium single lamp systems and is the basic design for many current products (2, 15).

Many annular reactor designs use a horizontal cylindrical body and variations in the placement of the inlet and outlet tubes. The resulting typical reactor outlines resemble the letters S, U and L and are the source of the descriptive names (Figure 2.1):

- U-shape: inlet and outlet are normal to the reactor axis, parallel and in the same direction (e.g. top inlet and outlet)
- L-shape: inlet is parallel and co-centric to the reactor axis, the outlet is normal to the reactor axis (e.g. front inlet, top outlet)
- S-shape: inlet and outlet are normal to the reactor axis, parallel and in opposite directions (e.g. top inlet, bottom outlet). This is a variant of the U-shape reactor.

The central lamp is commonly entered through an end cap and needs to be fixed in place at the opposite end. For the L-shape reactor, a lamp support structure (lamp holder) is required near the reactor entrance.

The design of reactors containing radiation fields to initiate the desired reaction is a relatively new area of research, but the numbers of recent publications show an increasing interest. The main challenge of operating under non-uniform concentration and radiation distributions is the highly non-uniform local rate of reaction (3), resulting in a high impact of the fluid flow field on reactor performance. For example, a bacteria passing through a badly designed reactor may not spend enough time in the volumes close to the radiation source and will most likely not receive a high enough dose to be inactivated.

Simplified models have been established for modeling UV-reactor hydrodynamics using fully developed laminar flows (7), fully mixed conditions (4), or tanks in series (12). While these models are valuable under the stated restrictions, their application to the more prevalent non-uniform flows in industrial continuous flow reactors is questionable. The link between hydrodynamics, radiation distribution and the reaction rate greatly increases the complexity of the models simulating

UV-reactor performance. In particular, the influence of the flow field on the performance of UV-photoreactors has been widely acknowledged (13). This underlines the importance of detailed flow-field information for performance analysis and design optimization of UV-reactors.

There have been some efforts using Computational Fluid Dynamics (CFD) to simulate the flow fields in UV-reactors (10, 11, 14); however, none of these studies conducted experiments to evaluate the CFD modeling results. Using CFD, the governing equations of mass and momentum conservation are solved iteratively in a discretized representation of the computational domain. CFD results are influenced by several parameters such as discretisation method, mesh structure and the choice of turbulence models for the momentum conservation equations. As a result, the CFD models need to be validated against reliable experiments. The hydrodynamics of UV water treatment systems have been studied experimentally to some degree. Schoenen et al. (17) demonstrated the effect of the reactor flow field on the performance of water disinfection systems. Chiu et al. (5) used laser Doppler velocimetry to experimentally obtain velocity information in a cross-flow UV-reactor. Despite these limited studies, no detailed experimental information covering a range of flow rates and reactor geometries is currently available for UV-reactors.

Particle Image Velocimetry (PIV) is one of the most advanced experimental methods available to visualize the main flow characteristics of a given configuration. It provides a non-intrusive measurement of the instantaneous planar velocity field over a global domain. As the name suggests, it records the position of small tracer particles over time to extract the local fluid velocity. PIV requires four basic components: an optically transparent test-section containing the seeded fluid, an illuminating light source (laser), a recording device (CCD camera) and a computer algorithm to process (cross-correlate) the recorded images (1). PIV has been widely used in the aviation and automobile industry and there have been some studies of turbulent flows in rectangular (9) and tubular channels (16). PIV results have also been used to evaluate CFD simulations (19). To the author's knowledge, no work has been reported in the open literature on the study of flow-fields in photoreactors.

This work presents a study of the annular UV-reactor hydrodynamics and determines the time-averaged turbulent flow field using PIV in two (U- and L- shape)

full-scale Plexiglas reactor models. Flow structures in the inlet region of both reactors are described in detail for a range of flow rates. The influence of lamp position and holder position for the L-shape reactor are determined. For the U-shape reactor, the time dependency of the flow at the inlet plane perpendicular to the axis is demonstrated.

2.2 Experiments

2.2.1 Experimental setup

Figure 2.1 shows a schematic of the experimental setup. A 100 L reservoir connected to a centrifugal pump was used to circulate distilled water through the test section in a closed loop. The flow rate at the reactor inlet was measured and adjusted by a flow-meter (Cole-Parmer, 5-25 GPM). Full scale Plexiglas models of the complete configuration for U- and L-shape reactors, with internal components including the quartz lamp-sleeve and lamp-holder were used for the PIV measurements. Both test sections (reactors) share major dimensions based on existing industrial designs for an estimated throughput of 40 L/min ($\approx$ 10 GPM). The test rig was designed as a modular system with a central tube internal diameter (ID) of D_1=8.89 cm (3.5 inches) and a reactor length of L=88.9 cm (35 inches). Both end-caps were designed to be removable, facilitating the change of reactor configurations. The inlet and outlet ports with an ID of D_2=1.91 cm (0.75 inch) were placed 2.54 cm (1 inch) from each respective end for the U-shape. The L-shape inlet was centred on the front-plate (Figure 2.2).

A concentric quartz tube of outer diameter (OD) D_3=2 cm (0.788 inches) was used to represent the UV-lamp sleeve with minimal optical interference on the laser sheet. The sleeve entered the reactor volume through a Teflon seal (Swagelok) and remained readily movable along the reactor axis. A cylindrical extrusion was used to fix the opposite end of the UV-sleeve for the U-shape, while a three pronged holder fixed the lamp sleeve concentric to the reactor tube for the L-shape reactor (Figure 2.2). The holder, a concentric ring of 0.3 cm thickness and a length of 1.52 cm (0.6 inch) with three radial cylindrical struts of 0.5 cm (0.2 inch) diameter, was slipped over the lamp with the struts centered at 18.5 cm (7.3 inches) from the

inlet. The holder's side-faces were minimized and the edges beveled to minimize exposure to the flow. The mean flow rates varied between Q=2.52×10^{-4} m^3/s (≈4 GPM) and Q=6.94×10^{-4} m^3/s (≈11 GPM). For the majority of the measurements Q=6.94×10^{-4} m^3/s, corresponding to a mean axial velocity of 0.11 m/s and a Reynolds number Re=10,000, was examined.

The annular reactor's were placed within a Plexiglas tank (130 cm×30 cm×30 cm) filled with distilled water, to eliminate optical distortion caused by the reactors curved external surface (see Appendix A for details). The whole experimental apparatus was finally placed on an extruded aluminum structure, consisting of a central table with two movable side planes and one movable top plane, all equipped with XY linear slides. This allowed the laser and the camera to be placed and moved at a consistent 90 degree angle.

2.2.2 PIV measurement system

Table 2.1 gives an overview of the PIV system specifications (Flow-Map 2D, Dantec Dynamics). The PIV illumination system consisted of a dual head Nd:YAG laser (New Wave Research: Model SoloIII-15 Hz) emitting 10 ns pulses with maximal energies of up to 50 mJ/pulse. The collinear frequency doubled beam (1064 nm to 532 nm) was spread into a sheet of 1-2 mm thickness through a set of cylindrical lenses directly attached to the laser head. The particle images were recorded on a high-resolution progressive scan interline CCD camera (Hamamatsu: HiSense MkII) at a maximum rate of 5 Hz. The camera with a resolution of 1344×1024 pixels and a 12 bit dynamic range, was fitted with a 514 nm line filter to minimize stray light. The camera and the laser were connected to a PIV hub with a frame grabber and 1.0 GB RAM to buffer the image stream. The hub's programmable synchronizer controlled the timing of the laser illumination and the camera image acquisition. The hub connected to a PC, where the experimental sequence was programmed and the resulting data stream was analyzed asynchronously (Figure 2.1).

2.2.3 Experimental procedures

For the PIV measurements, the time interval between two laser pulses was adjusted between 600 and 1500 μs. Tests concerning the number of images needed to get accurate time-averaged measurements were performed by taking a series of 1600 instantaneous velocity field measurements. Vector statistics of samples containing the full set and subsets of 800, 400, 200 and 100 images were compared. It was found that a sample size of about 200 images produce a stable time-averaged result. All further measurements were therefore performed with 250 or more image pairs for the best measurement accuracy. The amount of seeding ($\approx$50 mg/L) was determined by allowing not less than 10 particles per interrogation window. Small interrogation window sizes are desirable to resolve small turbulent flow structures, but require a high number of particles and are more sensitive to high velocity gradients. The influence of window size on the adaptive cross-correlation algorithm was evaluated. It was found that a final window size of 16×16 pixels with 50% overlap and two adaptation steps could be applied without loss of accuracy. A measurement rate of 0.1 Hz was chosen to minimize the influence of longer term fluctuations.

The accuracy of the velocity measurements was determined through statistical analysis over the 250 instantaneous vector fields at several points. Small errors (95% confidence interval) of less than 1% were determined for the high velocities at the inlet. The relative errors were found to be less than 5% for the intermediate flow rates at 10 cm from the reactor inlet, and around 17% for the low axial flow speeds at 23 cm and beyond (Figures 2.5a-c). At low flow rates, any gains in accuracy from longer Δt intervals were offset through the out-of-plane loss of particles.

The configuration of the test sections allowed for a maximum possible number of planes to be observed; however, parts of the reactor were blocked by obstacles in the path of either the laser or camera. The planes of interest, parallel and perpendicular to the main reactor flow, were specified for each reactor. The center planes were accessible to both laser and camera, which allowed the capture of the major flow characteristics in both test sections. The inlet region, with high gradients of flow velocities and high impact in determining the overall flow, was given the most attention. Viewable areas covered by one camera position were

determined by the CCD resolution and reactor height, resulting in oblong windows of 11 × 8.9 cm.

2.3 Results and discussions

In the statistical description of turbulence, the total instantaneous velocity is decomposed into its time-averaged velocity component and a turbulent fluctuation component. Using the large time resolved velocity data sets from PIV, it is possible to investigate both components in any direction in a planar field. Single instantaneous velocity fields show the characteristics of raw measurements, but deliver little information for understanding the fundamental flow physics. The mean (time-averaged) PIV velocity fields discussed here, trade off instantaneous (temporal) information for the time-averaged flow distribution, in order to visualize only the prevailing flow structures inside the reactor. The turbulent fluctuations remain accessible as statistical measures of local interactions due to unsteady behavior. Further information such as turbulent kinetic energies and vorticity which could be calculated from the same set of flow field data will not be discussed. The two test section geometries are presented separately starting with the L-shape reactor.

2.3.1 L-shape reactor

Figure 2.3a-b shows the composite time-averaged PIV measurements obtained from 4 camera positions within the L-shape reactor. The flow entered through a straight concentric inlet tube from the right and passed to the left. The tube with an $\frac{L_1}{D_1}$=45 allowed the flow to fully develop. The axisymmetric jet entering was subjected to an expansion ratio of $\frac{D_2}{D_1}$=4.6. The emerging flow structures along the reactor axis could be categorized into three distinct zones of jet expansion, recirculation, and redevelopment zones. The geometry with a sudden expansion created a central expanding jet (jet expansion zone). Between the jet and the slower fluid, shear layers with high velocity gradients formed and the expanding jet also introduced adverse pressure gradients. In this area between jet and outer reactor walls, a zone with recirculating fluid flow is formed (recirculation zone). The shear layer,

separating the expanding jet from the recirculation zone, grew by entraining the surrounding slow moving fluid and finally merged with the outer boundaries (walls) at the reattachment point. The reattachment point is defined as the point where the shear layer touches the wall, splitting into fluid returning to the recirculation area and fluid joining the bulk liquid flow. After interacting with the lamp holder the flow finally evened out in the "redevelopment zone".

The contours of velocity magnitude (Figure 2.4) show the local velocity magnitudes formed by the sum of square roots of the mean velocity in both z-(U) and r-(V) directions, parallel and perpendicular to the reactor axis ($\sqrt{U^2+V^2}$) for three flow rates. The white areas indicate velocities of more than 0.15 m/s in any direction and areas of low velocities appear darker or black. The shear layer is a distinct and nearly stationary region visible between the two opposing flows.

At 2.5 cm (1 inch), the round jet impinges on the semi-spherical lamp tip with little visible dispersion. The separating flow stays attached to the lamp surface until the lamp holder lifts the flow from the lamp and increases the angle of the shear layer, resulting in a reattachment for the reactor top at 20 cm (8.8 inch), corresponding to $2.5\times D_2$ in length from the inlet. In Figure 2.4, the reattachment point is shown by the (dark) shear layer meeting the walls. Roughly extrapolating the shear layer for a reattachment point without the holder, the point corresponds to more than $3\times D_2$ from the inlet. Even taking into account that a linear extrapolation might not be true, the lamp seems to reduce the angle of the shear layer growth rather than spreading the inlet jet.

Experimental results by various researchers, gathered by Forester and Evans (8), show that the reattachment point for similar geometries with no obstructions can be found around 2-$3\times D_2$ from the inlet. The lower than anticipated spreading of the jet could be explained by the coanda effect, the tendency of a flow to follow a (curved) surface. Devenport and Sutton (6) observed an opposite trend when placing a blunt center-body downstream of the sudden expansion; the curvature of the shear layer increased, resulting in an earlier reattachment point. This shows the potential importance of the shape of the lamp tip on the flow field.

In the recirculation zone, returning flows are visible along the top and lower walls with recirculation starting close to the reattachment points (Figure 2.3b). At a volumetric inflow of 11 GPM the counterstream flows reach maximal negative

velocities of -0.26 m/s corresponding to 0.11 $\times V_{inlet}$. Although there have been no systematic experimental investigations into the effect of expansion geometries on the maximum back flow velocity, Forester and Evans (8) report values of 0.096 V_{inlet} for a similar geometry without a central annulus. The recirculating flow feeds into the expanding shear layer and loses velocity, resulting in a concentric zone of low velocity along the reactor walls close to the entrance. The flow in the inlet region matches the characteristics of a standard expanding jet without obstacles in many respects. The central lamp seems to have little effect on the expanding jet in the inlet region and recirculation zone.

In the region of the lamp holder, the flow patterns deviated from a standard expanding jet. The axial velocity profile up to this point remained symmetric, as can be seen in Figure 2.5a-b. The ridge between lamp-holder and lamp clearly disturbed the flow attached to the lamp's face and deflected the main flow away from the center (Figure 2.5c). For the top part of the reactor, the shear layer showed the deflection toward the walls as discussed. For the lower part, this was not as evident, with the lower spoke of the lamp holder centered directly in the measurement plane. The flow separated around the cylindrical spoke and a closer analysis of the instantaneous velocity maps indicated that a periodic vortex shedding typical for blunt body flows occurred. The low measurement frequency of 0.1 Hz did not allow a resolution of the shedding phenomenon. In the time-averaged statistical solution, the alternating velocities perpendicular to the measurement plane cancel each other out, resulting in an area of low axial velocity. This time dependent behavior remained local and confined. The axial velocity profile in Figure 2.3b shows the slower and less stable flow in the zone right after the lower holder spoke and the faster flow between the top spokes. This pattern is thought to be repeated three times over the circular cross-section, with the extremes (in plane with spoke and between the spokes) visible here. In the redevelopment zone after the reattachment point, the flow evens out and assumes turbulent plug flow characteristics over the remaining length beyond 20 cm.

Predictable and stable flow patterns are important to ensure compliance with minimal reactor performance levels over a range of volumetric flow rates. This scalability is especially vital for mandated limits like the UV-disinfection rates for drinking water. To study the effect of flow rate on the reactor hydrodynamics,

flow rates of Q=6.94×10^{-4} m^3/s (11 GPM), Q=5.05×10^{-4} m^3/s (8 GPM) and Q=2.52×10^{-4} m^3/s(4 GPM) respectively, corresponding to Reynolds numbers of Re=10200, 7500 and 3700 in the main body of the reactor, were examined. Figure 2.5 shows axial velocity profiles at three positions downstream of the reactor inlet. The axial velocity profile obtained at 1.3 cm (0.5 inch) from the reactor inlet, was in good qualitative agreement with an expanding jet flow (18). At 10 cm (4 inch), the velocity of the recirculating flow for the lowest inlet speed drops disproportionally. The contours of velocity magnitude show that the centers of recirculation have moved while the central jet remains stable. At 23 cm (9 inch) the profiles show a similar behavior; the reduced flow speed changed the angle of the shear layer above the lamp holder resulting in a broader axial profile. The flow below the lamp shows changes in both the axial profile and the contours of velocity magnitude. This might be caused by the change in flow speed influencing the frequency of the vortex shedding after the spoke.

Figure 2.4 shows the contours of velocity magnitude for the three inlet rates. The observations made above hold true and show that within the tested flow regimes the flow structures remained stable, confirming that, over a broad range of inlet velocities, changes of internal flow distribution occur, but the flow structures scale predictably with the flow rates. The figures give a good qualitative comparison of the overall similarity for the different flow speeds, indicating that flow patterns stay predictable within the tested volumetric range.

To test the influence of changes in the internal reactor geometry on the flow behavior, two additional measurements were performed (Figure 2.6). First, the lamp and lamp holder were moved 2.54 cm (1 inch) away from the inlet, keeping the position of the lamp holder fixed relative to the lamp. This is a change possible with the little effort for any L-shape design, thus representing a likely modification. The contours of velocity magnitude in Figure 2.6b show an elongation of the inlet jet and a less pronounced change of radial expansion just after impinging on the moved lamp tip. The remaining flow structures were shifted by 2.54 cm as expected and retained their shape. Without the lamp holder breaking the jet away from the lamp, it could extend much further into the reactor domain. An extended shear layer would introduce more turbulent kinetic energy and thus mixing over the length of the reactor. On the other hand, a segregated flow with high velocities

and thus short residence times at the core might receive lower UV-dose, even though it remains in the volume of high fluence rates.

In a second change of the internal geometry, the lamp holder was moved to 7.62 cm (3 inches) from the reactor inlet while the lamp tip remained at 2.54 cm (1 inch). The higher velocities close to the inlet reduced the lamp holder's influence on the flow (Figure 2.6c). The deflection of the shear layer toward the outer walls was not as pronounced and the resulting shallower reattachment angle led to a less well defined reattachment point. Both reattachment and recirculation points moved less than 1 cm closer to the inlet while reflux zones pronouncedly changed their appearance. This change of reactor geometry had a much deeper impact on the resulting flow structures and removed the axisymmetry in the inlet region. The inlet jet retained much of its former shape despite the new obstacle. The recirculation point in the lower reactor part remained almost unmoved, now situated behind the lamp holder.

The axial velocity profiles at 38 cm (15 inch) or later were similar in all cases, thus indicating that any disturbances from the inlet region have abated at one-third of the distance along the reactor. No changes in the flow emerged, until the outlet dictated flow structures became predominant close to the reactor outflow. Figure 2.7 shows the PIV data for the final reactor section. The vectors of velocity magnitude for both the L- and U-shapes agree well and indicated that any hydrodynamic influence from further upstream has abated.

The results indicate that the shape and position of the lamp and the lamp holder can impact the flow distribution within the L- and U-shaped reactors. If enhanced mixing is desirable, changing the position of geometry of the lamp tip and the lamp holder offer the best starting points for improving flow mixing.

2.3.2 U-shape reactor

The second reactor examined was the U-shape, with all dimensions remaining fixed except for the inlet position and removal of the lamp holder since it is not needed in this design. The change of the inlet position resulted in a distinctly different flow distribution. The inlet in U-shape reactors is known to strongly influence reactor hydrodynamics, off-center inlets have been used to induce swirling flows

throughout the domain (16). For UV applications on the other hand, a uniformly turbulent, well-mixed flow is sought. Swirling might lead to stable flow structures remaining far from the energy source and thus receiving lower UV-dose.

From the top inlet, a round expanding jet entered the reactor, through a straight tube with an $\frac{L}{D}$=45 allowing for a fully-developed flow. The inlet position was situated on the curved reactor surface, 3.8 cm (1.5 inch) from the inlet wall and 85.1 cm (33.5 inches) from the outlet, resulting in asymmetric boundaries of the jet expansion volume. The expanding jet impinged on the concentric lamp surface and separated around it (Figure 2.8). The flow remained attached to the round lamp surface, until the streams recombined below and detached. Figure 2.8 shows the plane perpendicular to the main reactor body, centered below the inlet at 3.8 cm (1.5 inches). The view of the flow close to the lamp was blocked by the hexagonal nut holding the lamp, but the flow detaching from the lamp is clearly visible. The velocity vectors averaged from 800 PIV measurements taken over a period of 2 h resulted in a symmetric inlet flow (Figure 2.8b). The average vector of the detaching flow was centered but proved to be unstable and influenced by several factors. Symmetrical results were only obtained after averaging PIV measurements taken over more than one hour. The vectors of velocity magnitude from subsets of 100 PIV measurements (16 minutes) show the two main stable states of the time dependent flow (Figure 2.8c-d). Repeated measurements confirmed the flapping flow phenomenon occurred at a lower frequency than can be explained by vortex shedding.

A point P1 (Figure 2.8b) was defined in the recirculation area to determine a possible pattern in the flapping flow. A plot of the V (vertical) velocity at P1 over 800 instantaneous measurements (Figure 2.9) shows that velocity changes of more than 1.5 m/s occurred. The moving average over 10 instantaneous points, revealed two plateau velocities where the flow remains stable correlating with the (right/left) states in Figure 2.8c-d. No indication of a repeating pattern was found in the reversal of flow directions as the flow velocity remained stable from 1 up to 18 minutes.

The results indicate that the instability originated at the jet impinging point on the lamp. The geometry imposes an unstable equilibrium and the flow seeks a lower potential. With a fully symmetric geometry only a small perturbation

is needed to favor one side of the lamp over the other. Once the flow follows a wall, it will remain attached, according to the coanda effect. The flow leaving the lamp with a directional bias finally impinges on the reactor walls and follows the curvature back to the inlet. The biased returning flow thus reinforced the bias by exerting pressure on the inlet jet and stabilized the flow structure. However, the symmetrical reactor geometry limits this effect and the energy required to flip the flow remains low. Vortex shedding after the lamp and turbulent flow vortices in the inlet jet and wall flows occasionally overlap and exert enough force to flip the flow from one side to the other. There might be further effects exerting an influence on the fluctuating flow, such as a pulsing inlet flow (from pump irregularities), the movement of boundary conditions, and in particular the movements of the lamp.

If the flow remains stable on one side for an extended period of time, a swirling motion could build up along the reactor length. Measurements where the inlet was deliberately offset by 2 mm horizontally, showed that the flow did indeed stabilize and remain on one side of the lamp, leading to a clockwise swirling motion for an offset to the right (similar to the image in Figure 2.8b). While flow reversals still occurred for single measurements, there were no longer two stable states discernible. This supports the notion that the flapping flow is a result of flow instability where the inlet flow impinged on the central lamp surface.

Time-averaged results could still be made by extending the acquisition period to compensate for the time dependence at the inlet. Figure 2.10 shows the composite time-averaged results from PIV measurements at 4 camera positions along the central plane. The qualitative analysis of these measurements shows that a majority of the flow followed the lower wall in the main reactor direction. This might lead to lowered reactor performance due to a high flow velocity (short residence time) far from the radiation source.

Further investigation revealed that the flow field in this part of the reactor is highly three dimensional. The inlet jet impinging on the lower reactor wall followed its curvature upwards as seen in Figure 2.8 but also follows the main flow direction along the reactor. Finally, these two diagonal wall flows meet at the top of the reactor center-plane at about 20 cm, but the flapping inlet flow does not allow this structure to fully stabilize. Yet, while not capturing all aspects of the reactor hydrodynamics, the center plane gives the most accurate 2D representation of the

overall flow field.

The expanding jet at the inlet creates a low pressure gradient leading to two recirculation regions in the top half of the reactor: a small zone behind the inlet with a clearly defined recirculation point and a broader, less defined zone toward the outlet with a center roughly 14 cm from the inlet. The contours of velocity magnitude (Figure 2.11) show the recirculation zone as a dark area with little stream-wise velocity close to the top wall. At regions about 25 cm downstream of the inlet, the streams that followed the outer walls recombine and continue stream-wise; they are visible on the center plane as a confined zone of sudden high velocity (white) close to the top. The fast flow along the lower wall extended to roughly the same region at about 25 cm, where it detached and dissipated into the main stream. Over the next 15 cm the flow distributed evenly and after about $5 \times D_2$ length, the flow in the U-shape reactor assumed an axial profile equivalent to a turbulent plug flow (Figure 2.10).

The flow field at the outlet of the U-shape reactor is equivalent to that of the L-shape reactor (Figure 2.7) and is driven by the velocity gradient of the out-flow contraction. The S-shape reactor is expected to exhibit a similar flow field to that of the U-shape throughout most of the reactor volume, with an outlet flow field in the opposite direction.

2.4 Conclusion

The flow fields in two typical cylindrical annular UV-reactor configurations were examined and the dependency of the hydrodynamics on the inlet position was demonstrated. Using PIV, the instantaneous and time-averaged flow properties were studied for a number of flow conditions and over a range of changes in geometry.

As a measurement technique, PIV was effective in capturing large areas of velocity field information. The vectors of velocity arranged as axial profiles gave a good qualitative impression of the overall flow field in these reactors. Examination of the time-averaged velocity field revealed characteristic time-averaged flow structures for both reactor configurations.

For the L-shape reactor, the flow patterns remain stable and thus predictable

over a range of flow rates and minor changes in internal geometry. The inlet region exhibits a typical expanding jet behavior including flow recirculation and zones of slow flow close to the inlet. The rate of expansion of the inlet jet was influenced (reduced) by the central annulus and the coanda effect was proposed as an explanation for this behavior. Time dependent flow structures (vortex shedding) were observed around the lamp holder and it was shown that these remain localized.

For the U-shape reactor, the flow structures were found to be less stable. A time dependent flapping flow perpendicular to the main reactor axis was observed with no discernible pattern.

The results indicated that simple changes in reactor geometry, such as rearranging the inlet position can significantly impact the local flow field and therefore the expected UV-dose distribution and the reactor performance. The L-shape reactor showed high velocity fields closer to the radiation source while the U-shape reactor demonstrated higher velocities along the outer reactor walls far from the central lamp. Therefore, the L-shape is expected to provide a more uniform dose distribution and a better reactor performance. The detailed qualitative and quantitative information on reactor hydrodynamics presented, could be used for the validation of CFD flow predictions in annular reactors.

2.5 Tables and figures

Table 2.1: PIV system specifications

Laser Source	pulsed Nd:YAG
Wavelength	532 [nm]
Laser Power	$\sim$ 50 [mJ]
Pulse length	10 [ns]
Pulse interval	800 [μs]
CCD Camera	1023×1343 pixel
Interrogation Area	32×32, 16×16 pixel
Correlation	Adaptive Cross-Correlation
Overlap	50%
Particles	PSP, 20 μm
Particle density	1.03 [g/cm^3]

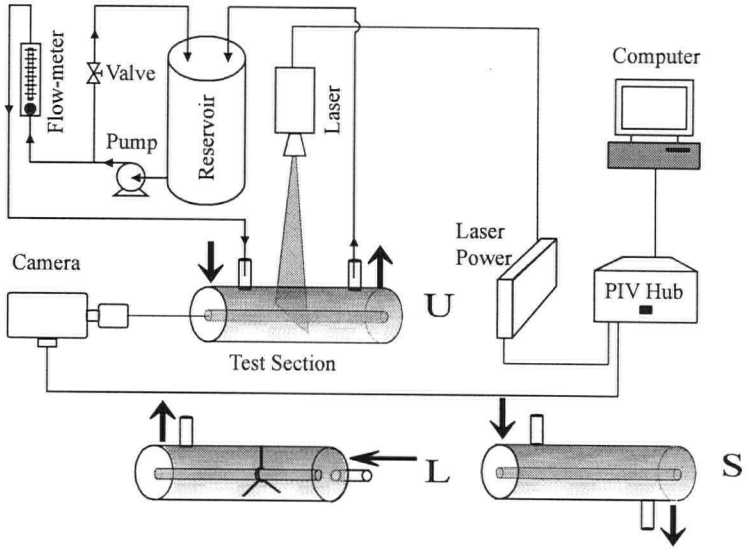

Figure 2.1: Schematic of the experimental setup: Fluid loop and PIV acquisition setup. The U-, L- and S- shape reactor configurations are show.

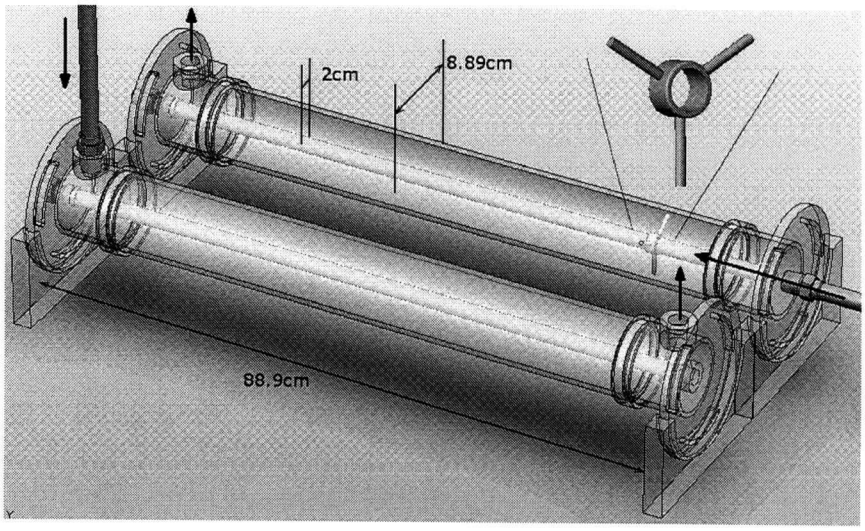

Figure 2.2: Geometry of the U- and L-shape reactors. The lamp holder in the L-shape is enlarged.

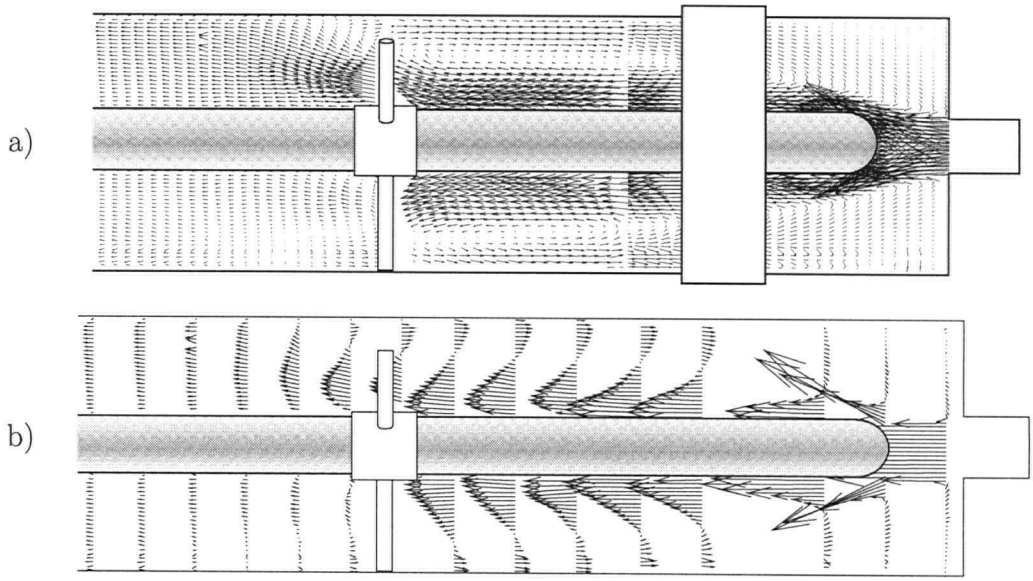

Figure 2.3: a) Vectors of velocity magnitude from PIV measurements at the vertical centre-plane the L-shape reactor 11 GPM. Areas not accessible by PIV are whited out (including the concentric lamp with a semi-spherical tip, a strip of 2.54 cm (1 inch) width, and the lamp holder visible at 18.7 cm (7 inches)). The length of the arrows shows the relative velocity magnitude. b) Vectors of velocity magnitude arranged to show the flow profile developing along the reactor axis.

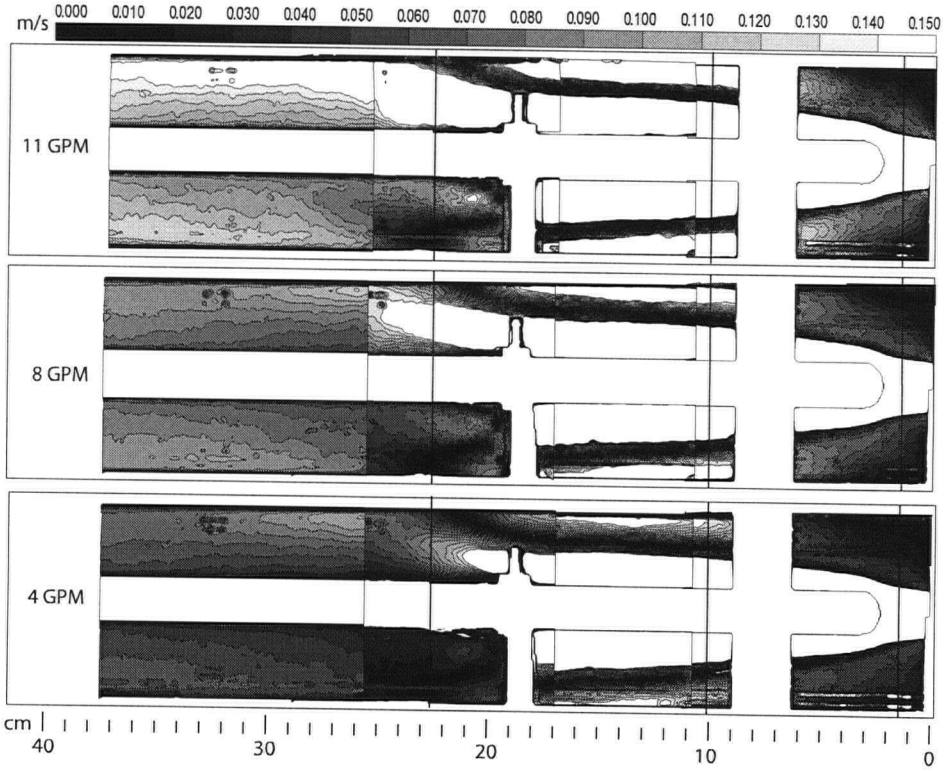

Figure 2.4: Contours of velocity magnitudes along the center-plane of the L-shape rector, for volumetric inlet flows of 11, 8 and 4 GPM. Each map is a composite of 4 partially overlapping measurement windows. The overlapping areas show very good agreement and support the assumption of negligible image distortion along the reactor axis. The white areas (except the lamp, lamp holder and cap attachment, where no measurements were performed, see Figure 2.3) indicate axial velocities of more than 0.15 m/s.

a)

b)

c)

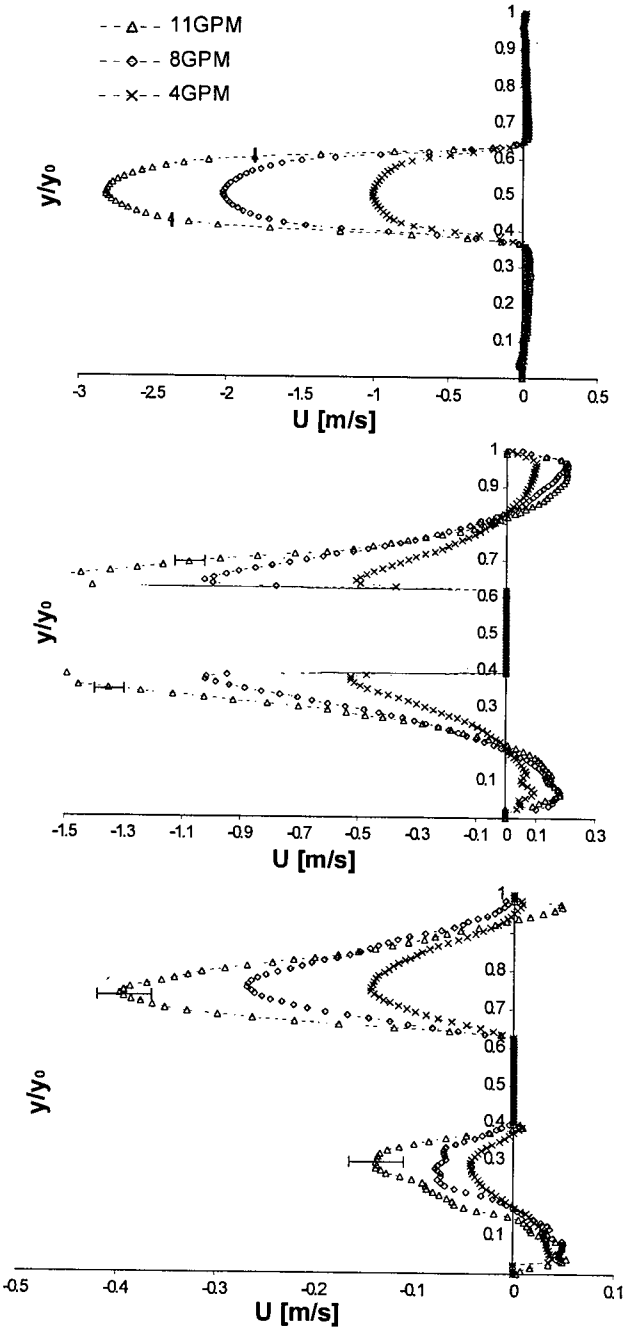

Figure 2.5: Contours of axial velocity (U) for three inlet speeds of 2.5 m^3/h (11 GPM), 1.82 m^3/h (8 GPM), and 0.91 m^3/h (4 GPM) at 1.3 cm (a), 10 cm (b) and 23 cm (c) from the reactor inlet. See Figure 2.4 for the position of the lines. The error bars represent the 95% confidence interval.

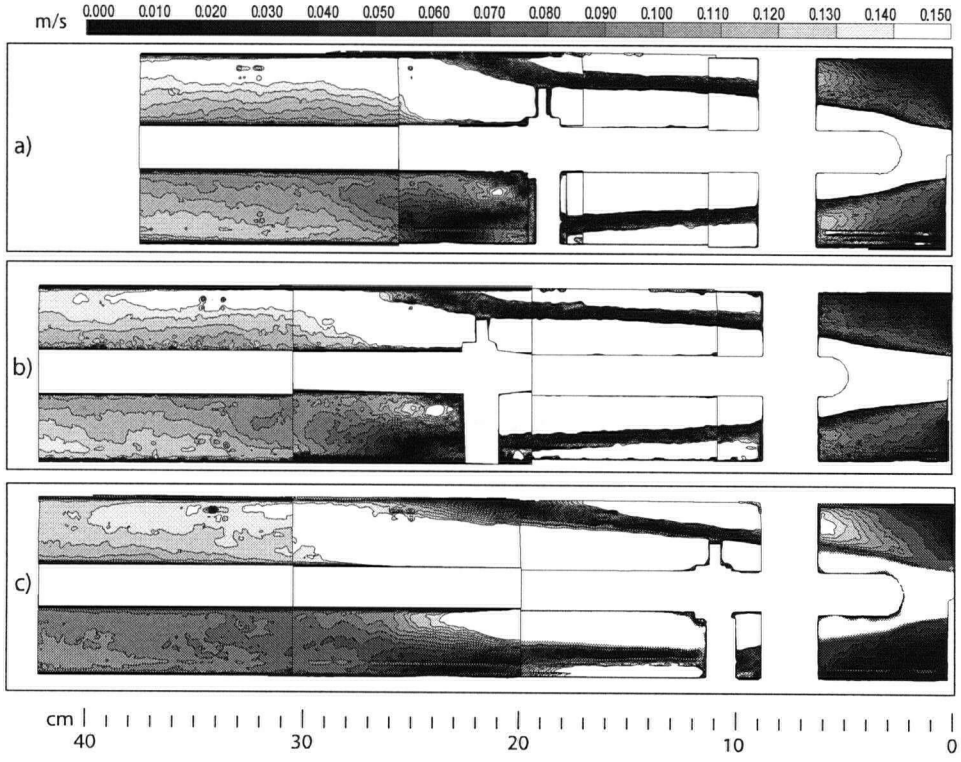

Figure 2.6: Contours of velocity magnitude at the vertical centre-plane fo the L-shape reactor. a) The standard configuration, lamp at 2.5 cm (1 inch) and lamp holder at 18.5 cm (7.3 inches) from the inlet, b) The lamp tip moved 5.08 cm (2 inches) from the inlet, c) The lamp holder moved from 18.5 cm (7.3 inches) to 7.6 cm (3 inches)

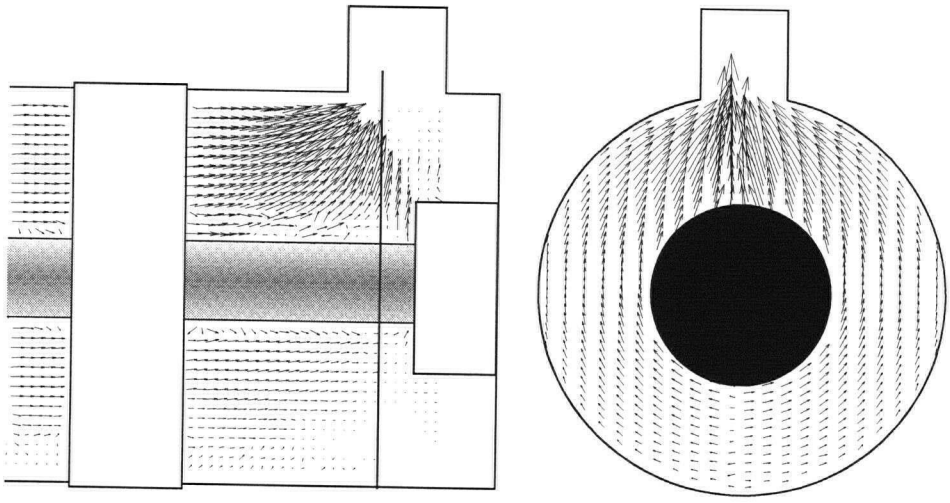

Figure 2.7: Vectors of velocity magnitude, in the outlet region of the L- and U-shape reactors. The length of the arrows shows the relative velocity magnitude. The outlet cross-section position is indicated at z=86 cm. Both L- and U-shape reactors showed nearly identical flow behavior at the outlet.

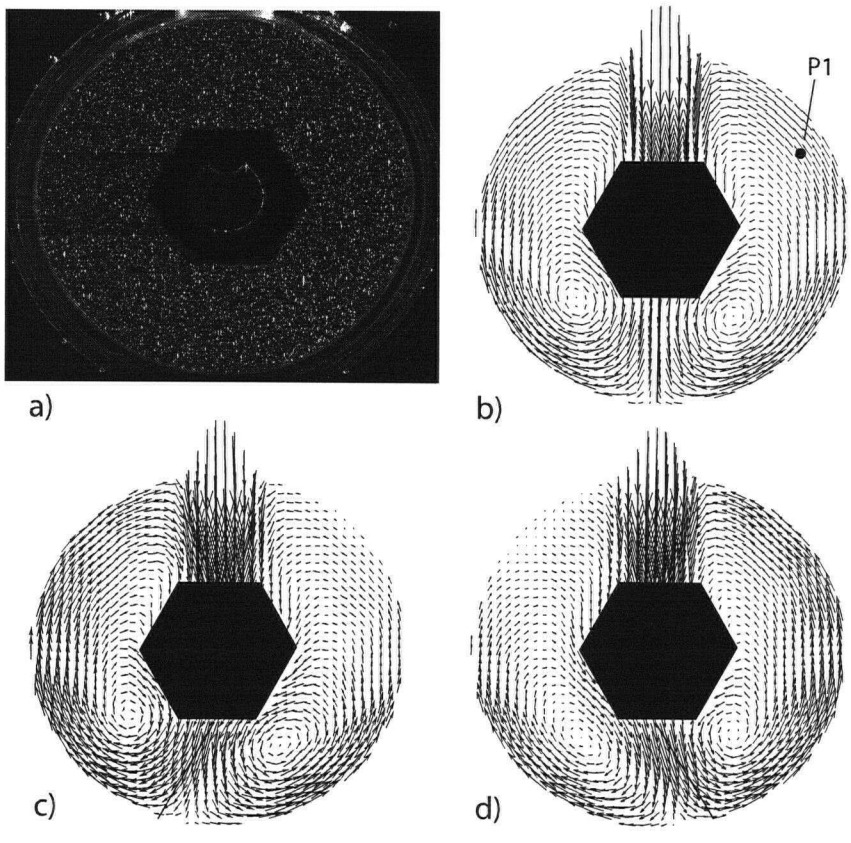

Figure 2.8: U-Shape reactor, cross-section inlet plane centered on the inlet. a) The unprocessed PIV image shows the shadow of the lamp sleeve illuminated from the right side, the nut holding the lamp (blacked out) and the illuminated 20 μm particles. b) Time-average vectors of velocity from 800 measurements. c) Average of the first 100 measurements. d) Average of the second 100 measurements.

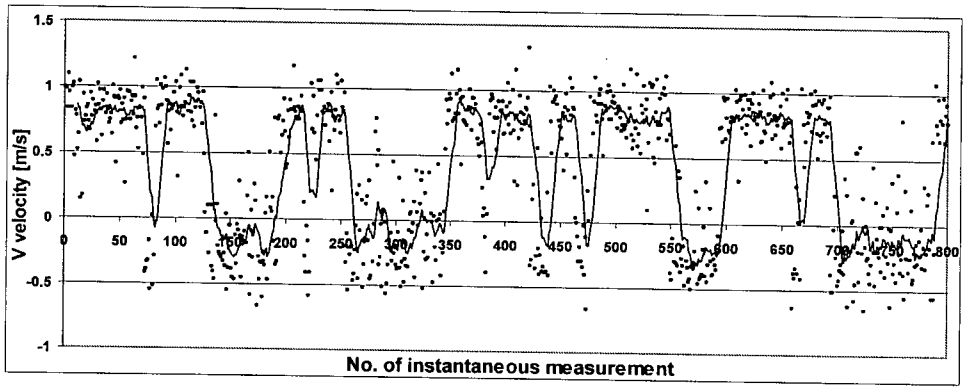

Figure 2.9: Instantaneous (time dependent) vertical (V) velocity measurements in point P1 from Figure 2.8b). The moving average over 10 points (solid line) shows the frequency of change from side to side, in the flapping flow.

a)

b)

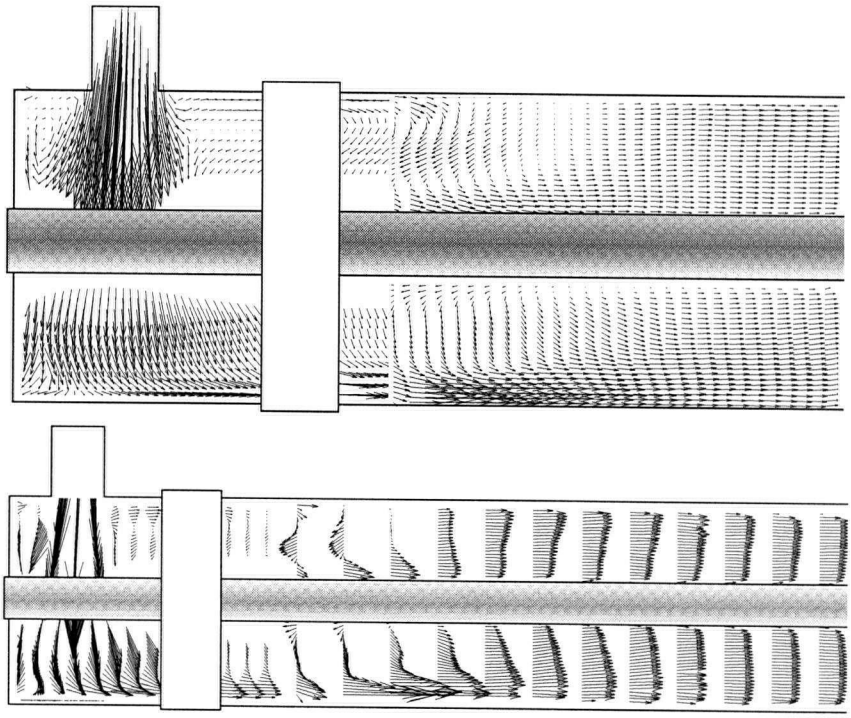

Figure 2.10: a)Vectors of velocity magnitude at the vertical center-plane of the U-shape reactor. Flow entering from the top left at a rate of 2.5 m^3/h (11 GPM) (lamp fitting (left) blocked laser access to areas close to the lamp in the near inlet region). b) Vectors of velocity magnitude arranged to show the flow profile developing along the reactor axis.

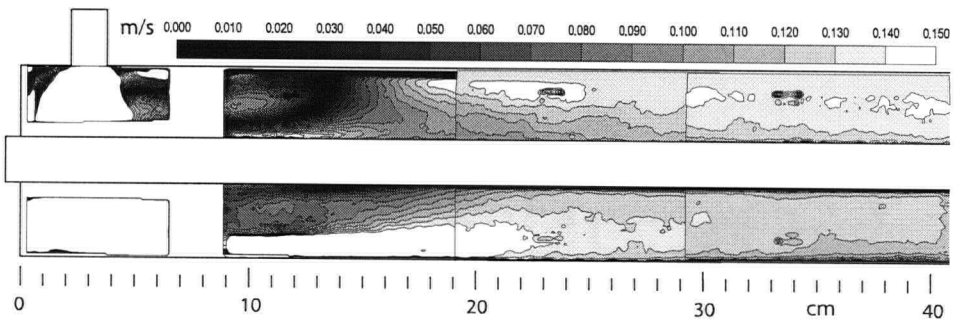

Figure 2.11: Contours of velocity magnitude at the vertical center-plane of the U-shape reactor. The white contours indicate velocities of more than 0.15 m/s. Blank areas were not accessible to either the PIV laser sheet (shadowing) or the camera.

Bibliography

[1] ADRIAN, R. J. Twenty years of particle image velocimetry. In *12th International Symposium on Aplications of Laser Techniques to Fluid Mechanics, Lisbon* (July 2004).

[2] BRAUN, A., JAKOB, L., AND OLIVEROS, E. Advanced oxidation processes - concepts of reactor design. *Journal of Water Supply: Research and Technology-AQUA 42*, 3 (1993), 166–173.

[3] CASSANO, A. E., MARTIN, C. A., BRANDI, R. J., AND ALFANO, O. M. Photoreactor analysis and design: Fundamentals and applications. *Industrial & Engineering Chemistry Research 34* (1995), 2155–201.

[4] CHANG, P. B. L., AND YOUNG, T. M. Kinetics of methyl tert-butyl ether degradation and by-product formation during uv/hydrogen peroxide water treatment. In *Proceedings of the Air & Waste Management Association's Annual Conference & Exhibition, 93rd, Salt Lake City, UT, United States, June 18-22, 2000* (2000), pp. 7036–7055.

[5] CHIU, K., LYN, D. A., AND BLATCHLEY, E. R. Integrated uv disinfection model based on particle tracking. *Journal of Environmental Engineering* (1999), 7–16.

[6] DEVENPORT, W. J., AND SUTTON, E. P. An experimental study of two flows through an axisymmetric sudden expansion. *Experiments in Fluids 14*, 6 (1993), 423–432.

[7] ELKANZI, E. M., AND KHENG, G. B. H_2o_2/uv degradation kinetics of isoprene in aqueous solution. *Journal of Hazardous Materials 73* (2000), 55–62.

[8] FORESTER, S. E., AND EVANS, G. M. Computational modelling study of the hydrodynamics in a sudden expansion - tapered contraction reactor geometry. *Chemical Engineering Science 52*, 21 (1997), 3773–3785.

[9] ISLAM, M. S., HAGA, K., KAMINAGA, M., HINO, R., AND MONDE, M. Experimental analysis of turbulent flow structure in a fully developed rib

roughened rectangular channel with piv. *Experiments in Fluids 33* (2002), 296–306.

[10] JANEX, M. L., SAVOYE, P., DO-QUANG, Z., BLATCHLEY, E., I., AND LAINE, J. M. Impact of water quality and reactor hydrodynamics on wastewater disinfection by uv, use of cfd modeling for performance optimization. *Water Science and Technology 38* (1998), 71–78.

[11] KAMIMURA, M., FURUKAWA, S., AND HIROTSUJI, J. Development of a simulator for ozone/uv reactor based on cfd analysis. *Water science and technology : a journal of the International Association on Water Pollution Research 46* (2002), 13–19.

[12] LABAS, M. D., ZALAZAR, C. S., BRANDI, R. J., MARTIN, C. A., AND CASSANO, A. E. Scaling up of a photoreactor for formic acid degradation employing hydrogen peroxide and uv radiation. *Helvetica Chimica Acta 85* (2002), 82–95.

[13] LAWRYSHYN, Y. A., AND CAIRNS, B. Uv disinfection of water: the need for uv reactor validation. *Water Science & Technology: Water Supply 3* (2003), 293–300.

[14] LYN, D. A., CHIU, K., AND BLATCHLEY, E. R., I. Numerical modeling of flow and disinfection in uv disinfection channels. *Journal of Environmental Engineering (Reston, Virginia) 125* (1999), 17–26.

[15] OPPENLAENDER, T. *Photochemical purification of water and air.* Wiley-VCH, 2003.

[16] PRUVOST, J., LEGRAND, J., LEGENTILHOMME, P., AND DOUBLIEZ, L. Particle image velocimetry investigation of the flow-field of a 3d turbulent annular swirling decaying flow induced by means of a tangential inlet. *Experiments in Fluids 29* (2000), 291–301.

[17] SCHOENEN, D., KOLCH, A., AND GEBEL, J. Influence of geometrical parameters in different irradiation vessels on uv disinfection rate. *International Journal of Hygiene and Environmental Medicine 194*, 3 (1993), 313–320.

[18] WEISGRABER, T. H., AND LIEPMAN, D. Turbulent structure during transition to self-similiarity in a round jet. *Experiments in Fluids 24* (1998), 210–224.

[19] WU, H. L., PENG, X. F., AND CHEN, T. K. Influence of sleeve tube on the flow and heat transfer behavior at a t-junction. *International Journal of Heat and Mass Transfer 46* (2003), 2637–2644.

Chapter 3

CFD study of annular UV-reactor hydrodynamics

The following chapter covers the computational fluid dynamics (CFD) models created to study the hydrodynamic flow in annular reactors. The influence of mesh density and choice of turbulence models is discussed. Finally, the CFD modeling results are compared to PIV experimental data and conclusions on the validity of the models are made.

3.1 Introduction

Water treatment processes using UV-technology have seen a rapid growth over the last decade (12). The increasing public awareness of water as a resource, and increasing regulations, have resulted in a compound annual growth rate of 11% (1996-2001) for the North American UV-market, and a slightly higher rate was estimated for the following years (16).

A successful fundamental simulation of UV-systems is the basis for several applications: virtual prototyping, cost effective design optimization, and on-line control and performance evaluation. UV reactor simulation can be achieved by considering the rate of reaction linked to the non-homogeneous UV-fluence rate through the local volumetric rate of energy absorption. This spatial dependency makes a three-dimensional resolution of the reaction rate indispensable (9). Only after computing the full hydrodynamic flow of the reactor does it become possible

to correctly model the reaction rate inside UV-reactors. The effect of the interaction between reactor hydrodynamics and local radiation intensity on the concentration distribution of contaminants in UV-advanced oxidation reactors (AdOx) was shown by Pareek et al. (11). Schoenen et al. (19) demonstrated the influence of the flow field and geometry on the performance of disinfection systems.

Realizing the importance of an integrated model, Romero et al. (18) set up the fundamental balances needed to solve the mass, momentum, energy, radiation and chemical reaction rate equations for annular UV-reactors. Because of a lack of computing power, they assumed axial symmetry and implemented a simplified set of equations for two-dimensional geometries, a method that was then applied for subsequent studies of different geometries and reaction kinetics by Cassano et al. (2). With the increased performance of computational resources and the development of simulation software, computational fluid dynamics (CFD) is becoming an affordable engineering tool to simulate and optimize reactor designs. The viability of CFD for the design and optimization of chemical reactors has been demonstrated for a variety of systems (1, 11, 20). CFD has been applied to the simulation of UV-reactors hydrodynamics (21). It has also been utilized to simulate UV-reactor performance through the integration of reactor hydrodynamics, radiation distribution and UV-reaction kinetics (9).

While CFD is becoming a mainstream modeling tool, anticipating the flow characteristics and selecting the appropriate modeling technologies (boundary conditions, turbulence model, etc.) remain the responsibility of the user. As CFD is based on the governing equations of mass and momentum conservation as well as mathematical models with simplifying assumptions, there are many possible sources for errors, and validation of the CFD results is vital for the effective use of such a model. Advanced experimental methods such as laser Doppler velocimetry (LDV) and particle image velocimetry (PIV) have been shown to give detailed information on the turbulent flow field in stirred vessels (10, 15) and in tubular channels (4, 6, 13).

CFD solves the governing equations of the flow mass and momentum conservation in the discretized computational domain using a numerical (e.g. finite volume) method. Different approaches can be taken for modeling turbulent flows. In the Reynolds averaged Navier-Stokes (RANS) approach, instantaneous velocity com-

ponents are usually divided into their mean and fluctuating values ($u = \overline{u} + u'$). The mass and momentum conservation in suffix notation are:

$$\frac{\partial \overline{u_i}}{\partial x_i} = 0 \tag{3.1}$$

$$\frac{\partial \overline{u_i}}{\partial t} + u_j \frac{\partial \overline{u_i}}{\partial x_j} = -\frac{1}{\rho}\frac{\partial p}{\partial x_i} + \frac{\partial}{\partial x_j}(\mu \frac{\partial \overline{u_i}}{\partial x_j} - \overline{u_i' u_j'}) \qquad i,j = 1,2,3(for\ x,y,z) \tag{3.2}$$

where u_i is the instantaneous velocity, $\overline{u_i}$ the mean velocity, and u_i' the fluctuating velocity component in the i^{th} direction. The unknown terms $-\rho\overline{u_i' u_j'}$, called the Reynolds stresses, represent the effect of small scale turbulence on the mean flow and need to be closed by using one of the turbulence models.

Among the factors that may influence the CFD results are the discretisation of the domain (structure and size of the cells), and the type of modeling approach employed (turbulence model, etc). Grid generation is often quoted as the most important and most time consuming part of CFD analysis. The quality of the grid has a direct influence on the quality of the analysis, regardless of the flow solver used. Additionally, the solver will be more robust and efficient when using a well constructed mesh. A quality grid, capable of representing the geometry, is the basis for a reliable, accurate simulation. In general, both mesh quality and grid independence of the solution need to be ensured (3).

When the flow is within the turbulent regime (typically the case in UV-reactors), additional models are required to consider the effect of turbulent fluctuations on the flow. For most engineering applications, only the mean effect of turbulent quantities is important; therefore, the time-averaged flow properties are of interest. The RANS equations are the established averaging approach for modeling turbulence. Two classes of RANS turbulence models are the κ-ϵ models and the Reynolds stress model (RSM), each relying on a set of implied assumptions with relative advantages and disadvantages. The κ-ϵ models use the Boussinesq hypothesis to relate the Reynolds stresses to the mean velocity gradient through the turbulent kinetic energy κ and the turbulent dissipation rate ϵ. This implies locally isotropic turbulent fluctuations and a local equilibrium of the production and dissipation terms. Primary shear stresses are predicted well with these two-equation models, but secondary shear stresses and normal stresses are not.

The Standard κ-ϵ model is the simplest of the two-equation models. It is robust, economic, and predicts a wide range of flows reasonably well. But the assumptions are only valid in fully turbulent flows; it cannot deal well with complex three-dimensional flows, sudden changes in the mean strain rate, curved surfaces, secondary motions and flow separation. It tends to over-predict turbulence generation in areas where the mean flow is highly accelerated or decelerated (8).

The Realizable κ-ϵ model incorporates time scale realizability and an additional source term in the epsilon equation for improved performance in flows involving adverse pressure gradients (including separated flows). It also features a realizability constraint on the predicted stress tensor. This avoids excessive levels of turbulence generation in regions of large mean strain, such as occur in impinging flows.

The RSM model uses the exact transport equations for Reynolds stresses, closing the unknown correlations at this level (second-order closure model). It abandons the isotropic eddy-viscosity hypothesis and performs well for many complex flows (e.g. highly swirling flows). The seven additional partial differential equations (PDEs) and a tendency to require a finer mesh make it computationally more expensive. Table 3.1 provides a brief summary of the advantages and disadvantages of the κ-ϵ and Reynolds stress models.

Despite a number of studies on CFD modeling of UV-reactor hydrodynamics, and the development of integrated CFD models for UV-reactor performance, to the author's knowledge there have been no efforts reported in the open literature to validate the CFD simulations with experimentally obtained flow field information. Also, little if any information can be found on the effect of computational domain discretisation and turbulence models on the CFD results. The objective of this work was to carry out a comprehensive CFD study of the turbulent flow occurring in annular UV-reactors and to compare the results with experimental measurements. The cylindrical UV-reactor with a concentric lamp parallel to the reactor body, which represents the basic design for many current UV-reactors, was investigated. The effect of grid number and structure on the CFD results in two commonly used UV-reactor geometries, with an inlet parallel (L-shape) and normal (U-shape) to the main reactor body, were studied. The influence of three different turbulence models was also assessed for both geometries. The results were

evaluated by comparison with experimental data obtained from Particle Image Velocimetry (PIV).

3.2 CFD modeling

The two model UV-reactor geometries studied, the L-shape and U-shape shown in Figure 3.1, are based on the existing industrial reactors as currently used. The simulation results were compared to the experimental PIV results from Plexiglas prototypes having the same dimensions. Both shapes shared the same main reaction tube diameter of 8.9 cm (3.5 inch), length of 88.9 cm (35 inch), with a central UV-lamp of 2 cm (0.79 inch) in diameter. The inlet and outlet ports, with a diameter of 1.91 cm (0.75 inch), were placed 2.54 cm (1 inch) from each respective end for the U-shape, while the L-shape inlet was centred on the front plate. The inlet tube length with an $\frac{L_1}{D_1} = 45$ was chosen to ensure that a fully developed flow was established at the entrance of the reactor. A volumetric inlet rate of 6.94×10^{-4} m^3/s (11 GPM), corresponding to a mean inlet velocity of 2.43 m/s, a mean axial velocity in the reactor of 0.11 m/s, and a Reynolds number of 10,000 was set.

The commercial mesh generator GAMBIT was used to create the grid and the tgrid tool was employed to merge separately meshed domains. The inlet and outlet tubes were meshed with 5,000-8,000 structured (Cooper) cells in all cases. Both structured and unstructured cells were employed to discretize the main reactor domain (Figure 3.2). For the unstructured tetrahedral mesh, no subdomains were needed. The size of cells was defined by cell-volume and refined manually if necessary. For the structured mesh, the domain was split into several subdomains reducing the use of unstructured cells to the volume containing the lamp holder in the L-shape reactor. For the U-shape, the inlet volume and lamp region with high velocity gradients, round jet impingement, and flow separation required a higher mesh resolution, while the lamp tip and the lamp holder needed more attention in the case of the L-shape.

A commercial CFD software package, Fluent (V6.1.22), was used to solve the conservation of mass and momentum equations for the described geometries. The internal structures were reproduced as 3D volumes and a no-slip boundary condition was imposed on the reactor walls. The operating fluid was defined as water

at 293 K. Velocity inlets, with a hydraulic diameter of 1.91 cm, 10% turbulent intensity, and a uniform velocity distribution were defined and a fully-developed flow (outflow) was applied at the exit. In all cases, the standard log law wall functions were employed. The segregated steady-state solver was used to iterate the solutions, starting with a first order upwind discretisation scheme, and continuing with the second order upwind scheme for the final converged solution. The SIMPLE method was chosen for the pressure-velocity coupling. Convergence of the numerical solution was ensured by monitoring the scaled residuals of continuity, x-,y-,z- velocities, and the turbulence parameters to a criterion of less than 10^{-5}. In addition, the velocity magnitude at two points defined in areas with high velocity gradients were used as indicators.

The importance of correctly resolving the turbulent flow behavior for chemical reactors has been stressed. The exact Navier-Stokes equations, are replaced by Reynolds averaged equations generating the need for closure models to obtain solutions. However, no turbulence model is universal and the choice is based on considerations of domain geometry and the anticipated flow behavior. Three turbulence models, the Standard κ-ϵ model, the Realizable κ-ϵ model, and the Reynolds Stress Model (RSM) were selected, based on availability (most widely used models) and usability (average time and computing power needed).

3.3 PIV experiments

The CFD flow simulations were validated using experimental PIV results. PIV is a non-intrusive method of instantaneous flow field visualization. A sheet of laser light flash-illuminates particles in the flow field and a digital camera captures the two points in time. The resulting flow velocity extracted from this digital image pair is an instantaneous snapshot of the flow in the area viewed.

The particle images were recorded using an 80C60 HiSense PIV camera connected to a FlowMap System Hub (Dantec Dynamics Inc.) for synchronization. A NewWave Solo-15 laser system provided illumination of the particles. The seeding (PSP, 20 μm diameter, 1.03 g/cm^3) was adjusted to $5 - 10$ particles per interrogation window. The image data were analyzed with a multi-pass adaptive cross-correlation technique with interrogation windows of 32×32 pixels and an overlap of

50% on the final pass. For each measurement, $250-500$ image pairs were used and the vector statistical average was calculated to obtain a time-averaged flow field. The PIV experiments were performed in exact full scale Plexiglas replications of the investigated reactors. A more detailed description can be found in Chapter 2.

3.4 Results and discussion

In annular U- and L-shape reactors (Figure 3.1), a typical structure is found to occur at the inlet where the round inlet jet impinges on the central annulus, from the front for the L-shape, or from the top for the U-shape reactor. The cylindrical annulus poses several challenges, such as flow separation, flow attachment/detachment, and also introduces an element of unsteadiness. The flow around bluff bodies is known to show a time dependent structure in the near wake, called vortex shedding. Since the flow is turbulent but statistically steady-state, the RANS turbulence modeling approach remains a viable approximation. However, the discretisation of this volume and the choice of RANS model may have a large influence on the final result. The effects of discretisation method and turbulence modeling on the CFD results are presented separately for the L-shape and U-shape reactors.

3.4.1 L-shape reactor

3.4.1.1 Influence of grid structure

The influence of the finite volume mesh on the CFD results was studied for both structured and unstructured grids. While an unstructured mesh is easier to generate initially and often the only solution for complex geometries, the unstructured tetrahedral elements are not considered ideal from an accuracy point of view. Control over the number and distribution of cells generated is restricted, resulting in higher cell densities compared to a structured grid. It is also well documented that structured meshes are less CPU intensive and tend to converge faster. Three test cases for the L-shape reactor are presented in Figure 3.2, an unstructured mesh with 0.3 million cells, and two structured meshes with 0.5 and 1.1 million cells. The central lamp with a rounded tip close to the entrance is held in place by a

lamp holder at 18.6 cm (7.3 inches). The three pronged lamp holder, required to center and retain the lamp at the entrance of L-shape reactors, was discretized with tetrahedral cells in all cases since no structured mesh was possible. The more precise control over the structured mesh is evident at the inlet and the lamp tip.

The simulated vectors of velocity magnitude of the flow produced in the reactor using the Realizable κ-ϵ turbulence model are presented on the center-plane of the reactor in Figure 3.3. The axisymmetric inlet jet entering the reactor from the right impinges on the lamp tip, separates and expands toward the outer walls. The expanding jet creates a pressure gradient leading to a region of flow recirculation along the reactor wall, and finally merges with the outer boundaries shortly after the lamp holder.

Even though the three plots show similar flow patterns, the disparity between the unstructured and structured meshes is easily visible and especially prominent when comparing the centers of recirculation. With a denser unstructured mesh, velocity profiles with a closer match to those obtained from both structured mesh and PIV experiments were achieved, but the results remained disparate within the memory dictated limits of a maximal 1.2 million cells. It can be concluded that a combination of unstructured mesh and lower mesh number were the reason for this difference. The two structured mesh plots show very good agreement and no difference between the low and high mesh is discernible, aside from the higher resolution.

Comparing the results to PIV data (Figure 3.4) shows that the CFD model yields flow patterns that are in good qualitative agreement for all mesh structures. However, some differences can be noted when comparing the structured and unstructured meshes. The centers of the primary recirculation loops are situated further along the reactor z-axis for the structured meshes, and the loops are elongated, which agrees well with the PIV data. In the area just behind the lower spoke of the lamp holder, the structured mesh solutions show a small recirculation loop that also shows up in the experimental data. There are no major flow structures that have not been captured by the modeled solutions.

Figure 3.5a-b compares the CFD results obtained using the three grid structures at positions 1 and 15 cm from the reactor entrance with the PIV experimental results. At these distances, the influence of turbulence is not significant and dif-

ferences are primarily mesh related. The maximum inlet velocity of 2.8 m/s and the overall velocity profiles are closely matched by all the CFD results. The unstructured mesh results, however, show a deviation from both the structured mesh results and the experimental data. The difference is especially notable at 15 cm and is a direct result of the shifted primary recirculation loop predictions. Both structured meshes show little deviation from each other and continue to match the experimental values closely. From these observations, it can be assumed that 0.5 million structured cells or more are sufficient for a mesh independent solution of UV-reactors with comparable dimensions, geometry, and flow rate.

3.4.1.2 Comparison of turbulence models

The effect of turbulence models was investigated using the structured mesh with 0.5 million cells for the Standard κ-ϵ, the Realizable κ-ϵ, and the Reynolds Stress models. The results of the Realizable κ-ϵ and the RSM models shown in Figure 3.6 are qualitatively comparable. However, differences can be noted in the area of the lamp holder. The RSM model over-predicts the turbulence in this region to such a degree that a region of unordered flow appears close to the upper reactor wall. This phenomenon is unphysical and is not observed in any other model or the experimental data. The discrepancy could be due to the higher sensitivity of the RSM model to abrupt changes in the grid structure.

A comparison of the z-velocity components (along the reactor axis) obtained using all three turbulence models with an experimental PIV data at 1, 15, 23, 38, 64 and 83 cm from the reactor inlet is shown in Figure 3.7a-d. At 1 cm, in the region of the free inlet jet, all turbulence models show an excellent match with each other and the experimental data. It can be noted that the Standard κ-ϵ shows some difficulty matching the outer regions of the free round inlet jet. At 15 cm, in Figure 3.7b, both the RSM and Realizable κ-ϵ models provide an excellent match of both flow contours and velocity, while the Standard κ-ϵ model under-predicts the returning flow velocity at the reactor walls indicating that the primary recirculation loops are not fully captured. At 23 cm, just after the lamp holder, both κ-ϵ models are in good agreement and give velocity profiles comparable to that of the PIV data. Both models over-predict the flow velocity along the lower reactor side and under-predict along the top. This discrepancy might be due to the introduction of

cylindrical bluff bodies (lamp holder spokes), and thus time dependent elements, into the flow. The κ-ϵ models are not well suited to deal with anisotropic flows, and have a tendency to over-predict viscosity, and thus equalize the flow distribution over too short a distance. The z-velocity components of the RSM model after the lamp holder are non-physical and show little resemblance to the experimental data. This is likely related to the sensitivity of this model to the unstructured mesh used in this region as discussed earlier. Finally, at 38 cm, the effects of the lamp holder are no longer prominent and all three models are in good quantitative agreement with the PIV results again. The RSM model matches the experimental flow profile closely in this region while the κ-ϵ models do not show the lower core velocity at the lamp surface. About three-quarters through the reactor, at 64 cm, the flow has assumed the typical plug flow structures that are well predicted by all turbulence models. Finally, at 83 cm (6 cm from the reactor end), the flow leaving through the top exit starts to show an influence and the velocity near the top surface increases, which is captured by all the turbulence models. It was found that the flow distribution in the last third of the L- and U-shape reactors show no significant difference.

A comparison of the contours of velocity magnitude obtained using the three turbulence models with PIV experimental values in Figure 3.8, shows that, in the reactor volume before the lamp holder, the predicted results of all the turbulence models agree with the PIV data and each other. At the lamp holder, the κ-ϵ models under-predict the deflection of the jet toward the reactor wall. While the RSM model captures this flow feature, the mentioned irregularities in the unstructured mesh are also apparent. The flow deflection also explains the observed higher velocity along the reactor walls at 23 cm (Figure 3.7).

The overall flow predictions are generally in good agreement with the experimental data throughout the reactor. The lamp holder introduces additional recirculation and mixing zones that were not accurately predicted by the κ-ϵ or the RSM models. Apart from the lamp holder region, the RSM model predicts the flow accurately; however, computational costs are approximately 60% higher and convergence is more problematic. Considering accuracy, computational costs, and sensitivity of the results to the grid structure, the Realizable κ-ϵ model seems to be a suitable turbulence model for the typical flows found in L-shape annular reactors.

3.4.2 U-shape reactor

In the U-shape reactor with the inlet on top, the lamp was fixed at the inlet and a cylinder attached to the end-cap was used to support the lamp at the outlet, removing the need for a lamp holder. With the exception of these structural changes, all other parameters remained fixed.

In the U-shape reactor, the flow is largely determined by the impinging jet on the central annulus in the inlet region and the following 90 degree change of flow direction. The bluff body (lamp) also introduces time dependent elements into the flow. Low and high cell densities were evaluated for both the structured and unstructured meshing approaches. The influence of the mesh density and structure on the central inlet plane velocity magnitudes, using the Realizable κ-ϵ turbulence model, are presented for unstructured and structured meshes in Figures 3.9 and 3.10, respectively. The main flow structures for both results are similar; a central expanding jet enters the reactor from the top, impinges on the central annulus, and separates around it. The flow follows the contours of the central annulus (coanda effect), recombines below the lamp, and detaches as a secondary jet. The impinging point on the lower reactor wall spreads the secondary jet and the flow following the reactor walls back up to the inlet, introduces two symmetric recirculation loops. The main challenge for this type of reactor is apparent in the non-symmetric solution for the low density, unstructured mesh (Figure 3.9b). The secondary jet detaching from the lamp at an angle, indicated a high mesh dependency of the solution. Unguided increase of the unstructured mesh's density did not automatically lead to better results. It was speculated that the non-symmetrical solution was due to numerical errors reinforced and amplified by the interaction of the recirculation loops with the inlet jet. This was corroborated by the modeling and convergence history of the models. First-order upwinding solutions converged nicely and showed the secondary jet detaching from the lamp centrally but in two separated streams, resulting in less pronounced recirculation loops. Second-order upwinding solutions showed pronounced recirculation loops and a combined single secondary jet, but detaching at an angle. Interestingly, rotating the virtual geometry by 90 degrees also resulted in different solutions, meaning that even the direction in which the numerical solver sweeped the iterated solutions through the domain influenced the final outcome. Enforced symmetrical

solutions through bisection of the reactor domain with a symmetry plane, lead to non-converging solutions, due to the highly three dimensional flow structure. A ten-fold increase of cell density in the inlet region, with special attention to the lamp surface, finally led to the anticipated results, but even with high mesh densities the detaching secondary jet was not perfectly centered.

The use of structured mesh in the inlet volume (Figure 3.10) led to a centered secondary jet, even for the lower mesh density. It was noted that the secondary jet still left the lamp in two streams. With the denser mesh, this no longer occurred, but as was the case for the unstructured mesh, a slight bias to the left remained.

The experimental data obtained from PIV in Figure 3.11 show symmetric recirculation loops with the secondary jet detaching centrally below the lamp. However, the PIV data were averaged over 2 h to reach this centered solution. The secondary jet flow initially showed a similar bias as noted for the simulation. It detached from the lamp at an angle and remained stable for short periods (in the order of 1-15 minutes) before swiftly changing to the other lamp side, resulting in a flapping motion. The secondary jet flow, detaching from the central annulus, remained roughly stable at angles of about 25 degrees to either side of the central symmetry line. It was speculated that the recirculating flow along the outer reactor wall directly influences the inlet jet, thus reinforcing and stablizing the bias by exerting more pressure on one side of the jet. However, several instantaneous turbulent eddies acting in concert exerted enough energy to flip the flow. This occurred every few minutes and thus the PIV results averaged over a long time period resulted in a symmetric averaged secondary jet. In the numerical simulation, this time dependency was reflected by the high mesh dependency of the solutions. It was speculated that calculation errors introduced during the iteration allowed the solution to migrate toward the stabilized solutions on either side of the lamp.

Qualitatively, the vectors of velocity magnitude obtained for both structured and unstructured high mesh densities compare well with those measured by PIV. Slight differences can be observed for the recirculation loops where the centers are predicted somewhat higher compared to the PIV results. But for all the CFD simulations, even at high cell densities, the detaching secondary jet below the lamp is not exactly centered.

A qualitative comparison of the CFD predicted symmetrical flow solution along

the reactor's center-plane initially showed only a partial match to the PIV experimental results. The inlet jet, flow structures in the inlet region, the two areas of recirculating flow to the left of the inlet, and the higher velocity along the lower reactor wall were captured (Figure 3.12). However, discrepancies were found in the upper right part of the reactor where the PIV data show returning flow structures that did not occur in the CFD results. It was found that these flow structures occurred in the non-symmetrical CFD simulations.

The flapping flow was found to be the most likely reason; while the symmetry of the inlet plane leads to a centered flow time-averaged solution, the same does not occur along the real reactor center plane. From the lower impingement point, fast flowing layers follow the curvature of the reactor walls diagonally upwards, meeting at the top 12-14 cm along the axis. For both stable states (left and right), these flows, and thus the upper meeting point, are rotated off center to the same degree as the lower impingement point defined by the angle of the secondary jet detaching from the lamp. These two states are not laterally reversed, and the PIV results show a time-average of the rotated flows. A model geometry, with structured mesh and the inlet moved off center by 1 mm, was used to emulate a similar flow by stabilizing the secondary jet on one side. CFD results for this model showed good qualitative agreement with the PIV data along the center plane (Figure 3.12).

The effects of turbulence models in the inlet region were investigated using the off-center CFD model. The z-velocity components of the three tested turbulence models, and PIV data at 6, 12 and 30 cm from the reactor inlet, are shown in Figure 3.13. At 6 cm, the higher flow velocity along the lower wall resulting from the secondary jet, is matched well by all turbulence models. The recirculating flow in the upper half is captured by both κ-ϵ models, while the RSM model underpredicts the velocity of the returning flow. At 12 cm, the lower reactor flow is matched relatively well by all turbulence models. In the upper reactor region, the previously described diagonal flows meet and while the RSM model gave the best match, the velocity profiles are not closely predicted by any of the turbulence models due to the time dependence of this phenomenon. This complex three-dimensional flapping turbulent flow quickly dissipates after this point. Over the following 15 cm, the annular flow velocity equalizes over the reactor's cross-section, finally assuming a plug flow character at around 30 cm, 1/3 of the distance through

the reactor (Figure 3.13c). The flow is then equivalent to the L-shape reactor at 64 cm (Figure 3.7) and remains directly comparable right up to the outlet.

3.4.3 Conclusions

The flow field of water in two reactor geometries, representing annular reactors in general, was simulated by CFD. The investigation focused on the effect of two main modeling parameters (discretisation of the volume and turbulence model) on the numerical solution for both reactor geometries and the results were compared with the experimental PIV data.

The geometry was found to have a large effect on the flow distribution in the first third of the reactor volume. The CFD flow predictions for the L-shape reactor were generally in good agreement with the PIV data, with the exception of the region immediately after the lamp holder. For the U-shape reactor, the inlet geometry with a central annulus separating the inlet jet, introduced an unstable flow resulting in a transient flapping motion that was not captured by the time-averaged CFD results. However, after a stable state of this motion was enforced by a small lateral movement of the inlet resulting in a swirling flow, the CFD simulation data closely matched the PIV findings of the same state. The instability of the fully symetric flow was also reflected in the high mesh dependence and problematic convergence history of the numerical solutions.

It was found that objects in the reactor stream need to be modeled with great care (i.e. lamp holder) as they have a great impact on the flow field. The effects of the inlet region were no longer significant after about one-third of the reactor length for the U-shape and two-thirds for the L-shape reactor. The last third of both reactor geometries showed comparable flow structures.

The study showed that the use of structured grid not only reduced the number of cells needed for a mesh independent solution but also reduced the influence of numerical errors. Mesh independent solutions were achieved using over 0.5 million structured cells per reactor, corresponding to a mean cell volume of 5×10^{-9} m^3. The unstructured mesh was easier to use but needed more cells to achieve similar results.

The effect of the two κ-ϵ and the RSM turbulence models on the final results

were found to be significant in the inlet region. The Standard κ-ϵ model was not well suited for the expanding jet flows that occur in this region. While in most regions the RSM model was somewhat superior to the Realizable κ-ϵ model, the higher mesh dependency (influence of unstructed cells) and computational cost of the former suggest the use of the later. Second-order upwind differentiation is necessary for accurate solutions.

Overal the CFD modeling results were in good agreement with the PIV data for the L-shape reactor, and showed close agreement for the U-shape, when enough care was taken with the choice of mesh structure and turbulence model. These verified CFD models could represent the flow structure for a variety of annular reactors and could be used for UV-reactor performance simulation by integrating reaction kinetics and radiation distribution models with the CFD hydrodynamic model in the reactor.

3.5 Tables and figures

Table 3.1: Comparison of κ-ϵ turbulence models and RSM-model. Several sources contributed to this table (5, 7, 14, 17).

Model	Advantages	Disadvantages
Standard κ-ϵ	• Simplest model to represent variation of turbulence length and velocity scales • Robust and economical • Good performance in many industrial flows • Most widely validated model	• Assumes isotropic eddy viscosity • Performs poorly for: - unconfined flows - rotating flows - non-circular ducts - curved boundary layers
Realizable κ-ϵ	• Compensates for large strain rates and streamline curvature • Resolves round-jet anomaly • Better for impinging and separating flows	• Assumes isotropic eddy viscosity • Not sufficiently validated
RSM	• Most general model of all classical turbulence models • Performs well for complex flows including non-circular ducts and curved flows • Resolves swirling flows	• Computationally expensive (+7 PDEs) • Sometimes as poor as κ-ϵ due to problems with ϵ equation • Prone to convergence difficulties • Not widely validated

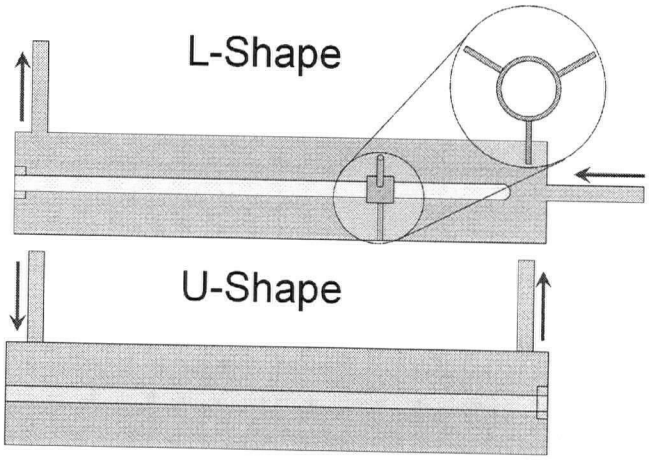

Figure 3.1: Schematic diagram of the L- and U-shape reactors. The inlet and outlets are indicated by arrows. The lamp holder in the L-shape reactor is enlarged.

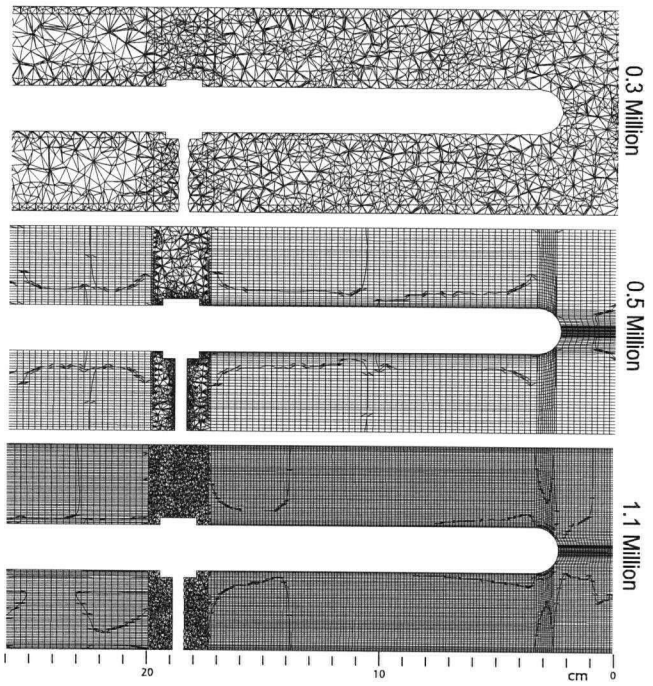

Figure 3.2: Meshes used in L-shape reactor. From the top to the bottom there are: Fully unstructured, structured with low mesh density and structured with high mesh density. The lamp holder region could not be meshed with structured cells and remained unstructured.

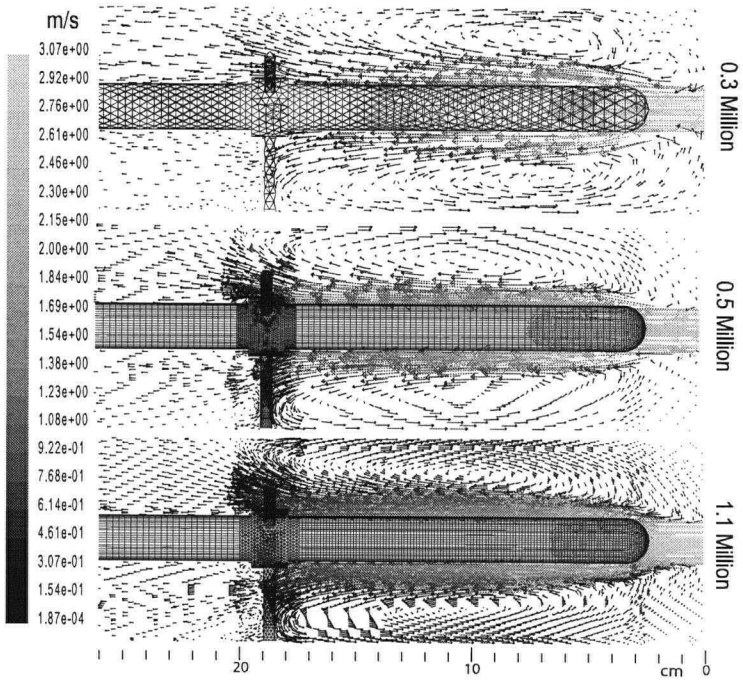

Figure 3.3: Vectors of velocity magnitude in the L-shape reactor. Results were obtained using the Realizable κ-ϵ turbulence model and the meshes described in Figure 3.2 (only every fourth velocity vector is shown).

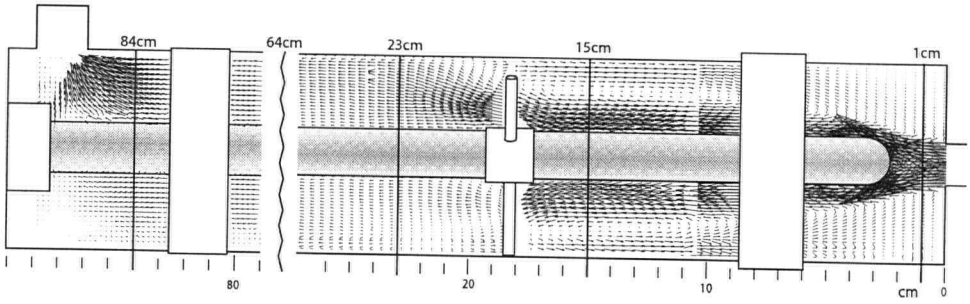

Figure 3.4: Vectors of velocity magnitude from PIV experimental data at center plane of L-shape reactor. Positions used for quantitative comparison are shown as vertical lines at different distances from the reactor inlet (see Figure 3.7).

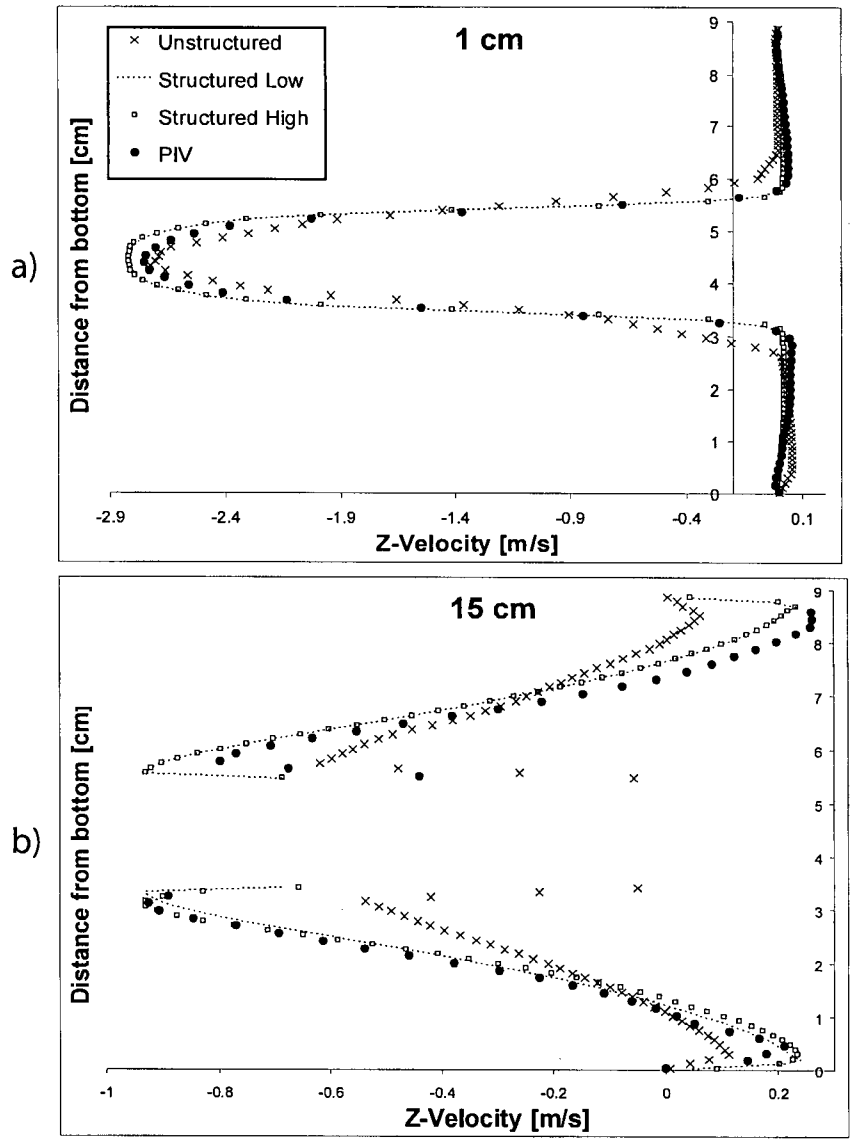

Figure 3.5: Quantitative comparison of the (axial) z-velocity component obtained using the three mesh structures give in Figure 3.2. Data are extracted from CFD and PIV results (Figure 3.3) at positions 1 and 15 cm from the reactor inlet (Figure 3.4)

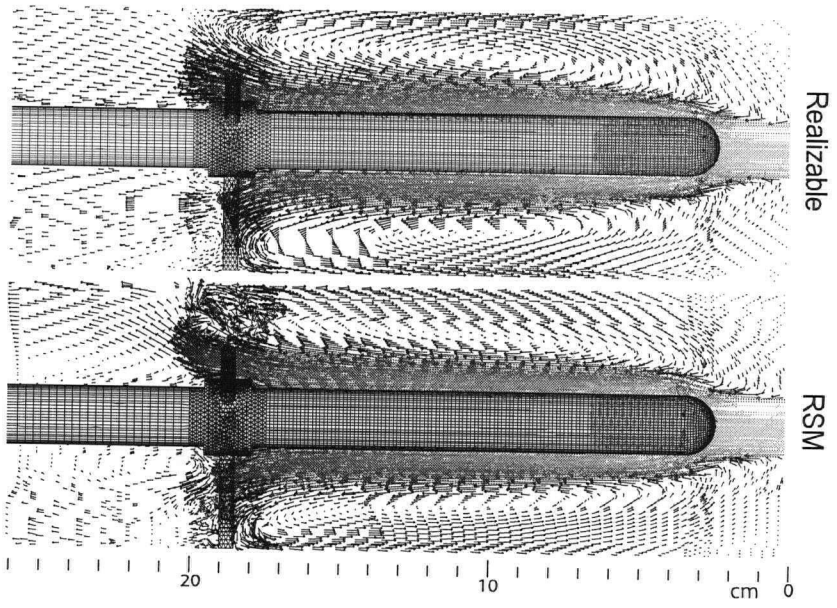

Figure 3.6: Vectors of velocity magnitude in the L-shape reactor. Realizable κ-ϵ and Reynolds Stress Model (RSM) are results compared. The RSM model exhibits instabilities in the unstructured mesh of the lamp holder region at different distances from the reactor inlet (see Figure 3.4).

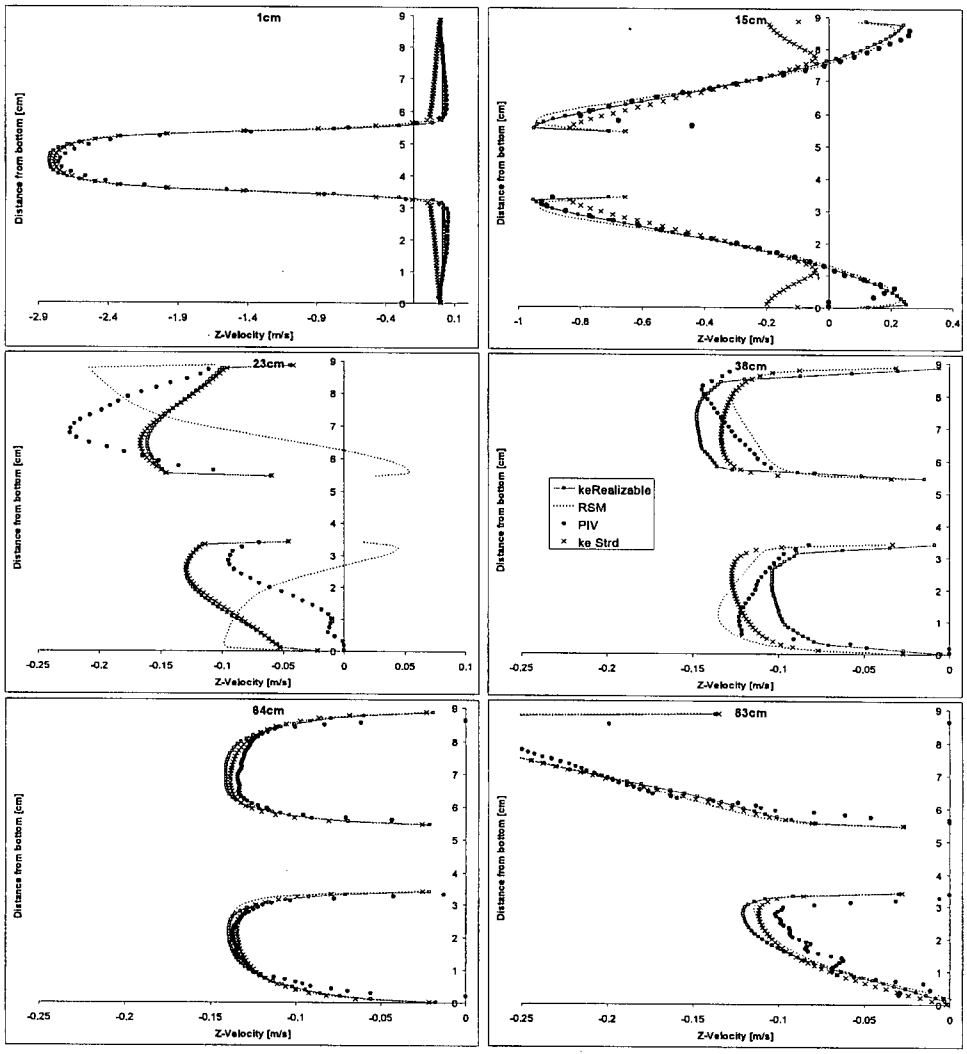

Figure 3.7: Z-velocity from three turbulence models in the L-shape reactor. Comparison of model results to PIV data at different distances from the inlet.

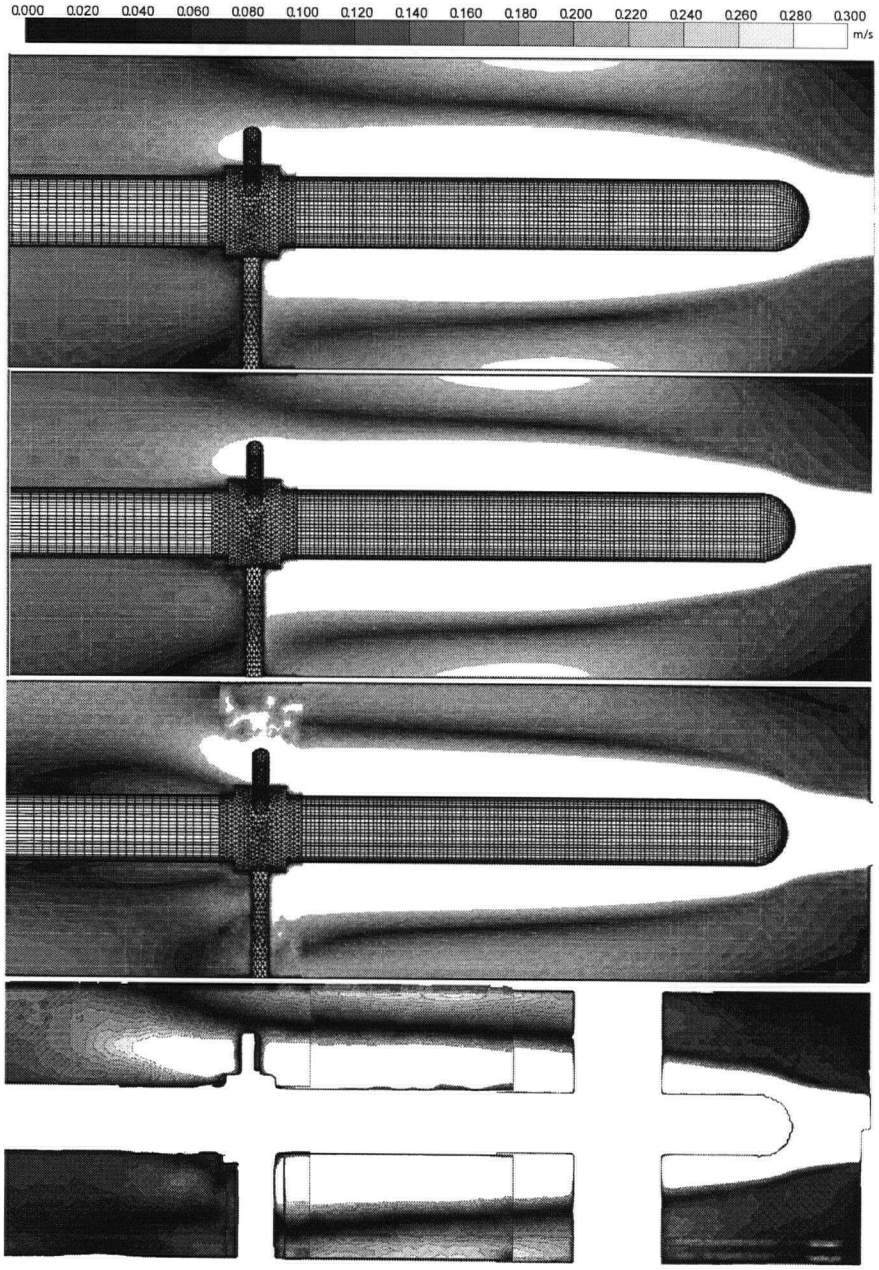

Figure 3.8: Contours of velocity magnitude, center plane of the L-shape reactor. a) Standard κ-ϵ, b) Realizable κ-ϵ, c) RSM, and d) PIV experimental values.

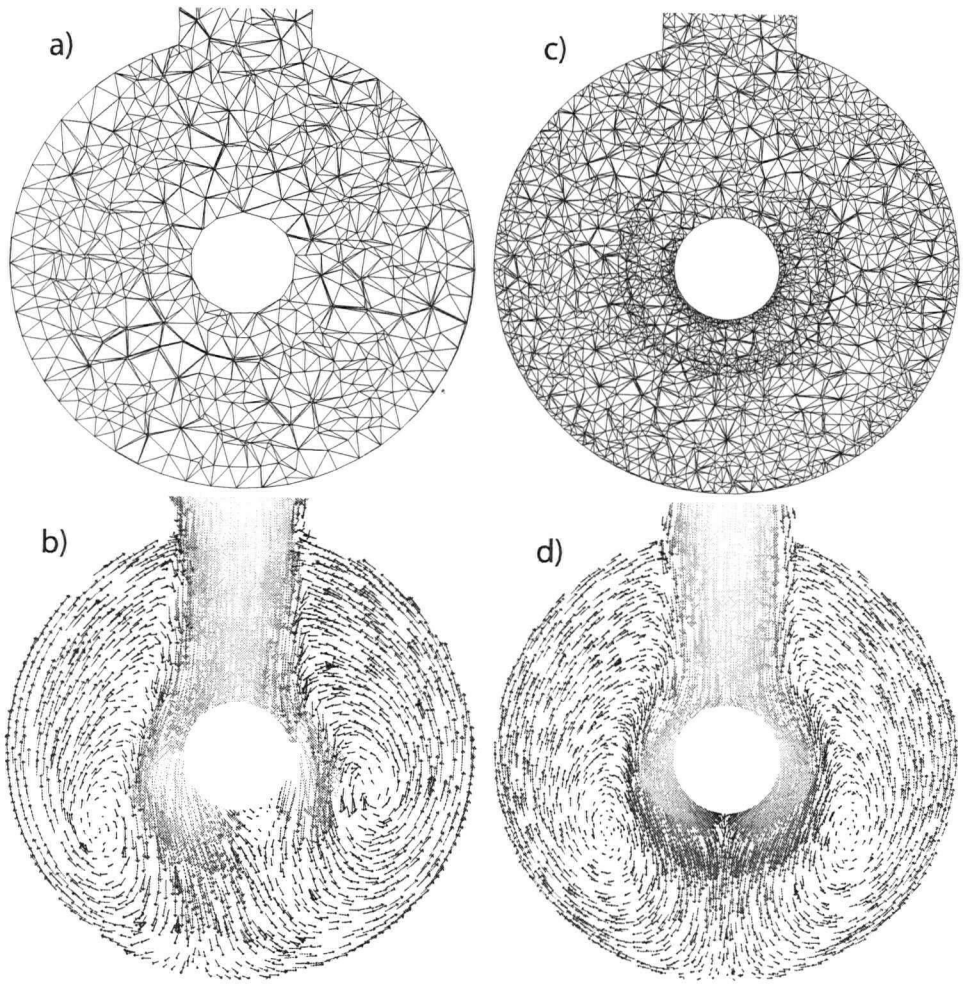

Figure 3.9: Influence of unstructured mesh density on the vertical cross-section centered below the inlet tube (a and c) on CFD velocity magnitude calculations (b and d) for the U-shape inlet plane perpendicular to the reactor body. Number of cells in the inlet volume a = 16,000 and c = 175,000

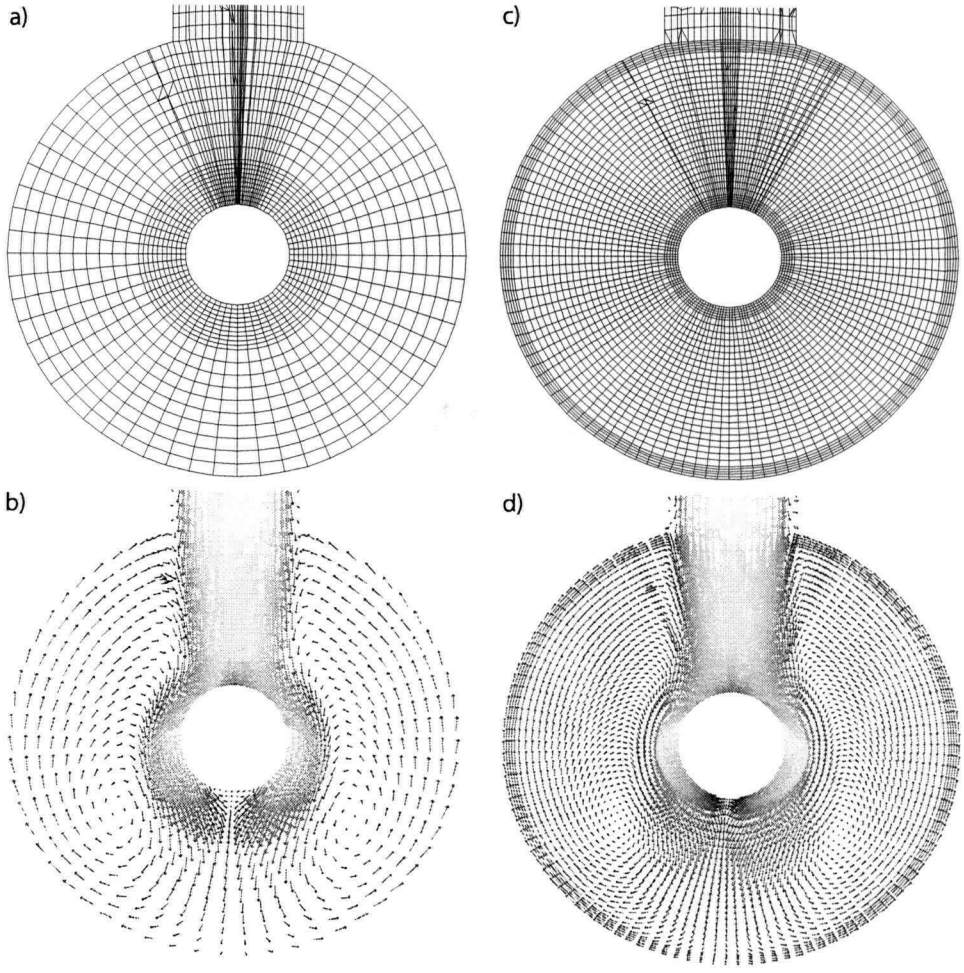

Figure 3.10: Influence of structured mesh density (a and c) on CFD velocity magnitude calculations (b and d) for the U-shape inlet plane. Number of cells in the inlet volume a = 31,000 and c = 122,000

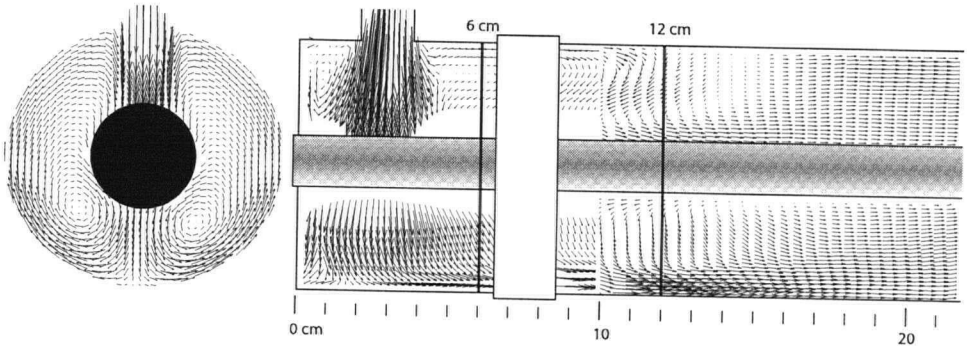

Figure 3.11: Vectors of velocity magnitude from PIV experimental data for the inlet plane (left) and center plane (right) of the U-shape reactor.

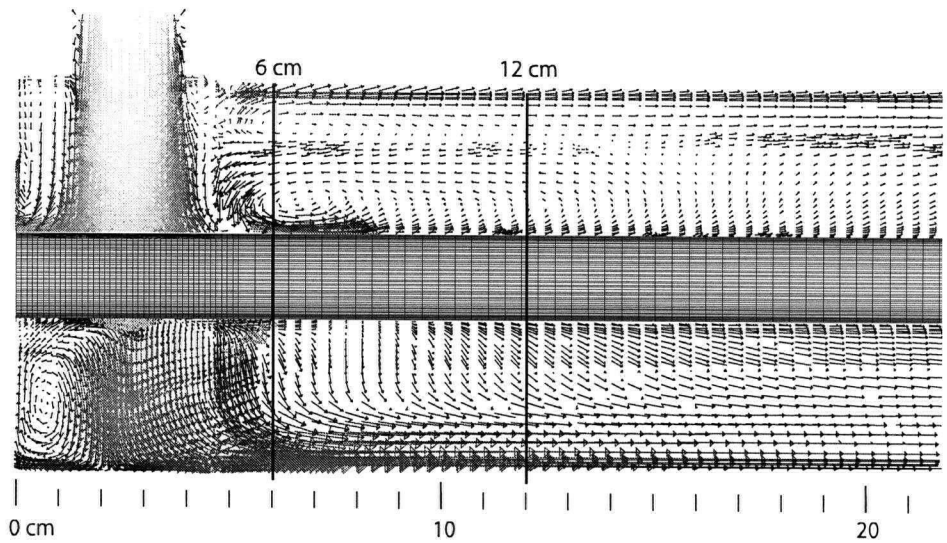

Figure 3.12: Vectors of velocity magnitude on the center plane of the U-shape reactor using the Realizable κ-ϵ turbulence model. The inlet was moved 1 mm off-center, stabilizing the flow to one side of the lamp.

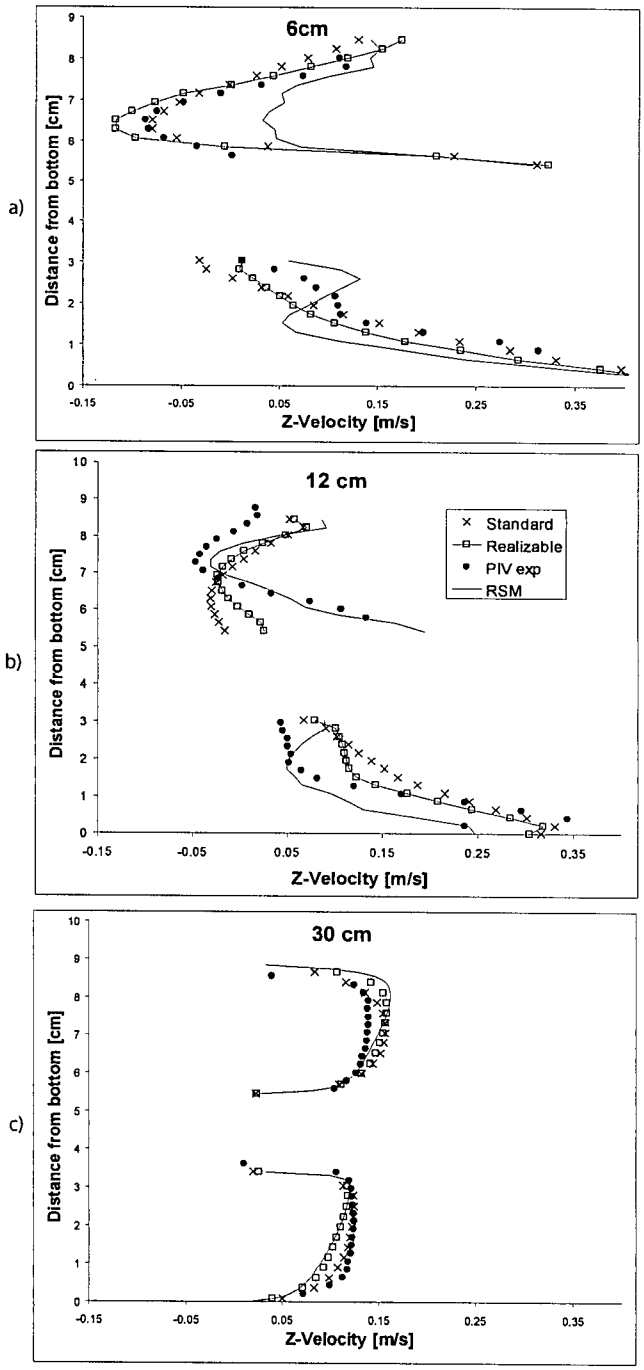

Figure 3.13: Z-velocity comparison of three turbulence models to PIV results for the U-shape reactor.

Bibliography

[1] BAKKER, A., HAIDARI, A. H., AND MARSHALL, E. M. Design reactors via cfd. *CEP Magazine December* (2001), 30–39.

[2] CASSANO, A. E., MARTIN, C. A., BRANDI, R. J., AND ALFANO, O. M. Photoreactor analysis and design: Fundamentals and applications. *Industrial & Engineering Chemistry Research 34* (1995), 2155–201.

[3] DOUGLAS, R. W., CAREY, G. F., WHITE, D. R., HANSEN, G. A., KALLINDERIS, Y., AND WEATHERHIL, N. P. Current views on grid generation: Summaries of a panel discussion. *Numerical Heat Transfer B:Fundamentals* (2002).

[4] ESCUDIER, M. P., AND SMITH, S. Turbulent flow of newtonian and shear-thinning liquids through a sudden axisymmetric expansion. *Experiments in Fluids 27* (1999), 427–434.

[5] FLUENT. *Fluent user guide: Chapter 10. Modeling turbulence.* Fluent, 2003.

[6] HU, H., KOBAYASHI, T., SAGA, T., SEGAWA, S., AND TANIGUCHI, N. Particle image velocimetry planar laser-induced fluoroscence measurements on lobed jet mixing flows. *Experiments in Fluids Suppl* (2000), 141–157.

[7] JAW, S. Y., AND CHEN, C. J. Present status of second order closure turbulence models. i:overview. *Journal of Enineering Mechanics May* (1998), 485–501.

[8] J.O.HINZE. *Turbulence.* McGraw-Hill Publishing, 1975.

[9] KAMIMURA, M., FURUKAWA, S., AND HIROTSUJI, J. Development of a simulator for ozone/uv reactor based on cfd analysis. *Water science and technology : a journal of the International Association on Water Pollution Research 46* (2002), 13–19.

[10] MEYERS, K. J., WARD, R. W., AND BAKKER, A. A digital particle image velocimetry investigation of flow field instabilities of axial flow impellers. *Journal of Fluids Engineering 119* (1997), 623–631.

[11] PAREEK, V. K., COX, S. J., BRUNGS, M. P., YOUNG, B., AND ADESINA, A. A. Computational fluid dynamic (cfd) simulation of a pilot-scale annular bunbble column photocatalytic reactor. *Chemical Engineering Science 58* (2003), 859–865.

[12] PIRNIE, M., LINDEN, K. G., AND JAMES P. MALLEY, J. Ultraviolet disinfection guidance manual, draft epa 815-d-03-007. *USEPA* (2003).

[13] PRUVOST, J., LEGRAND, J., LEGENTILHOMME, P., AND DOUBLIEZ, L. Particle image velocimetry investigation of the flow-field of a 3d turbulent annular swirling decaying flow induced by means of a tangential inlet. *Experiments in Fluids 29* (2000), 291–301.

[14] RANADE, V. V. *Computational flow modeling for chemical reaction engineering.* Academic Press, 2002.

[15] RANADE, V. V., PERRARD, M., SAUZE, N. L., XUEREB, C., AND BERTRAND, J. Trailing vortices of rushton turbines: Piv measurements and cfd simulations with snapshot approach. *Transactions in Chemical Engineering 79A* (2001), 3–12.

[16] RESEARCH, M. The us market for ultraviolet water treatment equipment. *MarketReaserach.com 2000* (1999), 2–5. MarketLooks.

[17] RODI, W. *Turbulence models and their application in hydraulics.* IAHR, 1979.

[18] ROMERO, R. L., ALFANO, O. M., MARCHETTI, J. L., AND CASSANO, A. E. Modeling and parametric sensitivity of an annular photoreactor with complex kinetics. *Chemical Engineering Science 38* (1983), 1593–1605.

[19] SCHOENEN, D., KOLCH, A., AND GEBEL, J. Influence of geometrical parameters in different irradiation vessels on uv disinfection rate. *International Journal of Hygiene and Environmental Medicine 194*, 3 (1993), 313–320.

[20] UNLUTURK, S. K., H.ARASTOOPOUR, AND KOUTCHMA, T. Modeling of uv dose distribution in a thin-film uv reactor for processingof apple cider. *Journal of Food Engineering 65*, 1 (November 2004), 125–136.

[21] WRIGHT, N. G., AND HARGRAVES, D. M. The use of cfd in the evaluation of uv treatment systems. *Journal of Hydroinformatics* (2001).

Chapter 4

Integrated UV reactor model development

In this chapter, further development of the verified computational fluid dynamics (CFD) model for the simulation of UV reactor performance is described. The integration of UV-radiation models into Fluent is described in the first part. In the second part, the integration of reaction kinetics into the CFD model is specified and the integrated model is evaluated against the experimental results.

4.1 Introduction

Alternative water treatment methods have gained popularity, due to increasingly stringent environmental regulations and concerns regarding chemical treatment methods. UV-based technologies, especially, have seen a rapid growth over the last decade (13). The use of UV-radiation for disinfection relies on the inactivation of microorganisms through changes in the pathogens DNA (i.e. formation of thymine dimers), rendering them unable to reproduce. UV application for advanced oxidation processes (AOPs) involves exciting a strong oxidant such as H_2O_2 or O_3 to generate highly reactive hydroxyl radicals to oxidize (toxic) organic substrates. In both applications, the local rate of reaction is linked to the non-uniform radiation distribution (UV-fluence rate). Reactor performance is thus strongly dependent on hydrodynamic transport processes, influencing the spatial distribution of the microorganisms or toxic substrates. The influence of the flow field and reactor

geometry on the performance of disinfection systems has been demonstrated by Schoenen et al. (15) and Chiu et al. (4), while the effect of interactions between reactor hydrodynamics and local radiation fluence on contaminants in AOPs was shown by Pareek et al. (12).

In a UV-reactor, the fluid behavior defines the spatial concentration distribution and flow of chemical agents or microorganisms through the reactor volume. UV-lamp(s) supply the radiation driving the main reaction with fluence rate attenuated by distance and transmittance of the media. Finally, the reaction rate is determined by the local UV-fluence rate, concentration of the species, and the kinetic rate constants. Modeling photo-reactors therefore involves three submodels for hydrodynamics, radiation fluence rate distribution, and UV-reaction kinetics that are coupled by the material and energy balances.

The use of advanced numerical simulation tools, in particular computational fluid dynamics (CFD), to model the flow and transport in chemical engineering processes has attracted much attention in recent years, e.g. (1, 12, 17). Integrated CFD models have also been used to simulate photo-reactor performance, e.g. (4, 7, 9). A key advantage of simulating reactor performance by solving the governing equations of the system is the virtual prototyping capability, allowing for a rapid evaluation of design alternatives.

The objective of this work was to implement an integrated numerical model using CFD coupled with a UV-radiation model and (volumetric) reaction rates to evaluate UV-disinfection reactors. A commercial CFD code, Fluent 6.2, provided the necessary code extensions to implement and execute the described submodels. Annular UV-reactors with a concentric lamp parallel to the reactor axis, representing a widely used design for UV-reactors, were investigated. Both, continuum (Eulerian) and dispersed phase (Lagrangian) approaches to disinfection modeling were implemented, combining a spatial UV-fluence rate model with first order kinetics for disinfection. The effect of UV-radiation models on reactor performance was studied by considering infinite line source and finite line source models. The numerical disinfection efficiency (log reduction) for two reactor geometries, inlet normal to the reactor axis (U-shape) and inlet parallel to the reactor axis (L-shape), were compared for several flow rates. The log reduction for a commercially available annular UV-reactor was then simulated based on the technical data and

biodosimetry results provided by R-can.

4.2 Modeling setup

4.2.1 Flow model

Two annular reactor geometries with different inlet positions (L- and U-shape) but similar dimensions (Table 4.1) were used in this study (Figure 4.1). The reactors contained an annular UV-lamp and inlet/outlet ports located 3.81 cm (1.5 inch) from either end for the U-shape, or with the inlet concentric on the front-plate for the L-shape reactor. A third industrial prototype UV-reactor, designed by R-Can Environmental Inc, provided the basis for the comparison of model predictions to the biodosimetry results. This L-shape design contained a larger lamp holder and an additional baffle close to the outlet, both of which were accounted for (Figure 4.1c).

Reynolds Averaged Navier Stokes (RANS) steady-state equations, derived from the general form of the governing equations for the conservation of mass

$$\frac{\partial \rho}{\partial t} + \nabla \cdot (\rho \, \vec{\nu}) = 0 \tag{4.1}$$

and the conservation of momentum,

$$\frac{\partial}{\partial t}(\rho \, \vec{\nu}) + \nabla \cdot (\rho \, \vec{\nu}\vec{\nu}) = -\nabla P + \nabla \cdot (\bar{\bar{\tau}}) + \rho g \tag{4.2}$$

where ρ is density, $\vec{\nu}$ is velocity, P is pressure, $\bar{\bar{\tau}}$ is the stress tensor and g is the gravitational acceleration, were solved by a finite volume based commercial CFD software package (Fluent 6.2). In RANS simulations, the time-averaged momentum transport equations are closed by modeling the momentum flux terms (Reynolds stresses) using a turbulence model. In this work, the realizable κ-ϵ turbulence model was used. The influence of discretisation (meshing) and choice of turbulence model on the hydrodynamic flow field in annular reactors was examined by comparing the predicted results with those obtained experimentally using particle image velocimetry (PIV) as was discussed elsewhere (Chapter 3). For these reactor geometries, the verified hydrodynamic models were established using

a mix of structured and unstructured meshes (0.5-1 million cells). No-slip boundary conditions were set at the reactor walls and the UV-lamp. The inlet boundary conditions were defined as a mass flow with the fluid properties of liquid water and 10% turbulent intensity over the diameter. An inlet tube with an $\frac{L_1}{D_1} = 45$ ensured a fully developed flow entering the reactor. Numerical convergence was defined at scaled residuals smaller than 1×10^{-5} for second order upwind solutions.

4.2.2 UV-fluence rate models

Assuming uniform optical properties of the fluid, the UV-fluence rate at any given point can be described independent of the flow field, as a function of the distance to the source, the optical transmissivity of the fluid, and the initial UV-output (2). The assumption implies low concentrations of contaminants and little or no change in the optical behavior of the reacting agent, which are appropriate for the case of UV-disinfection. Monochromatic UV-fluence models of increasing complexity, from one-dimensional radial to discrete ordinate (DO), have been proposed. Liu et al. (8) showed that, in many situations, shadowing, reflection and refraction effects have little influence on the final distribution. For the present study, two UV-models describing the spatial distribution of fluence rate were implemented in the reactor performance model to calculate the fluence rate at each point as a function of its distance from the lamp and the UV-transmittance of the medium.

4.2.2.1 Infinite line source or radial model

This model assumes the lamp to be represented as a line source with radiation emitted normal to the lamp axis. The fluence rate E, is related to the UV-lamp radiant power per unit length and the radial distance, r [cm], from the lamp center line (16). Simplified for an axisymmetric annular system, the local fluence rate, $E(r)$, is expressed as

$$E(r) = \frac{\frac{P}{L}}{2\pi r} exp\left[\sigma_w(r - r_L)\right] \tag{4.3}$$

where P is the total germicidal lamp output [mW], L is the axial lamp arc length [cm], r_L is the lamp sleeve radius [cm] and σ_w is the absorption coefficient of the

fluid [cm^{-1}]. σ_w can be calculated from the transimissivity, T,by following equation

$$\sigma_w = ln(10)log(T) \tag{4.4}$$

This model does not deal with refraction or reflection and cannot describe what happens near the lamp ends, but is easy to implement and has been shown to perform reasonably well for standard reactor sizes (8).

4.2.2.2 Finite line source or multiple point source summation (MPSS) model

In this method the lamp is approximated as a series of point light sources emitting radiation in all directions (2). The UV-fluence at each location in the domain is estimated as the sum of energy received from each individual point source in the system:

$$E(r,z) = \sum_{i=1}^{n} \frac{\frac{P}{n}}{4\pi l_i^2} exp\left[-\sigma_w (r - r_L)\frac{l_i}{r}\right] \tag{4.5}$$

where z [cm] represents the axial distance and l_i the distance from the current location [cm] to the point source number n_i out of a total of n sources. Results were found to be independent of the number of sources with $n = 100$ for the present models. Fluence rate changes over the length of the lamp and diffuse radiation at the lamp ends are predicted with this model, but it has been suggested that the model overpredicts fluence rates close to the lamp surface (8).

4.2.3 Disinfection kinetics model

MS2 bacteriophage biodosimetry is the method of choice for log inactivation studies of UV-disinfections systems and a standardized protocol is available from the US-EPA Environmental Technology Verification (ETV) program. MS2 is non-pathogenic to human, has a relatively high UV-resistance and, being a single stranded RNA virus, its dose response for UV-inactivation can be described by conventional first order Chick-Watson kinetics:

$$N = N_0 e^{-kEt} \tag{4.6}$$

where N_0 represents the initial organism concentration (plaque forming units per ml)[PFU/ml] and N the organism concentration after UV-exposure [PFU/ml], k is the inactivation rate constant [cm^2/mJ], E is the UV-fluence rate [mW/cm^2], and t is the exposure time [s]. Dose (sometimes referred to as fluence) is defined as the UV-fluence rate multiplied by the time, i.e. $D = E \times t$ [mJ/cm^2]. In general usage, the SI units are exchanged for the equivalent but more manageable units shown here (3).

Dose response curves are measured under tightly controlled conditions using a collimated beam of UV to eliminate the influence of hydrodynamics and non-uniform fluence rates, and are recorded as the log inactivation ($log\frac{N_0}{N}$) per unit dose. The rate constant k in Equation 4.6 can be obtained from the slope of $\frac{log\frac{N_0}{N}}{log(e)}$ plotted against dose D. Each culture of MS2 macrophages has to be calibrated separately, but an inactivation constant of $k = 0.1$ cm^2/mJ has been reported by several sources (10, 11, 14).

4.2.4 Integrated reactor performance model

For disinfection reactions in continuous reactors, the path a microorganism takes is key to the amount of UV-radiation (dose) it absorbs. The position of microorganisms in the reactor can be tracked in the Eulerian or Lagrangian reference frames. In the Lagrangian framework, after obtaining the velocity field by solving the transport equations, single organisms are treated as discrete particles where the trajectory is predicted by integrating the force balance on the particle. Random effects of turbulence on the particle are accounted for by the Discrete Random Walk (DRW), or "eddy lifetime" model, where the interaction of a particle with a succession of discrete stylized fluid phase turbulent eddies is simulated (6). The particle trajectories are computed based on a steady continuous-phase flow field. A statistically significant number of particles (representing microorganisms) is released at the reactor inlet (N_0) and the dose is integrated along the path of each particle, multiplying the average local fluence rate (E) by the time step Δt. For each dose interval i, the number of remaining vital particles (microorganisms) N_i is calculated by:

$$N_i = \alpha_i \times N_0 e^{-kD_i} \tag{4.7}$$

where α_i is the fraction of particles that receive the dose D_i, k is the inactivation rate constant and D_i is the average dose for the i^{th} bin interval. The sum of all vital particles over the entire range of doses yields the estimated total number of vital particles (microorganisms) leaving the reactor, N:

$$N = \sum N_i \tag{4.8}$$

In the Eulerian framework, the conservation equation of species (microorganisms) is solved along with the transport equations. The local mass fraction of each species, is predicted through the convective-diffusion equation for the species, to calculate the concentration of living bacteria through the domain:

$$\frac{\partial C}{\partial t} + \nabla \cdot (\vec{\nu}\, C) = -\nabla \cdot \vec{J} + R \tag{4.9}$$

where $\vec{J}$ is the diffusion flux of the species and the rate of inactivation R is defined as:

$$R = -kEC \tag{4.10}$$

where E is the local fluence rate and C the microorganism concentration. For the RANS equation of species conservation, the eddy dissipation model was used to solve the transport equations of the species (5). After discretisation of the reactor domain into small cells, volumetric reaction rates are calculated based on the local fluence rate and microorganism concentration for each cell. Each cell is thus treated as a completely mixed reactor with locally uniform microbial concentration and UV-fluence and a reaction rate defined by Equation 4.10.

4.3 Experimental work

A stock solution of MS2 (*E. Coli bacteriophage* ATCC 15597-B1) was prepared, according to the ISO 10705-1 protocol, using an E. Coli host (*E. Coli* ATCC 15597). MS2 was added to the feed tank in a concentration of 1×10^6 PFU/mL. Samples of 50 mL were taken at the reactor inlet and outlet after steady state was reached. The samples were then plated out on a double layer agar and the plaque forming units (PFU) counted, according to the US-EPA manual (18). Experimental results

were provided by R-Can Inc.

4.4 Results and discussion

4.4.1 Fluence rate

Figure 4.2a shows a two-dimensional representation of the UV-fluence rates in the annular reactor as calculated by the MPSS and radial lamp models for a germicidal UV-output of 35 W over the 80 cm lamp arc at a UV-transmissivity of 70% (per cm) for the fluid. The contours of fluence at the lamp ends clearly illustrate the differences between the two modeling approaches. UV-fluence rates from the reactor walls to the lamp surface ranged from 100–8 mJ/cm^2 for the MPSS to 60–5 mJ/cm^2 for the radial model. The radial profiles (Figure 4.2b) show that the MPSS model predicts higher fluence rates than the radial model close to the lamp surface; this corresponds to the model limitations described by Blatchley (2). Both models predict reasonable values at distances of 2.5 cm and more from the lamp and show good agreement with experimental UV-fluence rate measurements on the basis of actinometry (Liu et al. (8)). Closer to the UV-source where the models show the greatest deviation from each other, however, experimental measurements for model evaluation are hard to obtain due to physical limitations (the radius of the actinometry spheres is too large). In the UV-reactor configuration under study, with a lamp radius of 1 cm and a tube radius of 4.45 cm, much of the reactor volume lies within the zone where the MPSS model predicts a higher fluence rate than the radial model.

4.4.2 Lagrangian approach for simulating reactor performance

The dose distributions for an annular L-shape reactor with a flow rate of 25 GPM was estimated based on the Lagrangian tracking of microorganisms as described earlier. Figure 4.3 shows particle trajectories calculated by the random walk model, colored by the absorbed dose. Consistent results were found by releasing 10,000 or more particles in batches of 500 uniformly distributed over the reactor inlet. The

doses received by the microorganisms were in the range of 21-270 mJ/cm^2 with an average of 68 mJ/cm^2 (Figure 4.4). Short circuiting, where microorganisms predominantly pass quickly through regions of lower fluence rate, does not occur (no peak at lower doses), but the wide-spread and non-uniform dose distribution shows that the hydrodynamic efficiency can be improved. Better mixing throughout the domain might lead to a narrower dose distribution and thus more efficient use of the radiation energy. A log reduction of 1.87 was calculated from the dose distribution for a disinfection rate constant of k=0.1 cm^2/mJ.

4.4.3 Eulerian approach for simulating reactor performance

The concentration distribution of active microorganisms within the same L-shape reactor was estimated using the Eulerian method. Figure 4.5a shows the concentration distribution of living microorganisms within the reactor on a log scale where higher concentrations are represented by darker shades. The effect of the non-uniform fluence rate distribution on the concentration of non-reacted or "living" microorganisms is clearly visible. The contours of similar concentration are strongly slanted, with lower concentrations close to the lamp surface appearing earlier on the reactor axis. The contours of local reaction rates presented on a log scale in Figure 4.5b show similar tendencies but with a less distinct influence of the flow. This is understandable since reaction rates are a function of both the stationary fluence rate as well as the flow dependent microorganism concentration. In Figure 4.5b, the effect of flow recirculation is evident at the reactor inlet near the reactor walls, where despite low fluence rates, relatively high reaction rates are observed due to higher residence times. The average mass fractions of microorganisms at both inlet and outlet of the reactor are determined through integration to calculate the reactors total inactivation rate, resulting in a log reduction of 2.07; 10% higher than that predicted by the Lagrangian model.

4.4.4 Comparison of inactivation in two reactor geometries

The influence of reactor geometry, flow rate, and radiation model on the Eulerian and Lagrangian reactor performance predictions was investigated. The Eulerian microorganism concentration and Lagrangian dose distribution for both L- and U-

shape reactor geometries, using the MPSS radiation model at a UV-transmissivity of 70%, are presented in Figure 4.6 for a mass flow rate of 25 GPM. The influence of the reactor geometry is clearly visible in the inlet region and along the lower reactor wall where higher flow speeds in the U-shape reactor lead to lowered local rates of disinfection (Figures 4.6b and d). This qualitative view of microorganism concentration distribution can be helpful to identify the areas of short circuiting. This non-ideal behavior is also discernible through a shoulder in the lower ranges of the Lagrangian dose distribution where some particles receive less than 20 mJ/cm^2 in the U-shape reactor (Figure 4.6c). Microorganisms in this dose range did not receive enough dose to be disinfected effectively by remaining far from the radiation source and passing through the reactor volume at a high velocity. The secondary distribution curves in Figures 4.6a and c, indicate the number of non-inactivated microorganisms and show that the mean dose is of little importance on the reactor performance, since unreacted microorganisms affecting the log total reactor reduction only occur in significant numbers at lower doses. The distribution profile also shows the number of organisms that receive very high doses, uncovering the inefficient use of UV-radiation.

For the quantitative comparison of L- and U-shape reactors at various flow rates, the inlet flows of 10, 15, 25 and 35 GPM (6.3×10^{-4}, 9.5×10^{-4}, 15.8×10^{-4}, 22.1×10^{-4} m^3/s) were simulated, using the MPSS radiation model at a UV-transmissivity of 70%. The log reduction results for both reactor geometries using the Lagrangian approach are shown in Figure 4.7. While the L-shape reactor performed better for the tested flow range, the performance difference of the L-shape and U-shape reactors was dependent on the flow rate. The differences relative to the L-shape results ranged from 14% at 10 GPM to 3% at 35 GPM. This is consistent with the notion of short circuiting occurring in the U-shape reactor. As Figures 4.6a and c show, reactor performance is largely defined by the slow reaction rates of microorganisms receiving lower doses. At high flow rates, the short residence time results in an overall shift to the lower dose range. Short circuiting in the U-shape reactor still occurs, but has less influence on the total log reduction levels reached. At lower flow rates, microorganisms reach higher overall doses and the L-shape reactor performs well. In the U-shape reactor, on the other hand, short circuiting still occurs and its influence on reactor performance is more pronounced.

A relative performance increase of 10% for the L-shape, in the target log reduction range is substantial. The fact that this performance gain is evoked by a simple change in inlet placement underlines the importance of including hydrodynamic considerations into reactor design.

To study the impact of radiation models on the reactor performance results, the L- and U-shape reactors were simulated using the infinite line source (radial) and finite line source (MPSS) radiation models. For the given reactor dimensions, where the reactor walls are only 4.45 cm from the lamp surface, the lamp models have a marked influence on the simulated reactor performance (Table 4.2). The radial lamp model shows a $26 \pm 1.5\%$ lower log reduction over the entire calculated range of flow rates; the same relative difference was observed for both reactor geometries. This is consistent with the noted higher UV-output predicted in the near lamp region for the MPSS model (Figure 4.2) and demonstrates the importance of using an accurate radiation model in reactor performance simulations.

4.4.5 UV-reactor model evaluation

To experimentally verify the reactor performance models, the log reduction of a commercial annular L-shape UV-disinfection reactor was simulated (dimensions in Table 4.1). The main details of the internal reactor geometry, including a more complex lamp holder at the inlet and a reduction ring close to the outlet, were considered in the simulation. The reactor performance was calculated, implementing the integrated CFD model by discretizing the domain with 0.7 million cells, accounting for turbulence with the realizable κ-ϵ model and applying both Lagrangian and Eulerian disinfection models.

The log reductions predicted by the Lagrangian and Eulerian methods for a range of flow rates at a transmissivity of 70% are presented in Figure 4.8. Transmissivity and the reaction rate constant k=0.1 were obtained from experimental measurements. Both modeling approaches show very similar responses in regards to the influence of flow rate on the log reduction. For a flow of 10 GPM, the difference between the two methods was 11% and decreased to about 4.5% at a flow rate of 35 GPM. Similar trends in reactor performance difference using the Eulerian and Lagrangian models were observed for the L- and U-shape geometries (Explained in

section 4.4.4). The deviation between the Eulerian and Lagrangian methods has not been examined in depth, but possible causes are the different approaches taken by the two models, the numerical errors from the choice of the finite-rate reaction model (eddy-dissipation model used), and the inclusion of turbulent diffusion in the Eulerian model, that does not occur in the Lagrangian model. Both modeling results show a good agreement with the biodosimetry measurements performed for this reactor. Like most biological assays, biodosimetry has a considerable variance and not enough experimental values were available for a detailed comparison of the modeling approaches. However, the results indicate the possibility of modeling a UV-reactors performance to a close degree, knowing the geometrical specifications and operating conditions using either Lagrangian or Eulerian approaches.

4.5 Conclusions

Disinfection models based on the Lagrangian and Eulerian methods were successfully implemented in a commercial CFD code and provided results in good agreement with the experimental data over a range of flow rates. Though the Lagrangian and Eulerian methods could be used interchangeably, the final log reduction results deviated between 4-11 percent for the tested range of flow rates. Both models can be used to gain complimentary information on the same reactor; while the Lagrangian method provides estimates of the UV-dose distribution and the particle tracks visualize flows patterns, the Eulerian approach shows the concentration distribution and local reaction rates. The combined information can be used to predict and monitor reactor performance levels and to enhance the reactor designs. At a higher computational cost, the Eulerian model delivers a more conclusive image of the local disinfection rates within the reactor volume. More importantly, this model can be extended to UV-based Advanced Oxidation Processes, which involve additional volumetric reactions, by including further reaction steps.

The model parameters have a significant impact on the final simulation results. In this study, the selection of finite line source or infinite line source radiation model was found to influence the reactor performance results by about 26 %. While costly and time consuming construction of intermediate prototypes can be reduced through the use of UV-reactor simulations, complimentary experiments

remain necessary to verify reactor performance, for the final UV-reactor designs.

4.6 Tables and figures

Table 4.1: Dimensons for the L-shape, U-shape and industrial prototype (L-shape) reactor geometries.

	U-shape + L-shape	**Prototype**
Reactor body		
Diameter	8.9 cm (3.5 inch)	8.6 cm
Length	88.9 cm (35 inch)	101 cm
Lamp		
Diameter	2 cm	2.26 cm
Arc Length	80 cm	88 cm
Power.	35 W	35 W
Inlet/Outlet		
Diameter	1.91 cm (0.75 inch)	2.24 cm
Length	85 cm (34 inch)	100 cm

Table 4.2: Log reduction results over a range of flow rates for the L-shape reactor. Comparison of radial and MPSS lamp radiation models using both Eulerian and Lagrangian approaches. The lamp models consistently show about $26 \pm 1.5\%$ difference in log reduction

		10 GPM		**15 GPM**		**25 GPM**		**35 GPM**	
L-shape		Eul.	Lagr.	Eul.	Lagr.	Eul.	Lagr.	Eul.	Lagr.
	Radial	3.10	2.71	2.31	2.04	1.50	1.36	1.12	1.07
	MPSS	4.18	3.64	3.15	2.79	2.07	1.87	1.55	1.45
	% difference	25.8	26.1	26.6	26.8	27.4	27.2	27.8	26.3
U-shape		Eul.	Lagr.	Eul.	Lagr.	Eul.	Lagr.	Eul.	Lagr.
	Radial	2.76	2.41	2.03	1.88	1.37	1.29	1.08	1.04
	MPSS	3.66	3.16	2.71	2.44	1.86	1.72	1.45	1.39
	% difference	24.7	23.8	25.0	23.0	26.4	25.0	25.1	25.2

a)

b)

c)

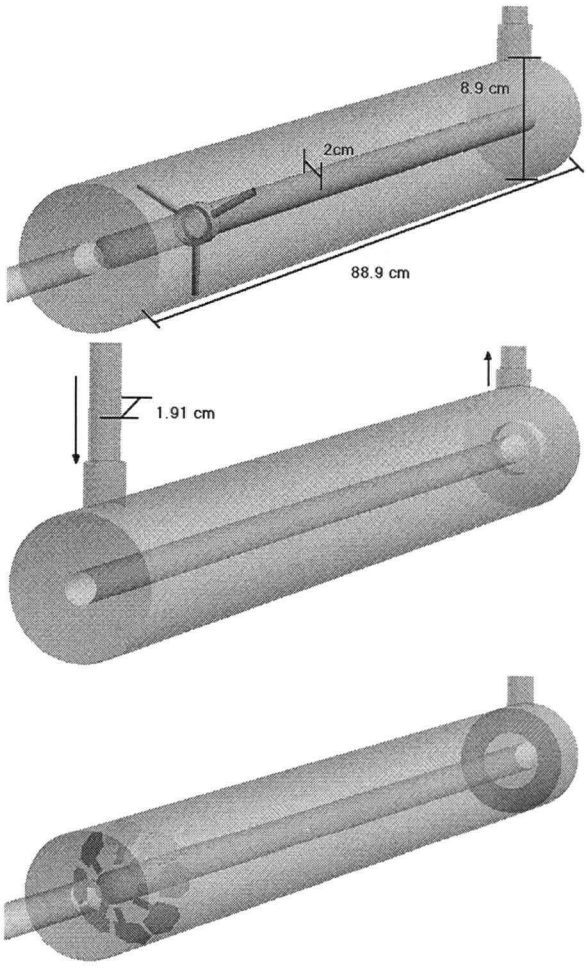

Figure 4.1: a) L-shape with lamp holder, b) U-shape, and c) Industrial prototype (L-shape with lamp holder) annular reactor geometries.

a)

b)

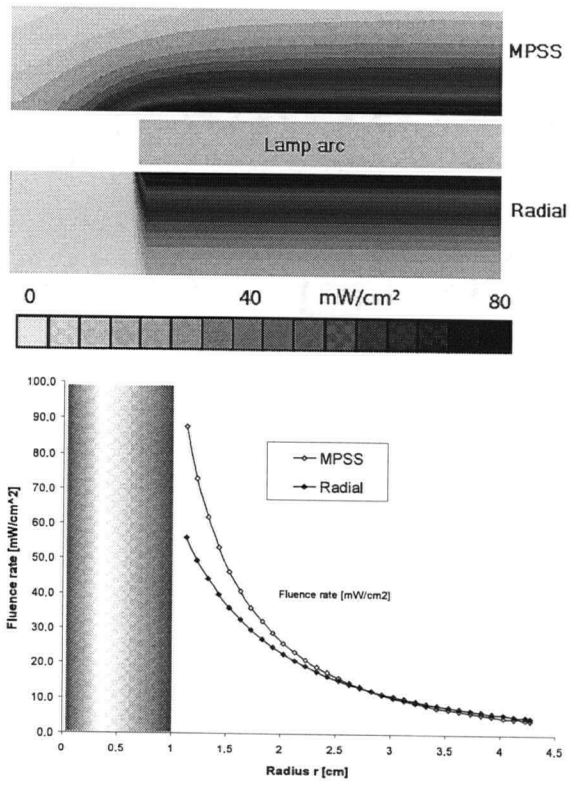

Figure 4.2: Fluence rates for the radial and MPSS radiation models at the centre of the lamp arc.

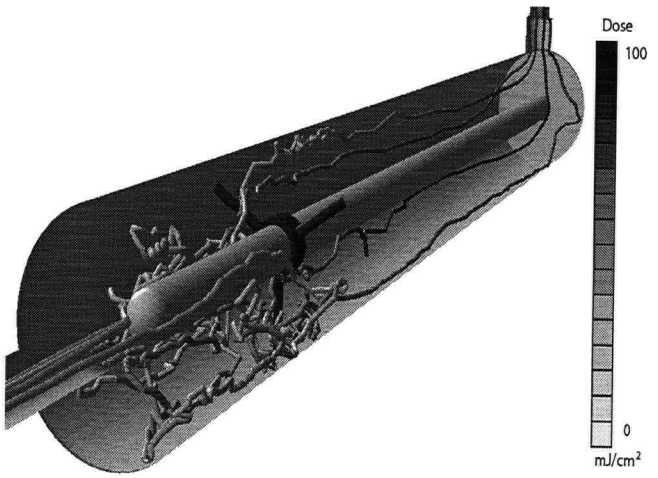

Figure 4.3: Lagrangian particles tracks in an L-shape reactor colored by absorbed Dose.

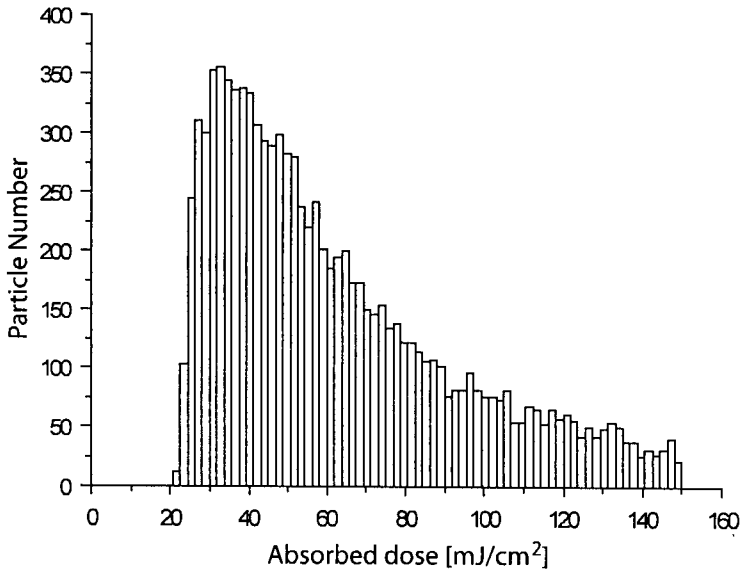

Figure 4.4: Lagrangian dose distribution, L-shape, 25 GPM with MPSS radiation model. The upper dose range was clipped at 150 mJ/cm^2 for better legibility, doses up to 270 mJ/cm^2 were reached infrequently.

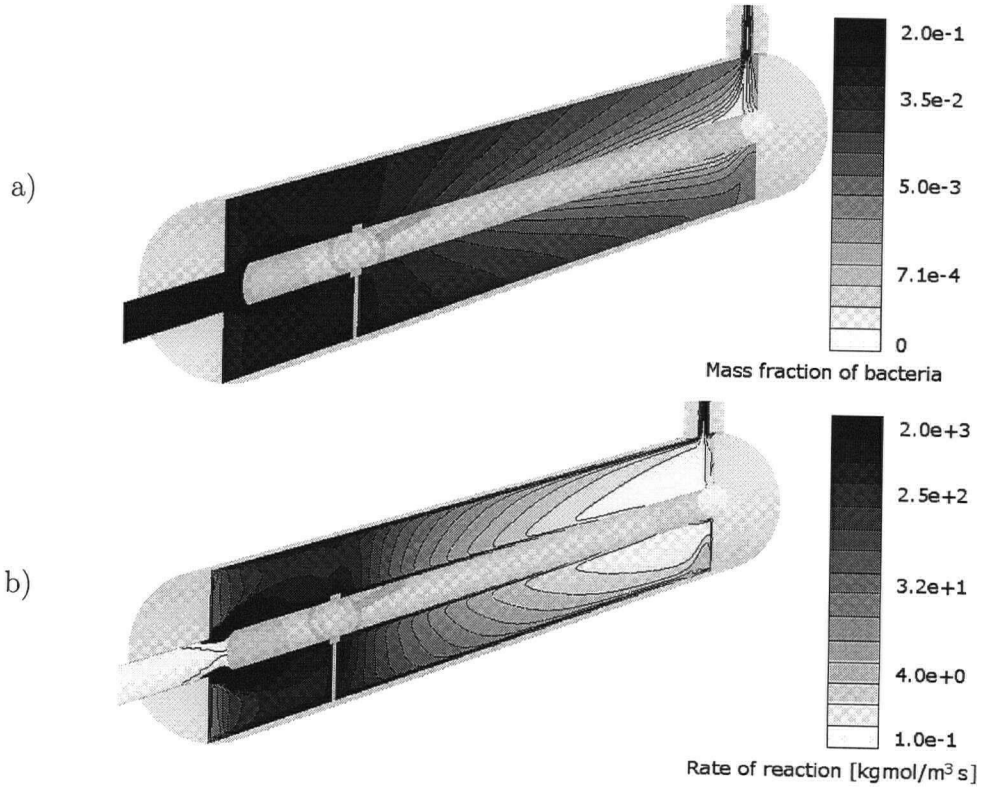

Figure 4.5: a) Contours of microorganism concentration, mass fraction on a log scale. b) Contours of disinfection reaction rates [kgmol/m^3s] on a log scale. L-shape, 25 GPM with MPSS lamp model.

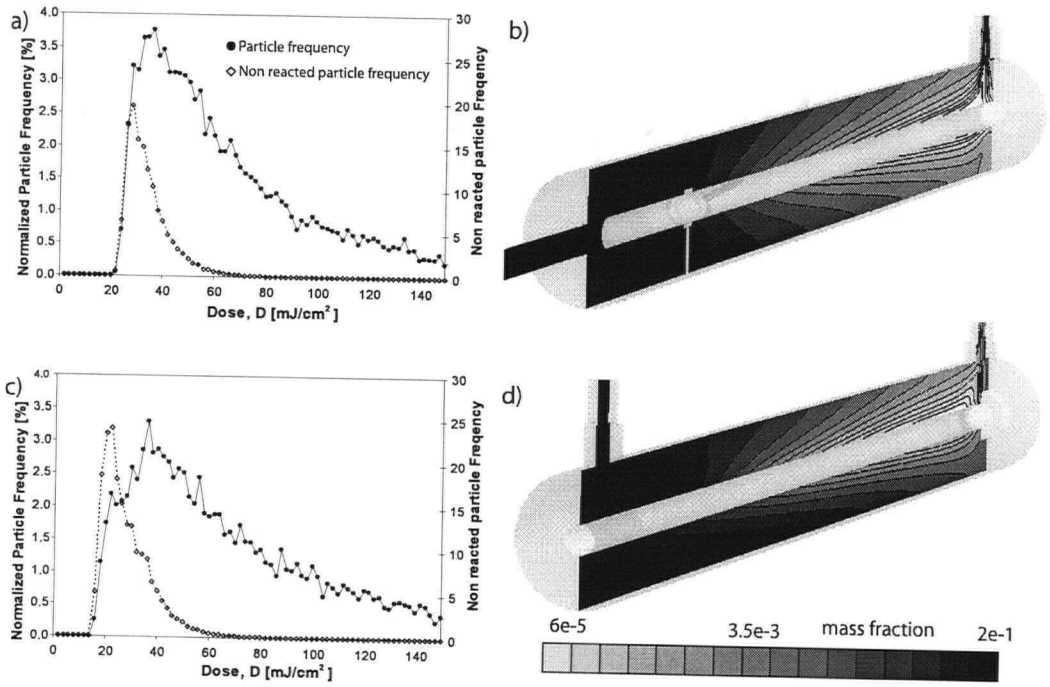

Figure 4.6: Lagrangian dose distribution (a,c) and Eulerian concentration distribution (b,d) for L- and U-shape reactor geometries. Range of Lagrangian results clipped at 150 mJ/cm^2 for better legibility

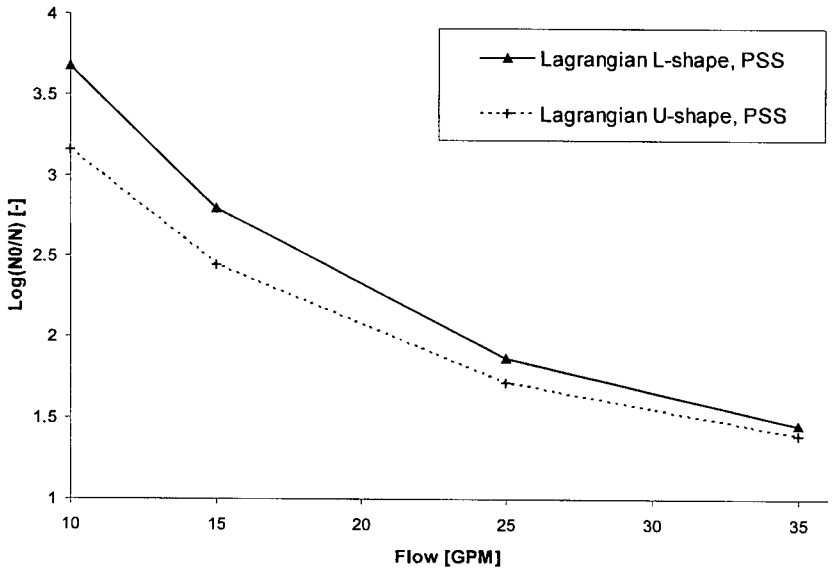

Figure 4.7: Log reduction in the L- and U-shape reactor geometries for different flow rates. Lagrangian approach with MPSS radiation at 70% UV-transmittance (per cm).

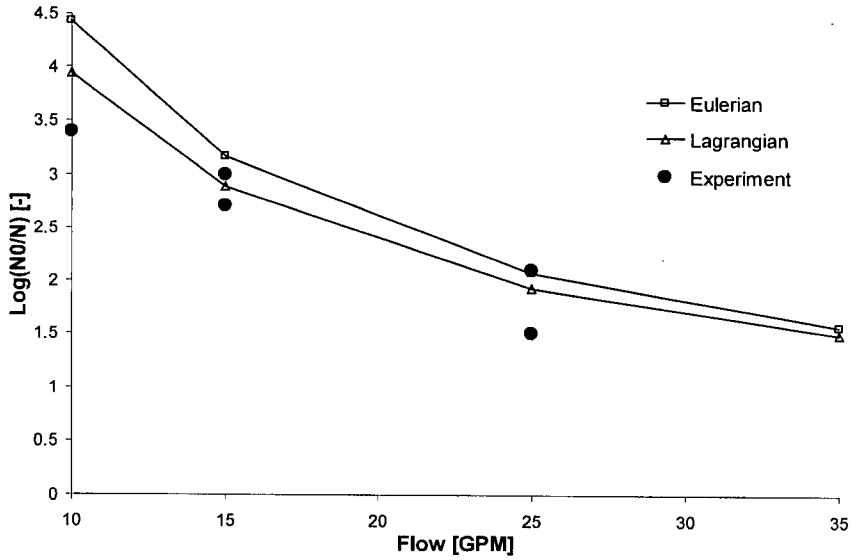

Figure 4.8: Eulerian and Lagrangian model results (MPSS radiation model with 70% UV-transmissivity) compared to experimental data over a range of flow rates for a commercial L-shape reactor.

Bibliography

[1] Bakker, A., Haidari, A. H., and Marshall, E. M. Design reactors via cfd. *CEP Magazine December* (2001), 30–39.

[2] Blatchley, E. R. Numerical modelling of uv intensity: Application to collimated-beam reactors and continuous-flow systems. *Water Research 31*, 9 (1997), 2205–2218.

[3] Bolton, J. R. Calculation of ultraviolet fluence rate distributions in an annular reactor: Significance of refraction and reflection. *Water Research 34*, 13 (2000), 3315–3324.

[4] Chiu, K., Lyn, D. A., and Blatchley, E. R. Integrated uv disinfection model based on particle tracking. *Journal of Environmental Engineering* (1999), 7–16.

[5] Fluent. *Fluent user guide: Chapter 13. Modeling species transport and finite-rate chemistry.* Fluent.inc, 2004.

[6] Fluent. *Fluent user guide: Chapter 19. Discreete phase models.* Fluent.inc, 2004.

[7] Kamimura, M., Furukawa, S., and Hirotsuji, J. Development of a simulator for ozone/uv reactor based on cfd analysis. *Water science and technology : a journal of the International Association on Water Pollution Research 46* (2002), 13–19.

[8] Liu, D., Ducoste, J., Jin, S., and Linden, K. Evaluation of alternative fluence rate distribution models. *Journal of Water Supply: Research and Technology-AQUA 53.6* (2004), 391–408.

[9] Lyn, D. A., Chiu, K., and Blatchley, E. R., I. Numerical modeling of flow and disinfection in uv disinfection channels. *Journal of Environmental Engineering (Reston, Virginia) 125* (1999), 17–26.

[10] MOFIDI, A. A., COFFEY, B. M., GREEN, J. F., AND CHOU, C. I. Investigation of ultraviolet light disinfection. Tech. rep., Metropolitan Water District of Southern California, 2002.

[11] MULKEY, L. A. Etv joint verification statement, uv disinfection of secondary effluent system by suntec inc. Tech. rep., US-Environmental Protection Agency, Envronmental Technology Verifcation Programm, 2003.

[12] PAREEK, V. K., COX, S. J., BRUNGS, M. P., YOUNG, B., AND ADESINA, A. A. Computational fluid dynamic (cfd) simulation of a pilot-scale annular bunbble column photocatalytic reactor. *Chemical Engineering Science 58* (2003), 859–865.

[13] PIRNIE, M., LINDEN, K. G., AND JAMES P. MALLEY, J. Ultraviolet disinfection guidance manual, draft epa 815-d-03-007. *USEPA* (2003).

[14] SCHEIBLE, O. K., AND MCGRATH, J. A. Generic verification protocol for high-rate, wet-weather flow disinfection applications. Tech. rep., US Environmental Protection Agency, 2000.

[15] SCHOENEN, D., KOLCH, A., AND GEBEL, J. Influence of geometrical parameters in different irradiation vessels on uv disinfection rate. *International Journal of Hygiene and Environmental Medicine 194*, 3 (1993), 313–320.

[16] TAGHIPOUR, F. Ultraviolet and ionizing radiation for microorganism inactivation. *Water Research 38*, 18 (2004), 3940–3948.

[17] UNLUTURK, S. K., H.ARASTOOPOUR, AND KOUTCHMA, T. Modeling of uv dose distribution in a thin-film uv reactor for processingof apple cider. *Journal of Food Engineering 65*, 1 (November 2004), 125–136.

[18] US-EPA. *USEPA Manual of methods for virology EPA 600/4-84/013 (N16)*, June 2001.

Chapter 5

Conclusions and recommendations

5.1 Conclusions

A detailed evaluation of the hydrodynamic flow in annular UV-reactors was performed for two characteristic reactor configurations, with inlets either concentric (L-shape) or normal (U-shape) to the main reactor axis. The flow structures on the vertical center plane were experimentally investigated employing particle image velocimetry (PIV) and numerically simulated using a commercial computational fluid dynamics (CFD) software package.

Time averaged PIV velocity field results revealed the prevailing characteristic flow structures for both reactor configurations. The results confirmed that changes in reactor geometry, both external (inlet position) and internal (lamp tip and holder), have a significant impact on the flow distribution. The inlet region of the L-shape reactor exhibited a typical and stable expanding jet behavior with zones of low velocity flow and flow recirculation. In the U-shape reactor, the flow separation around the central annulus introduced an unsteady flapping motion and the 90 degree change in directions resulted in a sustained asymmetric velocity profile with higher velocities along the lower wall, far from the central lamp. It was also shown that small lateral displacements or tilting of the inlet tube were sufficient to induce a swirling flow throughout the reactor domain. This instability was also reflected in the high mesh dependence and problematic convergence of the numerical solutions.

The reactor configuration was found to have a dominant effect on the highly

three-dimensional flow distribution in the inlet region. These effects attenuated and were no longer significant after approximately one-third of the U-shape and two-thirds of the L-shape reactor length. In the final third, the axial velocity profiles of both reactors were governed by the position of the outlet, and since this was the same for the two cases, the results cloesly matched one another

CFD simulations of the reactors used in the experiments were conducted and the mean velocity predictions were generally in a good agreement with the experimental values. Mesh independent solutions were achieved at mean cell volumes of 5×10^{-9} m^3 (0.5-1 million cells per reactor) when using structured cells. Of the three tested turbulence models, the Realizable κ-ϵ model showed the best overall agreement with the experimental data and was consequently employed for further investigations. The Standard κ-ϵ turbulence model did not perform well in regions with high velocity gradients such as in the inlet jet. The RSM model showed very good agreement with PIV data, except in regions with unstructured mesh and with time dependent flow phenomena (e.g. downstream of the lamp-holder). High computational costs and mesh dependency problems made the use or RSM unfavorable under the given technical constraints.

Disinfection performance of an industrial UV-reactor was successfully simulated by integrating UV-fluence rate and inactivation kinetics with the CFD hydrodynamic flow predictions, using MS2 bacteriophages as a model organism. While the Lagrangian random walk model provided the statistical dose distribution and particle tracks to visualize flow patterns, the Eulerian model, using a combination of species transport and volumetric reaction modeling, showed the concentration distribution and local inactivation rates.

MS2 inactivation results predicted by the two integrated approaches were found to be in good agreement with each other, yielding deviations of 4-11% for the tested range of flow rates (10-35 GPM). Results matched the biodosimetry findings well, considering that errors of 20% or more are standardly encountered for biological assays. The results were highly influenced by the choice of radiation model (radial or MPSS), where a consistent difference of about 26% was found. For the current situation, the MPSS model showed an overall better fit, but not enough experimental data were available for a conclusive judgment.

Reactor performance levels under identical simulation conditions were 5-14% lower for the U-shape configuration, when compared to the L-shape. The poorer performance of the former suggests that some short circuiting takes place, confirming the observed differences of the flow profiles. While numerical models provide detailed information on the velocity profiles, reaction rates, and areas of possible short circuiting within UV-reactors, complimentary experiments remain necessary to validate the accuracy of the results.

5.2 Recommendations

From the current study, it was not clear to what extent the final performance results were affected by each model component. A detailed parametric study of the influence of hydrodynamic flow, UV-radiation, and reaction kinetics would help to determine the emphasis of future model development.

Verification of CFD results based on one-dimensional quantitative and two-dimensional qualitative comparisons of the velocity data was successful. However, a quantitative comparison of the full two-dimensional flow field information would make much better use of the available velocity magnitude information from PIV. Such a detailed comparison would likely be a powerful tool to determine problematic areas with high deviations while also providing a more rigorous validation.

The Eulerian disinfection model predictions could be validated by PLIF (planar laser induced fluorescence) measurements. PLIF provides quantitative, instant concentration field data, giving access to the characterization of concentration fluctuations and mixing features in liquids. The setup is closely related to PIV and additional data could be gathered with the same equipment. This would allow the quality of the species transport based kinetic model to be assessed.

While the Realizable κ-ϵ turbulence model predicted the experimental velocity profiles reasonably well, the initial results from the RSM model were also very promising, considering the computational restrictions. Higher mesh densities in the area of the lamp holder should be explored to determine if the observed deviations can be eliminated. The RSM model may well prove to be the most versatile turbulence modeling approach.

Though verification of the hydrodynamic flow was established, the two UV-radiation models tested gave significantly different values. Hence, further investigations should be performed in order to evaluate the accuracy of the UV fluence distributions obtained using different radiation models.

With a verified integrated CFD reactor model, the possibilities for virtual reactor performance optimizations are nearly unlimited. Studies of different reactor sizes and geometries, including mixers, distributed inlet jets, Taylor-Couette or swirling flows, and the use of multiple lamps would significantly improve the current understanding of UV based reactor systems.

Appendix A

Specifications of the experimental setup

A.1 PIV setup

The PIV setup consists of a laser system providing a high intensity light sheet, a CCD camera capturing the illuminated particles and a hub to synchronize laser and camera action. A high speed frame grabber with a Last In First Out (LIFO) memory buffers and transfers the images to the processing computer.

The experimental test section is immersed in a fluid to compensate for optical distortion and the complete setup is placed on a sturdy table for best result.

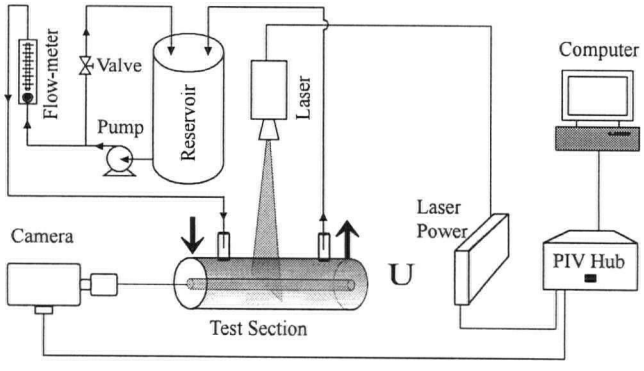

Figure A.1: PIV Setup

A.1.1 PIV camera

The HiSense camera is used in a number of applications; In PIV with large target areas and low light intensity; Planar laser-induced fluorescence experiments; Supersonic flows, with time separation down to 0.2 micro sec; Flame front measurements (gating option), and in any situation in which high light sensitivity and quality data are important. The camera uses a high-performance progressive scan interlines CCD chip. This chip includes 1280 by 1024 light-sensitive cells and an equal number of storage cells.

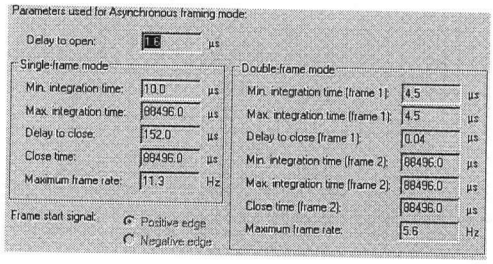

Figure A.2: Camera parameter

Make:	Hamamatsu C8484
Model:	C8484-05CP
Name:	HiSenseMkII
Serial:	710042
Resolution:	1023×1343 (H×W)
Pixelsize:	$6.45\mu m \times 6.45\mu m$
Framerate:	11Hz single, 5Hz double

Table A.1: PIV camera specifications

A.1.2 Camera lens

The camera lens images the target area onto the CCD array of a digital camera. A 514nm filter can be used with this lens to reduce the influence of ambient light. At a distance of 1m the lens focused on an area of 8×11cm with no barrel distortion.

Figure A.3: Lens

Make:	Nikon
Model:	AF Micro-Nikkor
Name:	60mm f/2.8D
MinFoc:	8.75 inch
MaxRep:	1:1 (Macro))
Size:	2.8×2.9inch (Diam.
Filter:	Dantec 514nm

Table A.2: PIV lens specifications

A.1.3 Laser

Solo PIV is a compact, dual laser-head system designed to provide a highly stable green light source for Particle Image Velocimetry (PIV) applications. It is ideally suited for most liquid and many air-based PIV experiments, and its small size provides excellent flexibility in setting-up such experiments.

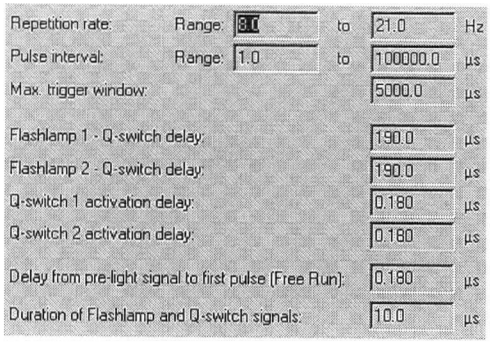

Figure A.4: Laser parameters

Make:	New Wave Research
Model:	Solo III 15Hz
Name:	SoloPIV 532nm Nd:YAG
Energy:	50mJ (532nm Green)
Stability:	±4% pulse to pulse
Pulse width:	3-5ns
Beam Div.:	<4 mrad
Diameter:	3.5mm
Jitter	±0.5ns

Table A.3: PIV laser specifications

A.1.4 Seeding

The seeding should be highly reflective and of the same density as the observed media. Polyamid seeding particles are produced by polymerization and therefore round but not exactly spherical. These microporous particles are highly recommended for water flow applications.

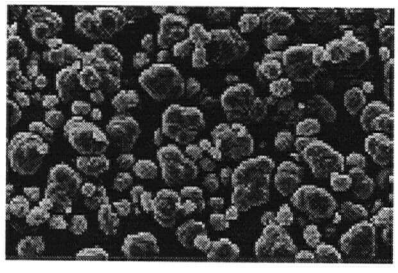

Figure A.5: PSP particles

Make:	Dantec Dynamics
Name:	PSP, Polyamid Seeding Particles
Mean Size:	$20\mu m$
Distribution:	5-35 μm
Shape:	Spherical but not round
Density:	1.03 $\frac{g}{cm^3}$
MeltingPt:	175 $^{\circ}C$
Refr. Index	1.5
Material	Polyamid 12

Table A.4: Seeding specification

A.1.5 System hub

The system hub is the central control system of the PIV setup. It is controlled asynchronously from a PC running Dantecs FlowMap software. Once a measuring sequence is programmed, the hub acts autononomously, synchronizing camera and laser and buffering the captured images. The captured data is then streamed to the controlling PC for analysis. The hub runs completely independent from the controlling PC for the duration of the measurements and the LIFO memory can buffer up to 200 measurements (double exposures) of roughly 5MB at a dynamic gray scale range of 12bit.

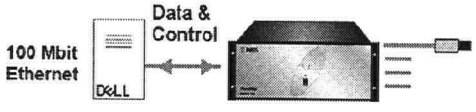

Figure A.6: PIV hub

Make:	Dantec Dynamics
Name:	Flowmap System Hub
Software:	Flowmap System HUB V4.01
LIFO RAM:	1.0GB (200 measurements)
Network	100MBit

Table A.5: Hub specifications

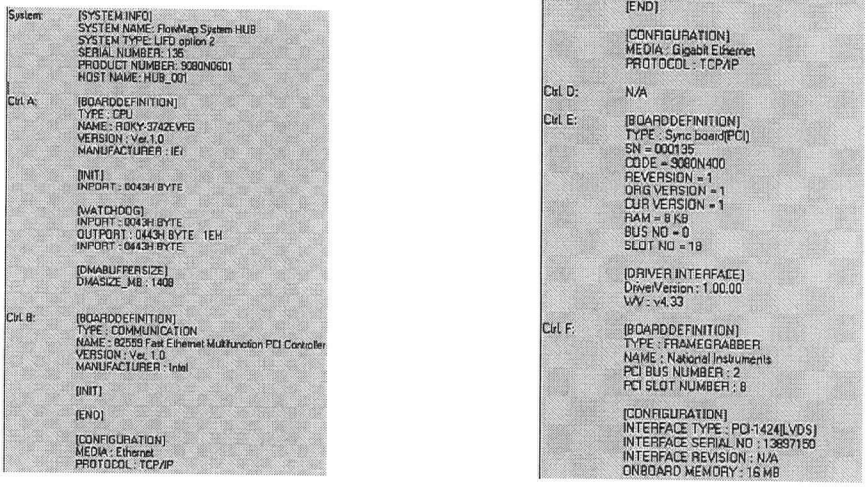

Figure A.7: Hub system info

A.1.6 PIV table

Camera and laser sheet should remain perpendicular to each other at all times for best results. Measurement with free standing camera and Laser were conducted but resulted in inferior data. An aluminum extrusion table was constructed with three free movable xy-planes (two on each side of the table and one above). The two outer planes are foldable and can be moved along the z-axis. The table can be leveled (feet are threaded) and the central table plate is subdivided into three sections, allowing for access from below.

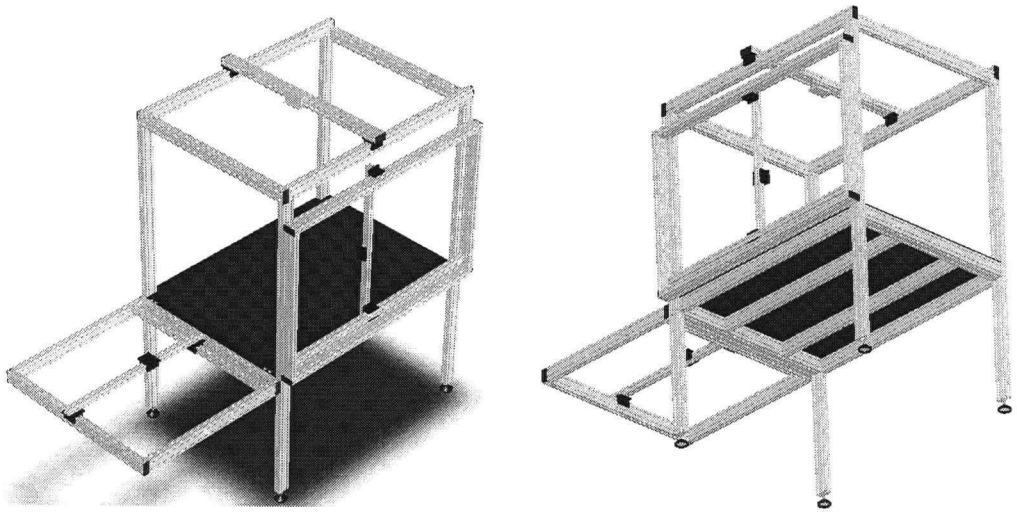

Figure A.8: PIV table

A.1.7 Fluid and aquarium

The fluid used in all components was distilled water at room temperature. Sodium Azide (Na-Azide) was added at a concentration of 0.5% $\frac{w}{v}$ to minimize algae growth.

A.1.8 Refractive index matching

PIV relies on the evaluation of visible data and distortion during measurements introduces a bias into the raw data. Post treatment during image analysis is possible;

however, it is not a straight forward process and should be avoided. Distortion occurs when light passes through non planar materials (such as cylindrical reactors) of different refractive indices. Ideally, the camera would face a flat reactor surface perpendicular to the laser sheet. The reactor was placed in a rectangular box filled with a refractive index matched fluid, thus creating a 'virtual' flat surface reducing the distortion. While a mixture of oils could fully match the refractive index of Plexiglas (Table A.6) the difference in viscosity made it impractical. Distilled water was used instead, tests showing it to adequately minimize the distortion to negligible levels. Images of a ruler immersed in the center of the reactor were used to quantify the distortion levels for several conditions; inner and outer volumes filled with air, water and glycerin respectively (Figure A.10). Glycerin in both volumes resulted in near perfect images. With distilled water, distortion perpendicular to the reactor axis was negligible up to $\approx$ 0.4 cm to the walls, where the image was compressed by 5-10%. Distortion along the cylinder axis was negligible, with no changes in the wall thickness and/or angle occuring. Distortion resulting from the cameras angle of view was minimized by placing it about 1m from the plane of measurement. s (Table A.6) the difference in viscosity made it impractical. Distilled water was used instead, tests showing it to adequately minimize the distortion to negligible levels. Images of a ruler immersed in the center of the reactor were used to quantify the distortion levels for several conditions; inner and outer volumes filled with air, water and glycerin respectively (Figure A.10). Glycerin in both volumes resulted in near perfect images. With distilled water, distortion perpendicular to the reactor axis was negligible up to $\approx$ 0.4 cm to the walls, where the image was compressed by 5-10%. Distortion along the cylinder axis was negligible, with no changes in the wall thickness and/or angle occuring. Distortion resulting from the cameras angle of view was minimized by placing it about 1m from the plane of measurement.

Material	refractive Index
Plexiglas	1.49
Glycerin (100%)	1.47
Distilled Water	1.33
Air	1.00

Table A.6: Refractive indices

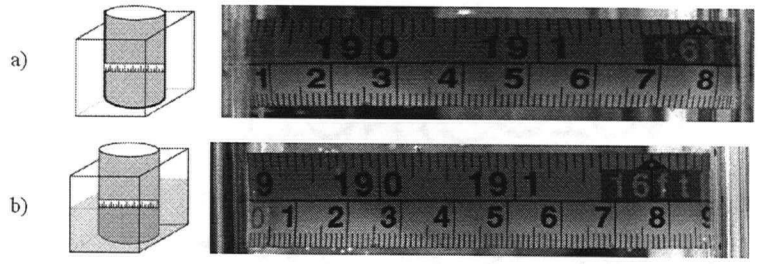

Figure A.9: Image distortion from the round reactor wall. a) The ruler is submerged in water within the cylindrical reactor body resulting in high distortion. b) Outer aquarium also filled with water reducing the optical distortion.

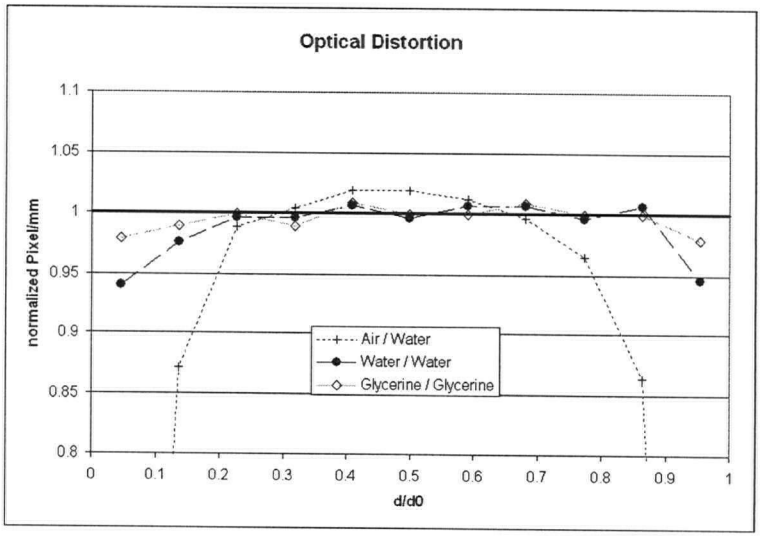

Figure A.10: PIV image distortion from the round reactor wall. Different conditions(fluid in reactor/fluid in box) are shown: Water/Water shows close to ideal image conditions.

Appendix B

Programs

The following listing are the programs and macros written to extend the capabilities of Fluent as needed for the thesis objectives or to simplify the handling of large amounts of data.

B.1 UV-radiation UDFs

The UV-radiation models were written and implemented in the C programming language and linked to Fluent as user defined functions (UDFs). The two following files represent the radial and the MPSS radiation models used. While both UDFs can be run as an interpreted programs, a user defined memory (UDM) space has to be allocated beforehand. (Define - User Defined - Memory ==> set to 1). Fluent has a bug that does not allocate the UDM space immediately, plotting the contours of the UDM will solve this.

Both radiation models were designed to handle multiple lamps. Each lamp is defined by the x,y,z coordinates of its start and endpoints that are hard coded within the UDF. The units used are cm and the program will automatically converts all values to the proper SI units. There is no security checks to verify if lamp coordinates are within the reactor space. For the case of multiple lamps, the local fluence rates are accumulated within each cell.

Shadowing effects have not been included and radiation calculations rely solely on the distance information of each cell centroid. Therefore, radiation calculations do not stop at the boundaries and care has to be taken with reactor shapes that

fold back on themselves.

All radiation models do not rely on any further definitions within Fluent. Lamps can therefore be defined anywhere withing the domain without a three dimensional model counterpart. This can be used to quickly test lamp positions without re-meshing the geometry. But calculations will only give a trend since neither the hydrodynamic influence of the lamp body nor kinetics within the lamp volume are correctly defined.

B.1.1 Radial model

The radial model calculates radiation as a function of the distance to the lamp. The radiation is only calculated within a virtual cylinder around the lamp vector defined by start and endpoints. To ensure full three dimensional compatibility, each cell centroid has to be checked if it is within the virtual cylinder. Simple checks only along the primary axes can lead to severe distortions (Figure B.1a) at either lamp end. A fully three dimensional collision check (Figure B.1b) ensures correct boundaries even for lamps not parallel to the coordinate system.

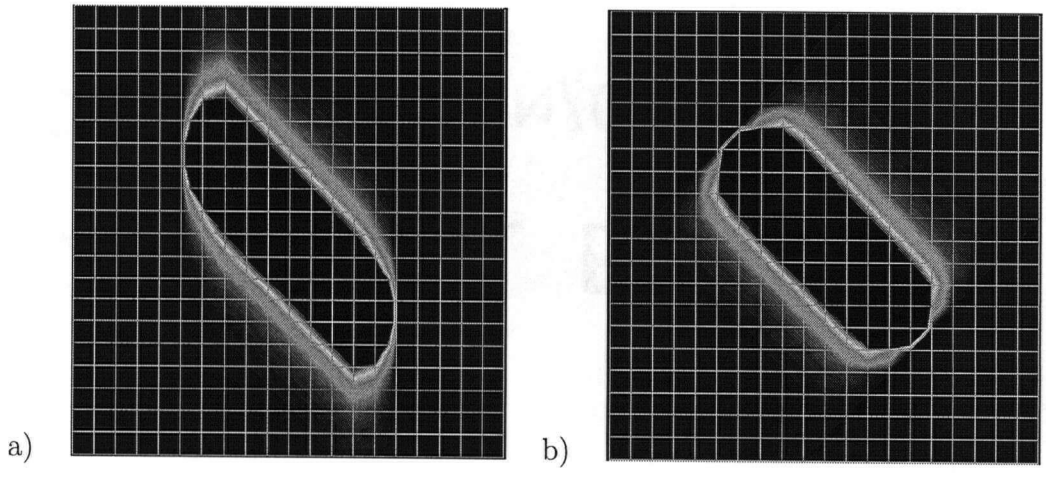

Figure B.1: Demonstration of non aligned lamp radiation a) without and b)with virtual cylinder collision detection.

```
**************************************************************************/
/*  Author:    Angelo Sozzi  angelo@sozzi.ch
/*  Date:      March 22 2004
/*  Package:   Fluent 6.1.18
/*  Platform:  Windows 2000
```

```
/*  Type:     UDF <interpreted>
/*  Tested on File   "March/oldRound1_1/fixedtest5_chem.cas"
/*
/*  Purpose: This function initializes the UDS in a given Zone to a given
/*   function of radius r.
/*   Note that the THREAD_ID parameter is the integer value shown as ID
/*   by in the Boundary Conditions Menu.
/*
/*  Usage:   Free memory space by:
/*           Solver -> Initialize Initialize to see the results show contours
/*
/* Started:   23-03-2004
/*
/* Revisions:
/* 25-08-2004
/* 09-07-2004 Remake now lamps can be placed in any direction
/* 21-05-2004 Working multi lamp adaption, lamps must be on axis
/* 19-05-2004 Adapted for more than one lamp 2D Array errors in Fluent !
/* 26-03-2004 Adapted for round reactor with main direction of pos Y
/* 23-03-2004 Changed to use any given lamp angle
/* 22-03-2004 (i) First working compilation
/*
/*
/*************************************************************************/
#include "udf.h"
#define V_CROSS(a,b,r)\
   ((r)[0] = (a)[1]*(b)[2] - (b)[1]*(a)[2],\
   (r)[1] = (a)[2]*(b)[0] - (b)[2]*(a)[0],\
   (r)[2] = (a)[0]*(b)[1] - (b)[0]*(a)[1])

/********** Some constants used ******************************************/
const int thread_id=2;   /* Specify the ID number here (2=fluid)          */
real pii  = M_PI;        /* Define Pi                                     */
real Trans= 0.7;         /* Transmittance of Water 1/cm  0.7=70%          */
real Alfa = 1;           /* Alfa 1/cm                                     */
/********** Lamp Specifications inserted here ****************************/
/* Specify the number of lamps you intend to use                          */
#define NRLAMPS 1
#define ON 1
#define OFF 0
/* lampdata for each lamp is passed as follows:
    x,y,z,     X,Y,Z, radius, Izero, SleveIndex
/*             Lamp / 1 /  2 /  3 /  4 /  5 etc.                          */
real Xst[NRLAMPS]=   {    0};   /* X coordinates Startpoints  [cm]        */
real Yst[NRLAMPS]=   {    0};   /* Y coordinates              [cm]        */
real Zst[NRLAMPS]=   { 4.45};   /* Z coordinates              [cm]        */
real Xnd[NRLAMPS]= {    0};     /* X coordinates Endpoints    [cm]        */
real Ynd[NRLAMPS]= {    0};     /* Y coordinates              [cm]        */
real Znd[NRLAMPS]= {84.45};     /* Z coordinates              [cm]        */
real r[NRLAMPS]=      { 1.0 };  /* Radius lamp sleve          [cm]        */
real Izero[NRLAMPS]={0.4375};   /* Lamp output per length     [W/cm]      */
real SLndx[NRLAMPS]={    1};    /* Sleve index of lamp        [-]         */
int  OnOff[NRLAMPS]={   ON};    /* Lamp State ON or OFF       [-]         */
/********** Variable declarations for macro ******************************/
int lamp;            /* Lamp which is currently looped over in macro      */
real lampStart[3];
real lampEnd[3];
real lampVec[3];    /* Variable to store the lamp vectors                 */
real PointVec[3];   /* To store the current cell (location)vector         */
real ptlampVec[3];  /* Store the vector from LampStart to Point           */
real KreuzProd[3];  /* To store the Cross Product (normal) vector         */
real dot;           /* Dot product                                        */
real lengthsq;      /* Square of the cylinder length ( vector magnitude)  */
int i;              /* just a counter variable                            */
real distanz;       /* store the distance of the cell to the lamp         */
real sumtop;        /* Store denominator sum                              */
real sumbottom;     /* Store nominator sum                                */
```

```
/********** Fluent on demand macro ****************************************/
DEFINE_ON_DEMAND(init_UDS_radius_multiV1_1)
{
  Domain *d;       /* Init Domain pointer                                  */
  Thread *t;       /* Init Thread pointer                                  */
  cell_t c;        /* Init Cell variable                                   */
  real xc[ND_ND];  /* Init xc with ND_ND=2 for 2D and 3 for 3D Fluent solver*/
  d = Get_Domain(1);               /* Get the specified domain            */
  t = Lookup_Thread(d, thread_id); /* Use only the selected Thread        */

  /* Loop over all the cells in the given thread                          */
  begin_c_loop (c,t)
  {
    C_CENTROID(xc,c,t);   /* Read the values of the centroid in SI units [m]! Point in space to calculate the distance to lamp 1 */
    for (i=0; i<3; i++)
      xc[i]=xc[i]*100;    /* convert Cell coordinates to cm               */
    C_UDMI(c,t,0) = 0;    /* Delete previous values, since we will add up values further down */

    for (lamp=0;lamp<NRLAMPS;lamp++)    /* loop through lamps             */
        {
/* calc values for each lamp as needed */
    lampStart[0]= Xst[lamp]; lampStart[1]= Yst[lamp]; lampStart[2]= Zst[lamp]; /* Read X,Y,Z of Startpoint into a vector */
    lampEnd[0]  = Xnd[lamp]; lampEnd[1]  = Ynd[lamp]; lampEnd[2]  = Znd[lamp]; /* Read X,Y,Z of Endpoint into a vector   */

    NV_VV(lampVec, =, lampEnd, -, lampStart);   /* Calculate the lamp vector Endpoint-Startpoint  */
    NV_VV(ptlampVec, =, xc, -, lampStart);      /* Vector from Cylinder Start to test point       */
    dot = NV_DOT(ptlampVec,lampVec);            /* Dot the lampVector and Point to StartLamp Vector to see if point lies behind cylinderd cap */
    lengthsq = NV_MAG2(lampVec);                /* Square of the cylinder length                  */
      if ((dot>0.0f) && (dot < lengthsq) && (OnOff[lamp]==ON)) /*check if inside lamp length 0=x 1=y 2=z                */
      {
        NV_VV(PointVec,=,xc,-,lampStart);             /* PointVector = Point-lampStart*/
        V_CROSS(lampVec,PointVec,KreuzProd);          /* Cross product of vector see top for def.                      */
        distanz = NV_MAG(KreuzProd)/NV_MAG(lampVec);  /* NV_MAG computes magnitude of a vector square root of the summ of square of vector components */

       //C_UDMI(c,t,0) = C_UDMI(c,t,0)+(Sleeve*     Izero* (pow(Trans,(Alfa*(distanz-SleeveRad)))))/(2*pii*distanz);
        C_UDMI(c,t,0) = C_UDMI(c,t,0)+(SLndx[lamp]*Izero[lamp]*(pow(Trans,(Alfa*(distanz-r[lamp])))))/(2*pii*distanz);
      }

          }  /* End loop through lamps */
  }
  end_c_loop (c,t)
}
```

B.1.2 MPSS radiation model

For the MPSS model, each lamp is subdivided into multiple point sources. The number of sources can be chosen freely, but calculation times get longer with each additional point. 100 point should provide sufficient accuracy for lamps of 1m or less. Since this radiation model relies on the distance of each cell centroid to the lamp vector and each source, radiation beyond the lamp tip is also accounted for. There is no longer a need to check the lamp boundaries as this is implicitly given.

```
/*****************************************************************************/
/*  Author:   Angelo Sozzi  angelo@sozzi.ch
/*  Date:     March 22 2004
/*  Package:  Fluent 6.1.18
/*  Platform: Windows 2000
/*  Type:     UDF <interpreted>
```

```
/*  Tested on File   "C:/CFD/Cube_test/20/"
/*
/*  Purpose: This function initializes the UDS in a given Zone to a given
/*   function of radius r.
/*   Note that the THREAD_ID parameter is the integer value shown as ID
/*   by in the Boundary Conditions Menu.
/*
/*  Usage:   Free memory space by:
/*   In the Solver -> Initialize Intialize to see the results show contours
/*
/* Started:   23-03-2004
/*
/* Revisions:
/*13-12-2004 Modified to eliminate divide by zero inf error (if distanz>r loop)
/* 23-09-2004 This is the PSS Model now
/* 09-07-2004 Remeake now lamps can be placed in any direction
/* 21-05-2004 Working multilamp adaption, lamps must be on axis
/* 19-05-2004 Adapted for more than one lamp 2D Array errors in Fluent !
/* 26-03-2004 Adapted for round reactor with main direction of pos Y
/* 23-03-2004 Changed to use any given lamp angle
/* 22-03-2004 (i) First working compilation
/*
/*
/*************************************************************************/
#include "udf.h"
#define V_CROSS(a,b,r)\
  ((r)[0] = (a)[1]*(b)[2] - (b)[1]*(a)[2],\
   (r)[1] = (a)[2]*(b)[0] - (b)[2]*(a)[0],\
   (r)[2] = (a)[0]*(b)[1] - (b)[0]*(a)[1])

/********** Some constants used ******************************************/
const int thread_id=2;   /* Specify the ID number here (2=fluid)      */
real pii  = M_PI;        /* Define Pi                                 */
real Trans= 0.7;         /* Transmittance of Water 1/cm  0.7=70%      */
real Alfa = 1;           /* Alfa 1/cm                                 */
real NrPts= 100;          /* Number of points that the lamp will be discretized to */
/********** Lamp Specifications inserted here ****************************/
#define NRLAMPS 1
#define ON 1
#define OFF 0
/* Specify the number of lamps you intend to use */
/* lampdata for each lamp is passed  in rows as follows:
    start x,y,z,    end X,Y,Z, radius, Izero, SleveIndex

/*            Lamp { 1 ,  2 ,  3 ,  4 ,  5 etc.}                     */
real Xst[NRLAMPS]=  {     0};     /* X coordinates Startpoints    [cm]  */
real Yst[NRLAMPS]=  {     0};      /* Y coordinates  "            [cm]  */
real Zst[NRLAMPS]=  {  4.45};      /* Z coordinates  "            [cm]  */
real Xnd[NRLAMPS]=  {     0};      /* X coordinates Endpoints     [cm]  */
real Ynd[NRLAMPS]=  {     0};      /* Y coordinates  "            [cm]  */
real Znd[NRLAMPS]=  { 84.45};      /* Z coordinates  "            [cm]  */
real r[NRLAMPS]=    {   1.0};      /* Radius lamp sleve           [cm]  */
real Izero[NRLAMPS]={0.4375};      /* Lamp output per LampLength  [W/cm]*/
real SLndx[NRLAMPS]={     1};      /* Sleve index of lamp         [-]   */
int  OnOff[NRLAMPS]={    ON};     /* Lamp State ON or OFF         [-]   */

/********** Variable declarations for macro ****************************/
int lamp;            /* Lamp which is currently looped over in macro  */
real lampStart[3];
real lampEnd[3];
real lampVec[3];     /* Variable to store the lamp vectors           */
real PointVec[3];    /* To store the current cell (location)vector   */
real ptlampVec[3];   /* Store the vector from LampStart to Point     */
real KreuzProd[3];   /* To store the Cross Product (normal) vector   */
real lampPt[3];      /* Store the coordinats of a point on the lamp  */
real lampUnit[3];    /* Store the lamp unit vector                   */
real addVector[3];   /* Vector to be added to Start for point pos    */
real PtPtVector[3];  /* The Point to Point Vector                    */
```

```
real abstand;        /* Distance from Point on Lamp to Cell          */
real Ifull;          /* UV lamp Power output of the whole lamp [W]   */
real dot;            /* Dot product                                  */
real LampLength;     /* Lamp cylinder LampLength (magnitude)         */
real parameter;      /* Lamp Unit multiplicator variable             */
real lamda;          /* as above but in the lamp loop                */
real k;              /* The Absorbtion coefficient [1/cm]            */
int i;               /* just a counter variable                      */
int points;          /* counter to go through points                 */
real distanz;        /* store the distance of the cell to the lamp   */
real sumtop;         /* Store denominator summ                       */
real sumbottom;      /* Store nominator summ                         */
real summup;         /* summ of values from each point               */
int flag=0;
/*********** Fluent on demand macro ************************************/

DEFINE_ON_DEMAND(init_UDS_radius_multiV3_1)
{
  Domain *d;         /* Init Domain pointer   */
  Thread *t;         /* Init Thread pointer   */
  cell_t c;          /* Init Cell variable    */
  real xc[ND_ND];    /* Init xc with ND_ND=2 for 2D and 3 for 3D Fluent solver */
  d = Get_Domain(1);                /* Get the specified domain              */
  t = Lookup_Thread(d, thread_id);  /* Use only the selected Thread          */
  k  =  -log(10)*log10(Trans);      /* Calculate k from T                    */

/* Loop over all the cells in the given thread                               */
  begin_c_loop (c,t)
  {
    C_CENTROID(xc,c,t);    /* Read the values of the centroid in SI units [m]! Point in space to calculate the distance to lamp 1 use */
    for (i=0; i<3; i++)
      xc[i]=xc[i]*100;     /* convert Cell coordinates to cm                */
    C_UDMI(c,t,0) = 0;     /* Delete previous values, since we will add up values further down */

    for (lamp=0;lamp<NRLAMPS;lamp++)    /* loop through lamps               */
    {
        /* calc values for each lamp as needed */
      lampStart[0]= Xst[lamp]; lampStart[1]= Yst[lamp]; lampStart[2]= Zst[lamp]; /* Read X,Y,Z of Startpoint into a vector */
      lampEnd[0]  = Xnd[lamp]; lampEnd[1]  = Ynd[lamp]; lampEnd[2]  = Znd[lamp]; /* Read X,Y,Z of Endpoint into a vector   */

      NV_VV(lampVec, =, lampEnd, -, lampStart);     /* Calculate the lamp vector Endpoint-Startpoint  */
      NV_VV(ptlampVec, =, xc, -, lampStart);        /* Vector from Lamp Cylinder Start to test point    */
      LampLength = NV_MAG(lampVec);                 /* Lamp cylinder LampLength */
      Ifull  = Izero[lamp]*LampLength;              /* Calculate the full lamp output in [W] from the Output per lentgh [W/cm]  */
      V_CROSS(lampVec,ptlampVec,KreuzProd);         /* Cross product of vector see top for def. */
       distanz = NV_MAG(KreuzProd)/LampLength;      /* NV_MAG computes magnitude of a vector square root of the summ of square of vector components */
      lampUnit[0]=lampVec[0]/LampLength; lampUnit[1]=lampVec[1]/LampLength; lampUnit[2]=lampVec[2]/LampLength; /* Calculate the Lamp Unit vector */

      parameter = LampLength/NrPts;                 /* LamUnit multiplicator */
      summup    = 0;                                /* Initialize the summup for each lamp */

      if (distanz> r[lamp]){
      for (points=0;points<NrPts;points++)          /* Loop through discretized points on lamp */
      {
        lamda = parameter*points;                   /* Calculate the Parameter to multiply the LampUnit Vector by */
        addVector[0]=lampUnit[0]*lamda; addVector[1]=lampUnit[1]*lamda; addVector[2]=lampUnit[2]*lamda; /* Multiply */
        NV_VV(lampPt, =, lampStart, +, addVector);  /* Finally Calculate the X,Y,Z of the point on the Lamp */
        NV_VV(PtPtVector, =, xc, -, lampPt);        /* Vector from Cell to point on Lamp */
        abstand = NV_MAG(PtPtVector);               /* Distance from Point to CellCentre */

      summup = summup+((Ifull/NrPts)/(4*pii*abstand*abstand)*exp(-k*(distanz-r[lamp])));
      }    /* End loop through points on lamp */
      C_UDMI(c,t,0) = C_UDMI(c,t,0)+summup;
      } /*End the if statement*/
    }       /* End loop through lamps */
  }         /* End loop through Cells in Thread */
  end_c_loop (c,t)
}          /* End On Demand Macro */
```

B.2 Lagrangian disinfection model

The Lagrangian model relies heavily on the Fluent discrete phase model (DPM) environment. The DPM environment has to be set up as described in the manual for particle tracking, before employing the Lagrangian model. An additional user variable and the UV-radiation model are also needed. The dose-setup function redefines the DPM user scalar name. The absorbed-dose function has to be hooked to the DPM-UDF environment and calculates the dose absorbed along the path of each particle. The dose-output function finally redefines the Report-DPM-Sample-output menu to output the absorbed dose values into an external file.

```
/************************************************************************/
/*  Author:    Angelo Sozzi  angelo@sozzi.ch
/*  Date:      April 07 2004
/*  Package:   Fluent 6.1.18
/*  Platform:  Windows 2000
/*  Type:      UDF <interpreted>
/*  Tested on File   "March/oldRoundi_1/fixedtest5_chem.cas"
/*
/*  Purpose: This function Integrates the Dose of a particle injected by
/*           Particle tracking. See 4-150 UDF manual.
/*
/*
/*
/*  Usage:   Interpret, and hook the UDF to Init. Open a UDS.
/*   In the Solve -> Initialize Intialize to see the results show contours
/*
/* Started:   23-03-2004
/*
/* Revisions:
/* 12-03-2005 Removed deactivation calc
/* 04-06-2004 (i) First working compilation
/*
/************************************************************************/


#include "udf.h"

static real dose_0;

DEFINE_ON_DEMAND(dose_setup)
{
  /* if memory for the particle variable titles has not been allocated
     yet, do it now */

   if (NULLP(user_particle_vars))
   {
        Init_User_Particle_Vars();
   }
    /* Set the name and label*/
   strcpy(user_particle_vars[0].name, "absorbed-dose");
   strcpy(user_particle_vars[0].label, "Absorbed Dose");
}
```

```
/* Update the user scalar variables */

DEFINE_DPM_SCALAR_UPDATE(absorbed_dose, cell, thread, initialize, p)
{
  if (initialize)  /* if this is a new particle */
  {
     /* this is the initialization call, set: p->user[0] contains the Dose
        index, initialize to 0. dose_0 contains the dose at the start of a time step*/
          p->user[0] = 0.;
     dose_0      = 0.;  /* be sure to have dose in UDMI[0] in W/cm^2 */
  }
  else
  {
     p->user[0] += P_DT(p) * C_UDMI(cell,thread,0)*1000; // in mJ/cm^2
    /* Add dose in this time step to dose history. */
    /* P_DT(p) is the time of the last timestep in [s]. */
  }
}

/* Set the output formating of the "report-discrete phase-sample" comand */
DEFINE_DPM_OUTPUT(dose_output, header, fp, p, thread, plane)
{
  char name[100];

  fp=fopen("dpm_output.dpm","a");

  if (header)
  {
    if (NNULLP(thread))
      fprintf(fp,"(%s %d)\n",thread->head->dpm_summary.sort_file_name,2);
    else
      fprintf(fp,"(%s %d)\n",plane->sort_file_name,2);
      fprintf(fp,"(%10s %10s %s)\n","time","absorbed-dose","name");
  }
  else
  {
    sprintf(name,"%s:%d",p->injection->name,p->part_id);
    fprintf(fp,"((%15.6g %10.6g) %s)\n", p->state.time, p->user[0], name);
  }
  fclose(fp);
}
```

B.3 Eulerian disinfection model

The Eulerian disinfection model requires the user to define a reaction in Fluent by enabling the species transport model. Two materials, one for dead and one living bacteria, with the properties of water are then generated. Finally a single step reaction is defined with the following stoichiometry: $1Live_{microorg.} \xrightarrow{k} 1Dead_{microorg.}$. The reaction has to be named "inactivation", since the UDF will access a function with this name and calculate the appropriate volumetric reaction rate based on the local UV-fluence (i.e. $k = f(UV_{fluence})$. It is important to have all used material in the proper sequence (1) Life Microorg. (2) Dead Microorg. (3) Water (bulk material).

```
/*************************************************************************/
/*  Author:    Angelo Sozzi  angelo@sozzi.ch
/*  Date:      November 15 2003
/*  Package:   Fluent 6.1.18
/*  Platform:  Windows 2000
/*  Type:      UDF <interpreted> or
/*  Tested on File   "VRtestchannel/Advanced1/channel.cas"
/*
/*  Purpose: This function sets the Reaction rate for the single step
/*   UVU reactions, it takes the value of light from UDM[0]
/*   Note: You need to have initialized UDM[0] in order to use this function.
/*   Note: Be sure to place your initial reaction species on in the first place
/*         on the material list.
/*
/*  Usage:   Compile, and hook the UDF to Vol react rate.
/*   Iterate and look a results in contours
/*
/* Started:   15-11-2003
/*
/* Revisions:
/*
/* 25-11-2004 Updated and working compilation with correct kinetics
/* 17-03-2004 (i) First beta compilation
/*
/*
/*************************************************************************/


#include "udf.h"

DEFINE_VR_RATE(ReactV3_2, c, t, r, mole_weight,species_mf,rate,rr_t)
{
   real mf1 = species_mf[0];     /* species 0 = b (bacteria)              */
   real mw1 = mole_weight[0];
   real c1= C_R(c,t)*mf1/mw1;
   real I  = C_UDMI(c,t,0)*1000; /*Fluence rate in mW/cm^2                */
   real k  = 0.1;                /* k for mJ/cm^2                         */
   if  (!strcmp(r->name, "inactivation"))
   {

     *rate   = I*k*c1;
     *rr_t = *rate;
   }
                                 /* No "return..;" value.                 */
}
```

B.4 Fluent scheme file

To expedite the extraction of data from Fluent, an automated script was written. Fluents scheme language allows all actions performed by mouse or written commands to be scripted. The following scheme file will generate rakes along the center plane of the reactor, extract x,y,z velocity data and write the values into separate files:

```
;; Scheme function to create rakes in L-shape reactor and safe the X,Y,Z velcity and the
;; Velocity Magnitude in the location the Scheme file was read from

;; Creating the Rakes
```

```
(ti-menu-load-string "surface/rake-surface aaRake-z-0.5 0 1.74 0.5 0 -1.74 0.5 100")

(do ((z 1.0 (+ z 1.0))) ((> z 6.0))
  (ti-menu-load-string
  (format #f "surface/rake-surface aaRake-z-0~f 0 1.74 ~4.1f 0 -1.74 ~4.1f 100" z z z))
)

(do ((z 6.9 (+ z 0.1))) ((> z 7.7))
  (ti-menu-load-string
  (format #f "surface/rake-surface aaRake-z-0~3.1f 0 1.74 ~4.1f 0 -1.74 ~4.1f 100" z z z))
)

(do ((z 8.0 (+ z 1.0))) ((> z 9.0))
  (ti-menu-load-string
  (format #f "surface/rake-surface aaRake-z-0~f 0 1.74 ~4.1f 0 -1.74 ~4.1f 100" z z z))
)

(do ((z 10.0 (+ z 5.0))) ((> z 30.0))
  (ti-menu-load-string
  (format #f "surface/rake-surface aaRake-z-~f 0 1.74 ~4.1f 0 -1.74 ~4.1f 100" z z z))
)

;; Saving X-velocity values
(ti-menu-load-string "plot/plot yes Rake-z-0.5-x-velocity.xy no no no x-velocity yes 0 1 0 aarake-z-0.5 ()")

(do ((z 1.0 (+ z 1.0))) ((> z 6.0))
  (ti-menu-load-string
  (format #f "plot/plot yes Rake-z-0~f-x-velocity.xy no no no x-velocity yes 0 1 0 aarake-z-0~f ()" z z))
)

(do ((z 6.9 (+ z 0.1))) ((> z 7.7))
  (ti-menu-load-string
  (format #f "plot/plot yes Rake-z-0~3.1f-x-velocity.xy no no no x-velocity yes 0 1 0 aarake-z-0~3.1f ()" z z))
)

(do ((z 8.0 (+ z 1.0))) ((> z 9.0))
  (ti-menu-load-string
  (format #f "plot/plot yes Rake-z-0~f-x-velocity.xy no no no x-velocity yes 0 1 0 aarake-z-0~f ()" z z))
)

(do ((z 10.0 (+ z 5.0))) ((> z 30.0))
  (ti-menu-load-string
  (format #f "plot/plot yes Rake-z-~f-x-velocity.xy no no no x-velocity yes 0 1 0 aarake-z-~f ()" z z))
)

;; Saving Y-Velocity values
(ti-menu-load-string "plot/plot yes Rake-z-0.5-y-velocity.xy no no no y-velocity yes 0 1 0 aarake-z-0.5 ()")

(do ((z 1.0 (+ z 1.0))) ((> z 6.0))
  (ti-menu-load-string
  (format #f "plot/plot yes Rake-z-0~f-y-velocity.xy no no no y-velocity yes 0 1 0 aarake-z-0~f ()" z z))
)

(do ((z 6.9 (+ z 0.1))) ((> z 7.7))
  (ti-menu-load-string
  (format #f "plot/plot yes Rake-z-0~3.1f-y-velocity.xy no no no y-velocity yes 0 1 0 aarake-z-0~3.1f ()" z z))
)

(do ((z 8.0 (+ z 1.0))) ((> z 9.0))
  (ti-menu-load-string
  (format #f "plot/plot yes Rake-z-0~f-y-velocity.xy no no no y-velocity yes 0 1 0 aarake-z-0~f ()" z z))
)

(do ((z 10.0 (+ z 5.0))) ((> z 30.0))
  (ti-menu-load-string
  (format #f "plot/plot yes Rake-z-~f-y-velocity.xy no no no y-velocity yes 0 1 0 aarake-z-~f ()" z z))
)
```

```
;; Saving Z-Velocity values
(ti-menu-load-string "plot/plot yes Rake-z-0.5-z-velocity.xy no no no z-velocity yes 0 1 0 aarake-z-0.5 ()")

(do ((z 1.0 (+ z 1.0))) ((> z 6.0))
  (ti-menu-load-string
  (format #f "plot/plot yes Rake-z-0~f-z-velocity.xy no no no z-velocity yes 0 1 0 aarake-z-0~f ()" z z))
)

(do ((z 6.9 (+ z 0.1))) ((> z 7.7))
  (ti-menu-load-string
  (format #f "plot/plot yes Rake-z-0~3.1f-z-velocity.xy no no no z-velocity yes 0 1 0 aarake-z-0~3.1f ()" z z))
)

(do ((z 8.0 (+ z 1.0))) ((> z 9.0))
  (ti-menu-load-string
  (format #f "plot/plot yes Rake-z-0~f-z-velocity.xy no no no z-velocity yes 0 1 0 aarake-z-0~f ()" z z))
)

(do ((z 10.0 (+ z 5.0))) ((> z 30.0))
  (ti-menu-load-string
  (format #f "plot/plot yes Rake-z-~f-z-velocity.xy no no no z-velocity yes 0 1 0 aarake-z-~f ()" z z))
)

;; Saving Velocity-Magnitude values
(ti-menu-load-string "plot/plot yes Rake-z-0.5-velocity-magnitude.xy no no no velocity-magnitude yes 0 1 0 aarake-z-0.5 ()")

(do ((z 1.0 (+ z 1.0))) ((> z 6.0))
  (ti-menu-load-string
  (format #f "plot/plot yes Rake-z-0~f-velocity-magnitude.xy no no no velocity-magnitude yes 0 1 0 aarake-z-0~f ()" z z))
)

(do ((z 6.9 (+ z 0.1))) ((> z 7.7))
  (ti-menu-load-string
  (format #f "plot/plot yes Rake-z-0~3.1f-velocity-magnitude.xy no no no velocity-magnitude yes 0 1 0 aarake-z-0~3.1f ()" z z))
)

(do ((z 8.0 (+ z 1.0))) ((> z 9.0))
  (ti-menu-load-string
  (format #f "plot/plot yes Rake-z-0~f-velocity-magnitude.xy no no no velocity-magnitude yes 0 1 0 aarake-z-0~f ()" z z))
)

(do ((z 10.0 (+ z 5.0))) ((> z 30.0))
  (ti-menu-load-string
  (format #f "plot/plot yes Rake-z-~f-velocity-magnitude.xy no no no velocity-magnitude yes 0 1 0 aarake-z-~f ()" z z))
)
```

B.5 Excel velocity data import macro

In order to import the files written by the Fluent scheme file, an excel macro was created. When pointed to the folder containing the scheme exported data, it will import the velocity data. Only the z-velocity import is shown, other data can be imported by changing the filename in the program. Two additional macros are used to properly align the data and to prune the multiple x axis values.

```
Sub import_z()
'
' import_z Macro
```

```
' Macro recorded 8/3/2004 by Angelo
'
' Keyboard Shortcut: Ctrl+Shift+E
' Make sure you are in the sheet you want to imort the data into before starting!
    Dim i, Max As Integer
    Dim name, pfad
    Dim colOffset, rowOffset
    colOffset = 2       ' Nr of Columns to offset the import from
    rowOffset = 3       ' Nr of Rows to offsett the import from
    Max = 23             ' The maximum number of files to read in (don't try more than you have

    For i = 1 To Max
    name = Worksheets("filename").Cells(i, 1).Value    ' This is where the filenumbering is stored (rake z-position)
    '-z-velocity
    '-y-velocity
    '-x-velocity
    '-velocity-magnitude
    pfad = "TEXT;C:\extract\Rake-z-" + name + "-z-velocity.xy" ' The path where the files are situated
    With ActiveSheet.QueryTables.Add(Connection:=pfad, Destination:=ActiveSheet.Cells(1 + rowOffset, i * 2 - 1 + colOffset))
        .name = "Rake-z-0" + LTrim(Str$(i)) + "-x-velocity.xy"
        .FieldNames = True
        .RowNumbers = False
        .FillAdjacentFormulas = False
        .PreserveFormatting = True
        .RefreshOnFileOpen = False
        .RefreshStyle = xlInsertDeleteCells
        .SavePassword = False
        .SaveData = True
        .AdjustColumnWidth = True
        .RefreshPeriod = 0
        .TextFilePromptOnRefresh = False
        .TextFilePlatform = 437
        .TextFileStartRow = 5
        .TextFileParseType = xlDelimited
        .TextFileTextQualifier = xlTextQualifierDoubleQuote
        .TextFileConsecutiveDelimiter = False
        .TextFileTabDelimiter = True
        .TextFileSemicolonDelimiter = False
        .TextFileCommaDelimiter = False
        .TextFileSpaceDelimiter = False
        .TextFileColumnDataTypes = Array(1)
        .TextFileTrailingMinusNumbers = True
        .Refresh BackgroundQuery:=False
    End With
    Next i
End Sub

--------------------------------------------------------------------------------
Sub cut_paste()
'
' cut_paste Macro
' Macro recorded 8/3/2004 by Angelo
' This Macro makes sure that the missing points from the y-rakes in the reactor are lined up properly
' It compares the x values of the first row (full 100 points) to the x values of the later rows and if it finds
' a mismatch it cuts the cells from those two rows and shifts them down to the point where the x values match up again
'
Dim j, i, first_row, second_row As Integer
Dim x1, x2, row_test, xfix, lastusedRow, lastusedColumn, ExcelLastCell
Dim colOffset, rowOffset
    colOffset = 2       ' Nr of Columns to offset the import from
    rowOffset = 3       ' Nr of Rows to offsett the import from
ExcelLastCell = ActiveSheet.Cells.SpecialCells(xlLastCell)
'lastusedColumn = ActiveSheet.Cells(rowOffset + 1, 150).End(xlLeft).Column 'Find the last used cell in the row
lastusedColumn = ActiveSheet.UsedRange.Columns.Count  ' Only works for sheets with no other data but Hey it works
    For j = colOffset + 1 To lastusedColumn / 2 ' loop through columns with data
        row_test = 0
        xfix = -1000000
        lastusedRow = ActiveSheet.Cells(150, j).End(xlUp).Row   'Find the last used cell in the row
```

```
        If ActiveSheet.Cells(lastusedRow, j).Value = ")" Then
            ActiveSheet.Cells(lastusedRow, j).ClearContents
            lastusedRow = lastusedRow - 1
        End If

        For i = rowOffset + 1 To lastusedRow
            x1 = ActiveSheet.Cells(i, colOffset + 1) 'Cells(Rows,Columns) = Range(Ai)
            If ActiveSheet.Cells(i, 1 + 2 * j).Value <> ")" Then x2 = ActiveSheet.Cells(i, 1 + 2 * j).Value
            ' If x2 = Empty Then Stop
            If Abs(x1 - x2) / Abs(x1) > 0.1 And row_test = 0 Then
                first_row = i
                row_test = 1
                xfix = x2
            End If
            If Abs(xfix - x1) / Abs(x1) < 0.0001 Then
                second_row = i
                ' Stop
            End If
        Next i
        'Stop
        If row_test <> 0 Then
            ActiveSheet.Range(Cells(first_row, 1 + 2 * j), Cells(100, 2 + 2 * j)).Select
            Selection.Cut
            ActiveSheet.Cells(second_row, 1 + 2 * j).Select
            ActiveSheet.Paste
        End If
       ' Stop
    Next j

-------------------------------------------------------------------------------------

End Sub
Sub Delete_Every_Other_Column()
Dim y, i, xRng, xCounter, offset
   ' Dimension variables.
   y = True             ' Change this to True if you want to delete rows 1, 3, 5, and so on.
   i = 1
   Set xRng = Selection
   ' Loop once for every row in the selection.
   For xCounter = 1 To xRng.Columns.Count

       ' If Y is True, then...
       If y = True Then

           ' ...delete an entire row of cells.
           xRng.Cells(i).EntireColumn.Delete

       ' Otherwise...
       Else

           ' ...increment I by one so we can cycle through range.
           i = i + 1

       End If

       ' If Y is True, make it False; if Y is False, make it True.
       y = Not y

   Next xCounter
End Sub
```